

PULSED EDDY CURRENT INSPECTION OF
SECOND LAYER WING STRUCTURE

UTILISATION DES COURANTS DE FOUCAULT PULSÉS POUR
L'INSPECTION DE LA DEUXIÈME COUCHE STRUCTURALE
D'UNE AILE D'AVION

A Thesis Submitted

To the Division of Graduate Studies of the Royal Military College of Canada

by

Colette Amelia Stott

Captain

In Partial Fulfillment of the Requirements for the Degree of
Masters of Applied Science in Chemical and Materials Engineering

9 June 2014

©This thesis may be used within the Department of National Defence
but copyright for open publication remains the property of the author.

ROYAL MILITARY COLLEGE OF CANADA
 COLLÈGE MILITAIRE ROYAL DU CANADA

DIVISION OF GRADUATE STUDIES AND RESEARCH
 DIVISION DES ÉTUDES SUPÉRIEURES ET DE LA RECHERCHE

This is to certify that the thesis prepared by / Ceci certifie que la thèse rédigée par

Colette Amelia Stott

entitled / intitulée

Pulsed Eddy Current Inspection of Second Layer Wing Structure /
 Utilisation des courants de Foucault pulsés pour l'inspection de la deuxième couche structurale d'une aile
 d'avion

complies with the Royal Military College of Canada regulations and that it meets the accepted standards of the
 Graduate School with respect to quality, and, in the case of a doctoral thesis, originality, / satisfait aux
 règlements du Collège militaire royal du Canada et qu'elle respecte les normes acceptées par la Faculté des
 études supérieures quant à la qualité et, dans le cas d'une thèse de doctorat, l'originalité,

for the degree of / pour le diplôme de

Master of Applied Science / Maîtrise en Science Appliquée

Signed by the final examining committee: /
 Signé par les membres du comité examinateur de la soutenance de thèse

_____, Chair / Président

_____, External Examiner / Examineur externe

_____, Main Supervisor / Directeur de thèse principal

Approved by the Head of Department: /
 Approuvé par le Directeur du Département: _____ Date: _____

To the Librarian: This thesis is not to be regarded as classified. /
 Au Bibliothécaire: Cette thèse n'est pas considérée comme à publication restreinte.

 Main Supervisor / Directeur de thèse principal

Acknowledgements

I would like to thank Dr. Krause, my thesis supervisor, for his guidance and patience throughout the last two years. Your dedication to the Non-Destructive Testing field, as well as encouragement and constructive feedback has greatly contributed to the success of this thesis.

I would also like to thank Dr. Underhill (Royal Military College of Canada Mechanical Engineering Department) for his unwavering support, assistance in building probes, Labview programs and whatever else I asked of him. Additionally I would like to thank Dr. Babbar (RMCC Physics Department) for his research, COMSOL modelling and assistance in understanding electromagnetic theories.

Additionally, I would like to thank Captain Alayne Edwards, Captain Ashley Oliver and Sgt James Scalf from the Aerospace Technical Engineering Support Squadron (ATESS) for their help in ordering parts for test pieces, and providing NDT expertise. Also, a special thank you is extended to Dr. Sangalli (RMCC Physics Department) for the French translation of the title and abstract.

Finally, I would like to thank Chris for his patience and understanding throughout the last two years. Your support has helped guide me through a great challenge and I could not have done it without you.

Abstract

A thesis completed by Stott, Colette Amelia, in partial fulfilment of the requirements for a MASc in Chemistry and Materials Engineering from the Royal Military College of Canada on this 9th June, 2014 on *Pulsed Eddy Current Inspection of Second Layer Wing Structure*, under the direction of Dr. Thomas Krause.

Non-destructive testing has become a valuable inspection tool for the aerospace industry. In particular, eddy current testing is used extensively to detect surface and near surface defects in aluminum aircraft component structures. However, there exists a requirement to inspect for the presence of cyclic fatigue cracks around ferrous fasteners in the second layer of double layer structures, such as the lap-joint of the CP-140 Aurora, and CC-130 Hercules. These defects are not easily detectable by conventional eddy current techniques, unless the fasteners are removed. A capability to inspect through the top layer would avoid fastener removal, in turn reducing down time and risk of collateral damage to the structure. Pulsed eddy current (PEC) is an emerging technique with the potential to detect cyclic fatigue cracking in the second layer of aluminum wing structures. PEC offers potential advantages over conventional eddy current in that the inspection occurs from the top layer, does not require fastener removal and the diffused magnetic field can be sensed at greater depths within the material. However, the time-domain PEC signals show only subtle differences between the presence or absence of cracks. Principal components analysis (PCA) is a statistical tool that can be used to reduce the time domain signal to a small number of scores, which enhance the distinction between PEC signals. These scores are clustered depending on whether a crack is present. The relative distance (Mahalanobis Distance), between the scores for a crack and the centroid of the scores for fasteners with no crack can be used to distinguish between cracks and non-cracks.

A PEC coil-based probe was tested on three lap-joint samples containing ferrous fasteners, two of which were actual CP-140 Aurora airframes, and one that was fabricated in the lab. Simulated flaws, ranging in size from 0.8 - 5.5 mm, were present in both the top and bottom aluminum layers. One hundred percent of the simulated flaws were detected in two of the samples with top sheet thickness of 2 mm, and 82% in a thicker (2.6 mm thick first layer) airframe section with a different fastener type, all at 5% false call rate. An observed correlation between Mahalanobis Distance and crack size also suggested that sizing of second layer cracks is possible.

Résumé

Thèse complétée par Stott, Colette Amelia, pour l'obtention d'une MASC en Chimie et Génie des Matériaux du Collège militaire royal du Canada ce 9 juin 2014 sur *utilisation des courants de Foucault pulsés pour l'inspection de la deuxième couche structurale d'une aile d'avion*, sous la supervision directe de Dr Thomas Krause.

Le contrôle non destructif est une technique de grande valeur pour l'industrie aérospatiale. En particulier, les courants de Foucault sont largement utilisés pour détecter les défauts de surface ou proche de la surface des composantes en aluminium dans les avions. Des critères d'inspection existent pour estimer la présence de fissures dues à la fatigue cyclique autour des attaches en fer au niveau de la deuxième couche d'une structure à deux couches, comme les joints de recouvrement des ailes des avions Aurora CP-140 et Hercules CC-130. Ces défauts ne sont pas détectables facilement avec les méthodes de courants de Foucault conventionnelles, à moins que les attaches en fer soient retirées. La capacité d'accomplir l'inspection à travers la couche supérieure des ailes permettrait d'éviter le retrait des attaches et donc de réduire la durée d'inspection et les risques collatéraux d'endommagement de la structure. L'usage des courants de Foucault pulsés (CFP) est une méthode relativement récente qui pourrait détecter les fissures dues à la fatigue cyclique dans la deuxième couche structurale des ailes d'avions en aluminium. L'avantage des CFP par rapport aux méthodes conventionnelles est que l'inspection est effectuée sans le retrait des attaches directement à travers la couche externe de l'aile et le champ magnétique diffusé peut être détecté plus profondément dans le matériau. Cependant, le signal des CFP dans le domaine temporel ne manifeste que de petites différences en présence de fissure par rapport à celui mesuré quand aucune fissure n'est présente. L'analyse en composantes principales (ACP) est un outil statistique qui peut être utilisé pour réduire le signal temporel en un petit nombre de poids ce qui permet d'augmenter les différences entre les signaux des CFP. Ces poids sont groupés en fonction de la présence de fissure. La distance relative (distance de Mahalanobis) entre les poids en présence de fissures et le centroïde des poids quand il n'y a pas de fissures, peut être utilisés pour distinguer les signaux dus sans fissures et avec fissures.

Une sonde CFP à base de bobines fut testée sur trois joints de recouvrement comprenant des attaches ferreuses, deux joints proviennent d'avions Aurora CP-140 et le troisième fut fabriqué au laboratoire. Des défauts allant de 0.8 à 5.5 mm furent créés à la fois dans première et la deuxième couche d'aluminium. Cent pourcent des défauts furent détectés dans les deux échantillons possédant une couche supérieure de 2 mm d'épaisseur et 82% des défauts furent détecté dans l'échantillon dont

la couche supérieure mesure 2.6 mm d'épaisseur et avec différents types d'attaches, dans tous les cas le taux de fausse détection est de 5%. La corrélation observée entre la distance de Mahalanobis et la taille des fissures suggère qu'il est possible d'estimer la taille des défauts de la seconde couche.

Table of Contents

Acknowledgements.....	iii
Abstract	iv
Résumé	v
List of Tables	xii
List of Figures.....	xiii
List of Abbreviations.....	xvi
1. Introduction	1
1.1 General.....	1
1.2 Eddy Current Testing	3
1.3 Research Survey.....	5
1.3.1 Analytical Work.....	5
1.3.2 Crack Detection in the Presence of Fasteners.....	6
1.3.3 PEC Signal Analysis.....	8
1.3.4 PEC signals and Principal Components Analysis	11
1.3.5 PCA and Mahalanobis Distance	13
1.4 Objective	14
1.5 Thesis Scope and Methodology	14
2 Theory	16
2.1 General.....	16
2.2 Maxwell's Equations	16
2.3 Electromagnetic Waves in Conductors.....	17
2.4 Diffusion Equations	18
2.5 Charge dissipation in a conductor	20
2.6 Skin Depth Theory.....	20

2.7	Eddy Current Generation	21
2.8	Equivalent Circuit Diagram	22
2.9	Principal Components Analysis (PCA)	26
2.9.1	General	26
2.9.2	PCA Method	26
2.9.3	PCA Scores	29
2.10	Cluster Analysis Method	30
2.10.1	Mahalanobis Distance Definition	30
2.10.2	Decision Threshold	31
2.11	Probability of False Positive (False Calls)	31
3	Experimental Technique	33
3.1	General	33
3.2	Coil Probe Design	33
3.3	Sensing Equipment	34
3.4	Single Fastener Test Piece	35
3.5	Multiple Fastener Test Pieces	36
3.5.1	NAVAIR Sample Description	36
3.5.2	Test Piece #1 Description	38
3.5.3	Test Piece #2 Description	40
3.5.4	CP-140-TT-1B Test Piece	40
3.6	Experimental Procedure	42
3.6.1	Probe Alignment	42
3.6.2	Single Fastener Experimental Procedure	44
3.6.3	Multiple Fastener Test Piece Experimental Procedure	45
3.7	Summary of Experiments	45
3.8	Signal Processing	46

3.8.1	Signal Gating.....	46
3.8.2	Signal Analysis	47
4	Results and Analysis of Single Fastener Case.....	49
4.1	General.....	49
4.2	Off-Centering Effects.....	49
4.3	Notch Effects	51
5	Results and Analysis of Multiple Fastener Case.....	54
5.1	General.....	54
5.2	Off-Centering Effects.....	54
5.3	Notch Effects	57
5.4	Effect Due to Height of Fastener Head and Lift-Off.....	57
5.4.1	Fastener Head Height Effects.....	58
5.4.2	Lift-off Effects	61
5.5	Effect Due to Edge.....	62
5.6	Effect Due to Fastener Distance from Edge.....	63
5.7	Effect of Temperature on Probe Performance	65
5.8	Results on NAVAIR Sample.....	65
5.8.1	Test Piece Summary	65
5.8.2	Eigenvector Selection.....	65
5.8.3	Absolute Mode Crack Detection Test Results	67
5.8.4	Differential Mode Crack Detection Test Results.....	69
5.8.5	Mahalanobis Distance versus Crack Size	71
5.9	Results on Test Piece #1.....	72
5.9.1	Test Piece Summary	72
5.9.2	Eigenvector Selection.....	72
5.9.3	Absolute Mode Crack Detection Results	73

5.9.4	Differential Mode Crack Detection Results.....	75
5.9.5	Mahalanobis Distance versus Crack Size	76
5.10	Results on Test Piece CP-140-TT-1B	77
5.10.1	Test Piece Summary	77
5.10.2	Differential Mode Crack Detection Results.....	77
5.10.3	Mahalanobis Distance versus Crack Size Results.....	79
5.11	Comparison of Test Piece Results (Differential Analysis)	80
6	Discussion.....	82
6.1	PCA and Crack Orientation	82
6.2	Absolute versus Differential Analysis	83
6.3	Comparison to FEM.....	84
6.4	PCA Score Correlations with Variables	84
6.5	Minimum Detectable Flaw Size	85
6.5.1	General	85
6.5.2	First Layer Notches	86
6.5.3	Second Layer Notch Detection	86
6.6	False Call Rates.....	87
6.7	Sources of Uncertainty	87
6.7.1	Coil Balancing.....	87
7	Conclusions and Recommendations.....	88
7.1	Conclusions.....	88
7.2	Recommendations.....	89
	References.....	92
	Annex A	97
	Annex B.....	98
	Annex C.....	99

Curriculum Vitae.....102

List of Tables

Table 1: Description of parameters for Figure 11.	23
Table 2: Driving coil and pick-up coil parameters.	34
Table 3: Single fastener case experimental parameters.	36
Table 4: NAVAIR sample notch locations and lengths.	38
Table 5: Test piece #1 notch parameters.	40
Table 6: CP-140-TT-1B notch parameters.	42
Table 7: Shimming experimental parameters.	44
Table 8: Number of measurements taken per test piece.	45
Table 9: Summary table of experiments conducted on each test piece, in sequence.	45
Table 10: NAVAIR sample experimental cases for off-centering and notch effects on PCA scores.	54
Table 11: Test Piece #2 HL-19-5-5 fastener head height relative to aluminum surface, for no notch sites.	58
Table 12: Distance from edge of fastener to edge of aluminum.	63
Table 13: NAVAIR Sample crack detection results in absolute mode.	69
Table 14: NAVAIR Sample crack detection results in differential mode.	70
Table 15: Test piece #1 crack detection results in absolute mode.	74
Table 16: Test Piece #1 crack detection results in differential mode.	75
Table 17: Test piece CP-140-TT-1B crack detection results in differential mode.	77
Table 18: Crack detection results for no false calls, 5% and 10% false call rate.	81
Table 19: Summary of PCA correlations with different variables.	85

List of Figures

Figure 1: Cross-section of lap joint (a), where the two sections are attached using a row of fasteners, and (b) close up of crack location showing aspect ratio of 1:1.	2
Figure 2: Typical damage that can occur to wing skin during fastener removal.	3
Figure 3: Front view of a solved 3D finite element half-model showing flux penetration through the ferrous fastener (CDDP Probe design) [25].	8
Figure 4: Typical PEC signal with common signal response analysis.	9
Figure 5: Time domain response from four fasteners, with and without notches.	10
Figure 6: Zoomed view of peaks from Figure 5.	10
Figure 7: Zoomed view of zero-crossing from Figure 5.	11
Figure 8: Sample and probe geometry used in FE models [32].	13
Figure 9: RL circuit representing excitation coil.	22
Figure 10: Current in driving coil representing equation 2.33.	23
Figure 11: Equivalent circuit diagram for driving coil and pick-up coil.	24
Figure 12: Current response in pick-up coil representing equation 2.36 (i_2).	25
Figure 13: Three-way mutual inductance relationships between driving coil, pick-up coil and sample.	26
Figure 14: PEC original signal with first eigenvector reproduction, and eigenvectors 1-4 reproduction. The insert shows the four eigenvectors for each coil of the pair, used for the reproduction.	29
Figure 15: PCA scores viewed in 3D, in the (a) un-rotated view and (b) rotated view for fasteners with (●) and without (○) notches at their bore.	30
Figure 16: Probe face with central driving coil, ferrite core and eight pick-up coils.	33
Figure 17: Flow chart depiction of sensing equipment operation cycle.	35
Figure 18: Side view of Single Fastener Test Piece with three plates and centrally located ferrous fastener.	35
Figure 19: NAVAIR sample with notches, view from top.	37
Figure 20: NAVAIR sample with view of fastener.	37
Figure 21: View from top. Notch orientation diagram.	37
Figure 22: Microscopic photo of notch cut into fastener hole (11x magnification).	39
Figure 23: Picture of test piece #1.	39
Figure 24: Picture of section of CP-140-TT-1B test piece.	41

Figure 25: Schematics of notches located at fasteners 9 and 19 of CP-140-TT-1B Aurora Sample...	41
Figure 26: Alignment tool, showing the direction of shimming (0° and 90°).	43
Figure 27: Probe with alignment guide and sample.....	44
Figure 28: Raw PEC data signal from a fastener without a notch, indicating the gate.	46
Figure 29: Eddy current density curve from finite element modeling.....	47
Figure 30: Data processing sequence for PEC signals.	48
Figure 31: Plot of PCA scores S2 versus S1 for single fastener with no notch, showing off-centered results.	49
Figure 32: Plot of PCA scores S3 versus S1 for single fastener with no notch, showing off-centered results.	50
Figure 33: Plot of PCA scores S5 versus S4 for single fastener with no notch, showing off-centered results.	51
Figure 34: Plot of PCA scores S2 versus S1 for single fastener case of no notch (\diamond), 2 mm (\square) and 8 mm (Δ) notch. Arrows indicate direction of increasing notch length.....	52
Figure 35: Plot of PCA scores S3 versus S2 for single fastener case of no notch (\diamond), 2 mm (\square) and 8 mm (Δ) notch. Arrows indicate direction of increasing notch length.....	52
Figure 36: Plot of PCA scores S5 versus S4 for single fastener case of no notch (\diamond), 2 mm (\square) and 8 mm (Δ) notch. Arrows indicate direction of increasing notch length.....	53
Figure 37: Plot of S2 versus S1. Numbers correspond to Table 10 cases. For probe displacement (disp), arrows indicate direction of increasing displacement.	55
Figure 38: Plot of S3 versus S1. Numbers correspond to Table 10 cases. For probe displacement (disp), arrows indicate direction of increasing displacement.	56
Figure 39: Plot of S4 versus S1. Numbers correspond to Table 10 cases. For probe displacement (disp), arrows indicate direction of increasing displacement.	56
Figure 40: Plot of S5 versus S1. Numbers correspond to Table 10 cases. For probe displacement (disp), arrows indicate direction of increasing displacement.	57
Figure 41: Effect of fastener head height distance and lift-off distance on first PCA score (S1).....	59
Figure 42: Effect of fastener head height distance and lift-off distance on second PCA score (S2). .	59
Figure 43: Effect of fastener head height distance and lift-off distance on the third PCA score (S3).	60
Figure 44: Effect of fastener head height distance and lift-off distance on the fourth PCA score (S4).	60

Figure 45: Effect of fastener head height distance and lift-off distance on the fifth PCA score (S5).	61
Figure 46: Experimental no-crack differential signals from all four coil pairs.....	63
Figure 47: PCA score S4 plotted with fastener distance to edge in millimeters.	64
Figure 48: PCA score S5 plotted with fastener distance to edge in millimeters.	64
Figure 49: First five eigenvectors of PCA on data from NAVAIR third coil pair (differential mode).	66
Figure 50: Results from logistic regression performed on hit miss data from NAVAIR sample using 1-3, 1-4 and 1-5 eigenvectors. Horizontal axis is on a log scale.....	67
Figure 51: 3-D view of NAVAIR data PCA scores S2, 3 & 4.	68
Figure 52: NAVAIR Sample Mahalanobis Distance versus fastener # in absolute mode.	69
Figure 53: NAVAIR Sample Mahalanobis Distance versus fastener # in differential mode.	70
Figure 54: Mahalanobis Distance versus crack size for NAVAIR Sample second layer cracks in differential mode.	71
Figure 55: First five eigenvectors of PCA on data from Test Piece #1 third coil pair (concatenated signals) in absolute mode.	72
Figure 56: Results from logistic regression performed on hit miss data from Test Piece #1 using eigenvectors 3-5 and 1-5. Horizontal axis is on a log scale.....	73
Figure 57: Test Piece#1 Mahalanobis Distance versus fastener # in absolute mode.	74
Figure 58: Test Piece#1 Mahalanobis Distance versus fastener # in differential mode.....	75
Figure 59: Mahalanobis Distance versus crack size for Test Piece #1 in differential mode.	76
Figure 60: CP-140-TT-1B Mahalanobis Distance versus fastener # in differential mode.	78
Figure 61: Mahalanobis Distance versus crack size for test piece CP-140-TT-1B in differential mode.	80
Figure 62: Three dimensional depiction of PCA scores S2, S3 and S4 from NAVAIR differential data. Labels refer to notch orientation as defined in the inserted figure.	83

List of Abbreviations

AC	Alternating Current
ATESS	Aerospace and Telecommunications Engineering Support Squadron
AWG	American Wire Gauge
BHEC	Bolt Hole Eddy Current
CDDP	Central Driver Differential Pickup
CFRP	Carbon Fiber Reinforced Polymer
CGSB	Canadian General Standards Board
EDM	Electrically Discharge Machining
EMF	Electromotive Force
ET	Eddy-Current Testing
FEM	Finite Element Modelling
GMR	Giant Magneto-resistive
IACS	International Annealed Copper Standard
LPI	Liquid Penetrant Inspection
MD	Mahalanobis Distance
MPI	Magnetic Particle Inspection
NDE	Non-destructive Evaluation
NDT	Non-destructive Testing
NI	National Instruments
NN	No Notch
PCA	Principal Components Analysis
PEC	Pulsed Eddy Current
POD	Probability of Detection
SCC	Stress Corrosion Cracking
UT	Ultrasonic Testing

1. Introduction

1.1 General

The probability of failure of aircraft components in flight has been reduced by the implementation of inspection programs. The application of non-destructive evaluation techniques (NDE) provides a means of inspecting aircraft and their components for flaws or damage without ideally compromising the component's future use. The aerospace industry has introduced the application of NDE techniques into inspection schedules with increasing age of military and civilian aircraft. Additionally, scheduled maintenance periods may be lengthened with proper use of these techniques in the maintenance cycle [1]. Non-destructive testing (NDT) techniques are similar to those of NDE. However, NDE incorporates additional analysis of measurements that are more quantitative in nature [2].

There are many different types of NDE methods but the only five certified NDT techniques of the Canadian General Standards Board (CGSB) are: ultrasonic testing (UT), radiography, liquid penetrant inspection (LPI), magnetic particle inspection (MPI) and eddy current [3]. Understanding the physical basis of these techniques, along with their respective strengths and limitations, helps determine reliable inspection criteria for the aerospace industry. Despite advances in technology, there are still many inspection requirements that are beyond the capability of the five techniques mentioned above, which drives research in the field of NDE.

The CP-140 Aurora and CC-130 Hercules aircraft most often employ the eddy current NDT method because their aircraft structures are mainly composed of highly conducting aluminum (30.0% - 31.4% International Annealed Copper Standard (IACS)). However, in some cases, there are requirements to inspect second layer aluminum structure, such as at a lap joint, where two plate sections are attached with a row of fasteners [4]. A schematic of a lap joint is shown in Figure 1.

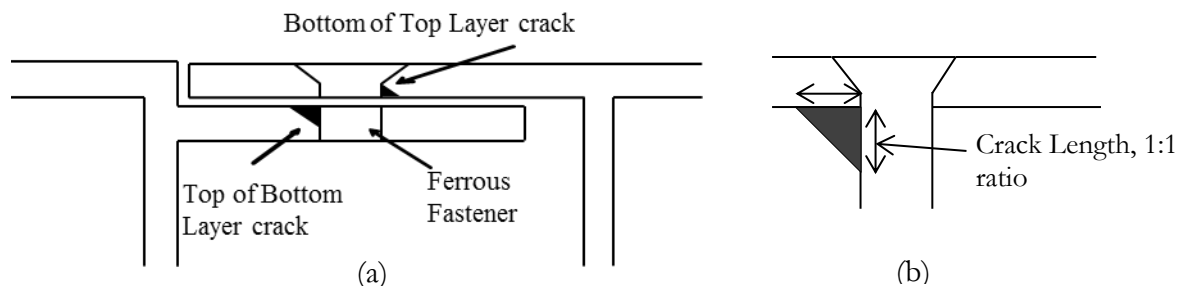


Figure 1: Cross-section of lap joint (a), where the two sections are attached using a row of fasteners, and (b) close up of crack location showing aspect ratio of 1:1.

Fatigue cracks are one type of in-service damage to which an aircraft riveted component is susceptible. Small flaws may be initiators for cracks, which have the potential to grow to critical crack length by cyclic loading of a component in tension and compression, eventually leading to fracture of the component [5]. The lap joint is of particular concern because fatigue cracks may originate around the ferrous fasteners in the bottom of the top layer and/or top of the bottom layer, as shown in Figure 1 (a). In addition, crack size refers to the length along the surface of aluminum. In this thesis, the terms crack, notch and defect are used interchangeably, with the understanding that some differences in eddy current response may be present.

There are two current methods for inspecting for cyclic fatigue. The first method utilizes conventional eddy current [6], with fasteners retained. The NDT system is capable of reliably detecting 2.54 mm cracks (see Figure 1 (b), aspect ratio length-to-depth is 1:1), but the probe requires rotation to detect cracks in multiple directions, and the system presently has limitations in four directions (0° , 90° , 180° and 270° , see Figure 21). The second method of inspecting for cyclic fatigue is bolt-hole eddy current (BHEC) [7], which requires fastener removal. This is a time consuming process, involving the removal of fasteners and their replacement resulting in extended down time of the aircraft and potentially causing further damage to the aircraft, as shown in Figure 2.



Figure 2: Typical damage that can occur to wing skin during fastener removal.

The minimum detectable flaw size, or $a_{90/95}$ (the crack size that an NDT technique is able to detect 90% of the discontinuities of that size, 95% of the time [8]), for second layer notches is not yet defined using PEC technique. However, the current BHEC technique used on the CP-140 Aurora fleet has an $a_{90/95}$ of 0.76 mm (0.030 inch) flaw [9]. In addition, the eddy current inspection of CP-140 Aurora wing lap joint fastener holes (technique # 140-306-E) has a minimum detectable flaw size of 2.54 mm, (0.100 inch) for flaws in the first and second layer, with fasteners retained [9]. In order to be a competitive technique with BHEC, the goal of this work is to demonstrate the potential to detect flaw size of 0.8 mm in the second layer, using PEC, which does not require removal of fasteners. This size of crack needs to be reliably detected given known crack growth rates and critical crack size, in conjunction with the given inspection interval.

1.2 Eddy Current Testing

The NDT method eddy current testing (ET), utilizes the induction of currents, referred to as eddy currents, in electrically conductive materials [1]. In conventional eddy current methods, a sinusoidal excitation generates a changing magnetic field close to the part being inspected. The eddy currents are formed in response to the changing electromagnetic field according to Faraday's Law [10]. When a defect is present, pick-up coils sense the changing field, and results are displayed on an impedance plane display [11].

Eddy current techniques are limited by depth of penetration of the induced field and the consequent induced response in a sensor for the particular material being inspected. Second layer cracks in aluminum structures pose a challenge for the depth at which cracks may be detected. This limitation of depth-of-penetration may be partially overcome by the application of pulsed (transient) eddy current (PEC). The PEC method is an emerging technique that has been investigated for the

detection of surface and subsurface defects in multilayered structures [4] [12]. Instead of the sinusoidal excitation applied in conventional techniques, PEC uses a square pulse excitation, which may be viewed as being comprised of a spectrum of discrete frequencies [13]. It is the lower frequency components of the transient pulse that have been shown to travel deeper into the conductive material than conventional techniques [14], making PEC a viable technique for crack detection at greater depths.

Cadeau [15] examined different coil configurations to determine an optimal probe to detect cracks at increased depths, without fasteners present. He observed improved depth of penetration when the driving coil was relatively large in length and diameter and wound with an American wire gauge standard (AWG) of 34, thereby increasing the relaxation time of the probe. In addition, increasing the voltage applied to the coil improves the depth to which one can identify discontinuities in a material [15]. It has been suggested, based on simple skin depth arguments, that the PEC technique should be able to penetrate 1.8 times deeper than that of conventional eddy current [13]. This means that since the magnetic fields penetrate further into the material, defects should be detectable at greater depths using PEC than for conventional techniques.

The presence of a ferrous fastener near the area to be inspected also introduces further limitations for conventional ET due to the strong magnetic response the fastener induces, overwhelming coil response and thereby, hampering defect detection. It is for these reasons that a viable solution must be sought to overcome depth of penetration restrictions, and signal variations due to the presence of ferrous fasteners.

This thesis utilizes the probe design tested by Whalen [2], for PEC inspection in the presence of ferrous fasteners. Furthermore, recent work conducted by Horan *et al.* [16] has shown PEC as a viable option for crack detection in inner wing spars at large lift-offs, defined as probe-to-specimen spacing [11], (up to 20 mm). Horan *et al.*'s technique employed the statistical analysis of principal components, which reduces PEC signals to a series of scores and eigenvectors that express as much of the variation in the data as possible [17]. The work presented here combines the probe design of Whalen and Horan *et al.*; however, it utilizes a multi-coil design that has been optimized for cyclic fatigue crack detection in second layer aluminum structures. In addition, the application of principal components analysis (PCA) on PEC signals and an additional cluster analysis method, termed

Mahalanobis Distance analysis [17], are used to further distinguish between signals obtained in the presence of cracks from those where cracks are not present.

1.3 Research Survey

A literature review of the field of eddy current testing, specifically for aircraft structures was performed. Extensive research has been conducted for the application of conventional eddy current testing for detecting flaws in aircraft structures. In the area of PEC, recent research [4] [12] [13] [14] [18] is becoming available and this material will be considered in light of the objective of this thesis. Crack detection in the presence of ferrous fasteners is explored, along with PEC signal analysis using statistical techniques such as Principal Components Analysis (PCA) and Mahalanobis Distance analysis, which make crack detection viable for the lap-joint configuration.

1.3.1 Analytical Work

Conventional eddy current techniques have existed for many years, facilitating defect identification using sinusoidal excitation [11]. Pulsed eddy current, which uses a square pulse excitation, is emerging as a viable inspection technique that can alleviate some of the shortcomings of ET stated earlier in this thesis. However, PEC signal analysis is normally conducted in the time domain rather than the typical impedance plane display used in conventional ET [14]. PEC signal analysis techniques are not well developed, which has limited their use in present-day research.

The earliest work concerned with transient eddy currents was conducted by Wwedensky [19] in 1921. Eddy currents arose from the application of an abrupt magnetic field change that was applied to ferromagnetic materials such as iron. Although inaccurate in his assumptions (violating Gauss's Law of magnetism [10] [20]), Wwedensky's work formed the foundation of early work on transient electromagnetic excitation. The advancement of analytical solutions for transient electromagnetic phenomena has been limited, however. While Dodd and Deeds [21] conducted analytical and experimental work concerning the sinusoidal excitation of a single coil above an infinite plane, and a single coil surrounding a rod of conducting material, the same approach cannot be applied to the case of transient excitation because of the more significant effect of feedback from the sample on coil response. Desjardins [22] has recently explored these solutions based on the approach of Dodd and Deeds [21], using the magnetic vector potential, with the additional innovations of convolution

and Fourier transforms to solve differential circuit equations formulated from three-way feedback effects between driving coil, sample and pick-up coils.

1.3.2 Crack Detection in the Presence of Fasteners

A further challenge in the aircraft industry is the inspection of components with ferrous fasteners present. The work included in removing fasteners and subsequently inspecting an aircraft wing using bolt hole eddy current (BHEC), for example, is time consuming, and introduces the risk of additional damage to the structure, as stated in Section 1.1. Therefore, it is highly desirable to find a solution that allows reliable detection of cracks in second layer aluminum structures in the presence of ferrous fasteners.

Probe design in this thesis utilizes a central driving coil wound around a ferrite core, and pick-up coils placed within close proximity of the driving coil that sense the time rate of change of the magnetic flux. Abindin *et al.* [14] utilized a shielded circular probe comprised of a ferrite core and an excitation coil with a Hall sensor at its centre, as the sensing element, to examine the effect of varying the duty cycle on the peak height of the signal in the time domain. The experiment consisted of a multi-layer aluminum sample with ferrous fasteners present. They successfully detected electric discharge machined (EDM) notches 5 mm in length, which were located in the third layer, 3 mm deep.

Recent work by Desjardins *et al.* [23] confirmed that the ferrous fastener enhances flux transmission deeper into the structure and thereby improves the potential for defect detection in second layer aluminum structures. Since the fasteners are ferromagnetic they will be strongly magnetized with application of a magnetic field [24]. Greater magnetization and longer diffusion time, cause the eddy currents induced in the first and second layer aluminum to persist for a longer period of time and penetrate further into the structure than if the ferrous fastener was not present [23].

Work conducted by Whalen [2] investigated the effect of ferrous fasteners on the detection of discontinuities extending from a hole in multi-layer aluminum samples. This work utilized a Central Driver Differential Pick-up (CDDP) probe, which consists of a central driving coil wound around a ferrite core and four pick-up coils wound on 1 mm ferrite cores, located at 90° intervals, around the driving coil. The ferrite core of the driving coil magnetized the fastener, allowing for deeper penetration of flux into the sample. The pick-up coil pairs, which were connected differentially and

located either 90° or 180° apart, sensed the resulting time domain flux changes. The sample consisted of a ferrite fastener, with head diameter of 7 mm, centrally located in a stack of 2024-T3 aluminum plates, with a 9 mm long notch cut into the bore hole, located at various depths in the stack. Whalen [2] determined that with a 6 mm ferrite core, the 9 mm notch was detectable at a depth of 3.2 mm. Increasing the diameter of the ferrite core to 8 mm, which is 1 mm larger than the diameter of the fastener head, increased the detectable depth to 6.4 mm. This increased depth of penetration was attributed to the greater amount of flux in the fastener provided by the larger ferrite core. However, the configuration of a fastener in a central hole in a plate is not representative of the lap joint structure, which has effects due to the edge. The lap-joint used in the present work has ferrous fasteners placed approximately 2.45 cm apart, within 1 cm of an edge (see Figure 21). Cracks also emanate in multiple directions around the fastener making it impossible to ignore edge effects. Therefore, this work employs the use of a probe with four coil pairs (eight coils in all), to compensate for the presence of an edge and variable crack propagation directions, eliminating the need to rotate the probe.

Finite Element Modeling (FEM) conducted by Babbar *et al.* [25] for the transient CDDP probe utilized in the work by Whalen [2], provided a good visual depiction of magnetic flux penetration through the ferrous fastener, as shown in Figure 3. The magnetic flux produced by the driver coil was pushed further into the sample by the fastener, thereby generating induced currents deeper in the conducting aluminum plates, consistent with Desjardins *et al.* [23]. The FEM successfully simulated the transient response to a crack emanating from a fastener hole in the aluminum plate with the fastener present, and was able to accurately model a 9.5 mm crack up to a depth of 4.8 mm. The modeling provided a good representation of how the fastener acts as a pathway for the flux created by the driving coil.

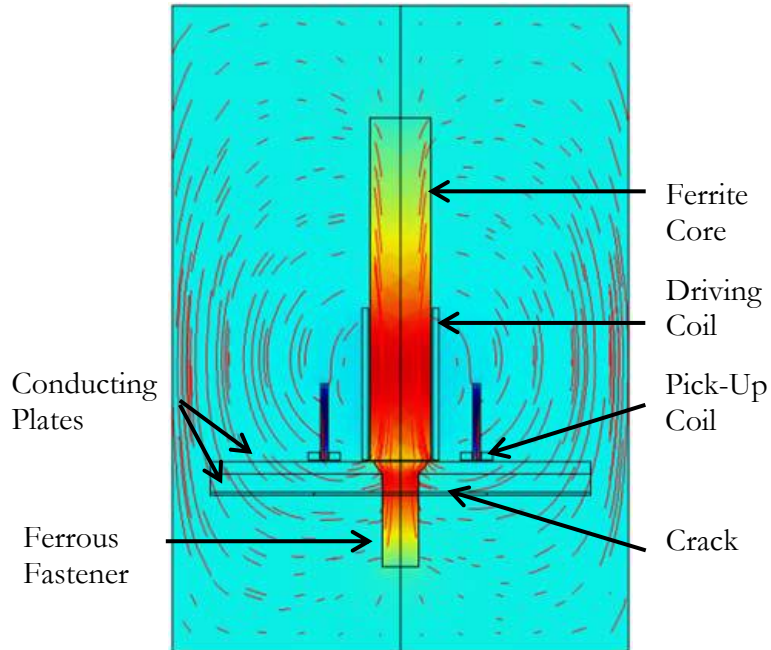


Figure 3: Front view of a solved 3D finite element half-model showing flux penetration through the ferrous fastener (CDDP Probe design) [25].

Recent work performed by Horan [26] addressed the issue of PEC inspection for stress corrosion cracking (SCC), through carbon fiber reinforced polymer (CFRP). The conductivity for CFRP is essentially zero. Cracks emanated from around ferrous fasteners, and travelled span wise, fastener to fastener, in the inner wing spar of the CF-188. The inner wing spar consists of a layer of 7.5 - 20 mm (0.3 - 0.8 inch) thick CFRP, where the spar is attached underneath, using ferrous and non-ferrous fasteners. SCC in the inner wing spar occurs between fasteners, which are located approximately 25 mm apart. Horan [26] [27] successfully detected cracks at large lift-off using coil-based probes, which utilized a central driving coil wound around a ferrite core, and Giant Magneto-resistive (GMR) sensors. GMR and coil sensor signals were analyzed using PCA.

1.3.3 PEC Signal Analysis

The response signals in PEC techniques provide information about the presence of potential defects. Three commonly used methods of characterizing signals are shown below in Figure 4: time-to-peak, peak amplitude and zero-crossing time [28]. Time-to-peak amplitude has provided defect depth information in multi-layered structures [12]. He *et al.* [18] conducted experiments using differential coils and Hall probes, showing that the peak amplitude of the response signal yields information about the defect volume and that the zero crossing time yields information about the

depth of the defect [18]. Their work [18], utilizing time domain analysis of signal feature characteristics, proved to be satisfactory as surface and subsurface defects were detected.

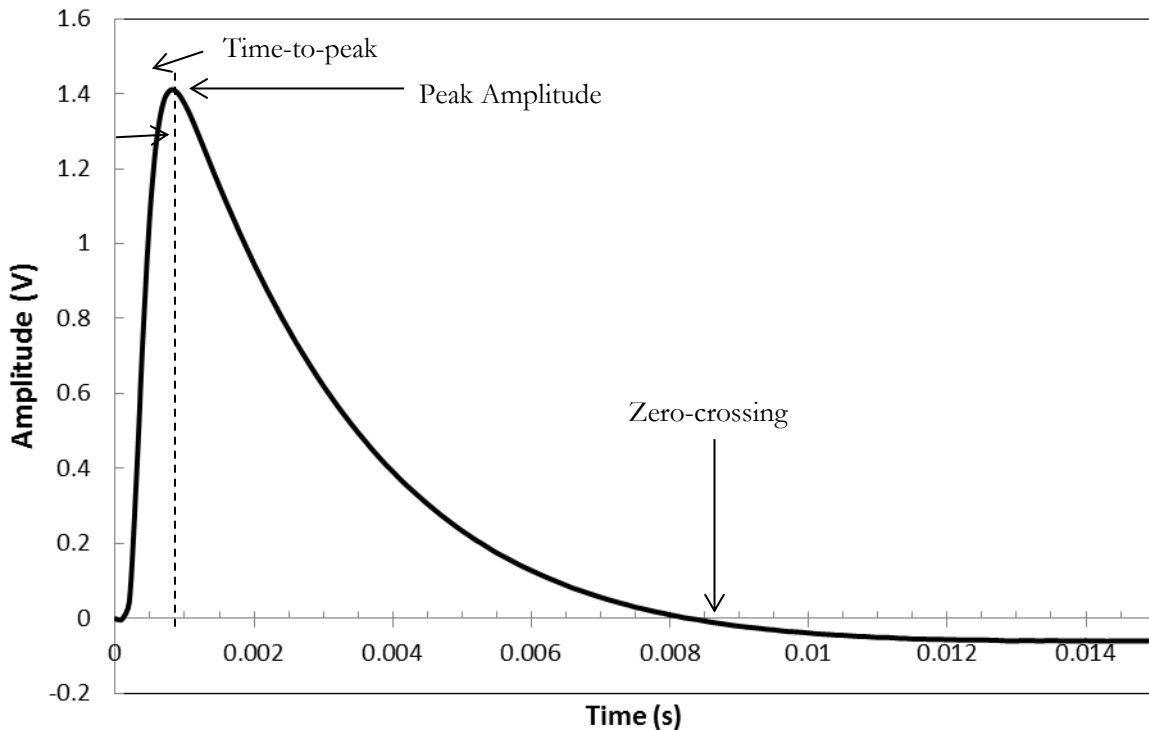


Figure 4: Typical PEC signal with common signal response analysis.

While these signal analysis techniques have been successful in defect detection in past studies, it becomes increasingly difficult to distinguish between signals with defects present from those without defects, when the signals do not vary by an easily measurable amount. A plot of four signals from four fasteners, which were obtained using the experimental methodology to be detailed in Section 3, are shown in Figure 5. Two of the signals were obtained from fasteners that contain defects in the second layer, while the other two signals were obtained from fasteners that do not contain defects. It is challenging to distinguish between the signals using peak amplitude analysis, because the peaks do not follow a discernable trend, as shown in the close up view of the peaks in Figure 6. In addition, zero crossing time cannot differentiate between the signals because the signals are very similar, as shown in the close up view of Figure 7. Therefore, in order to detect the minute changes between signals with and without notches, it would be useful to employ a technique that is sensitive to small changes between the signals. Such a potential method is Principal Components Analysis (PCA).

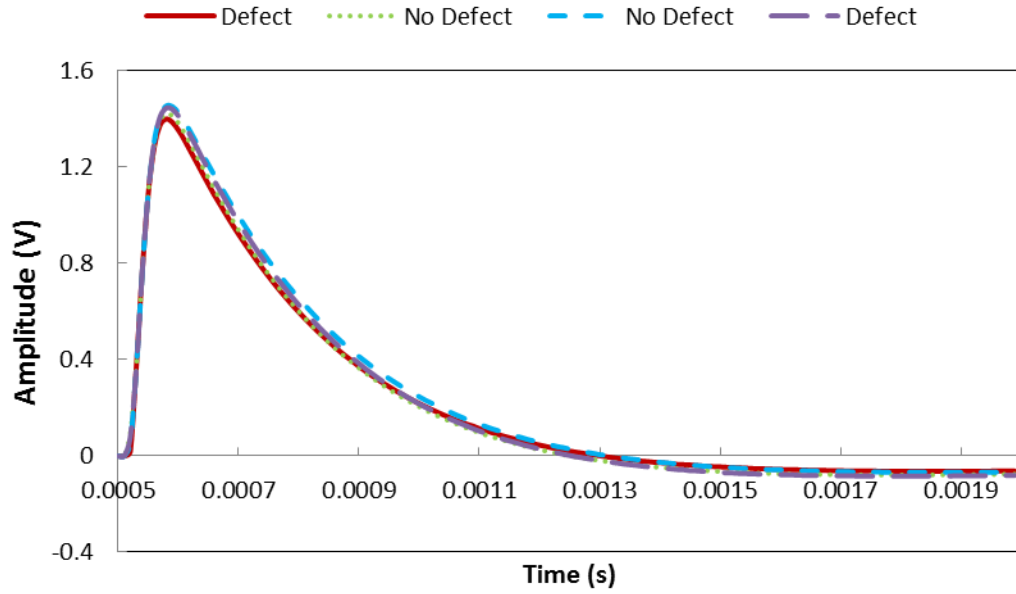


Figure 5: Time domain response from four fasteners, with and without notches.

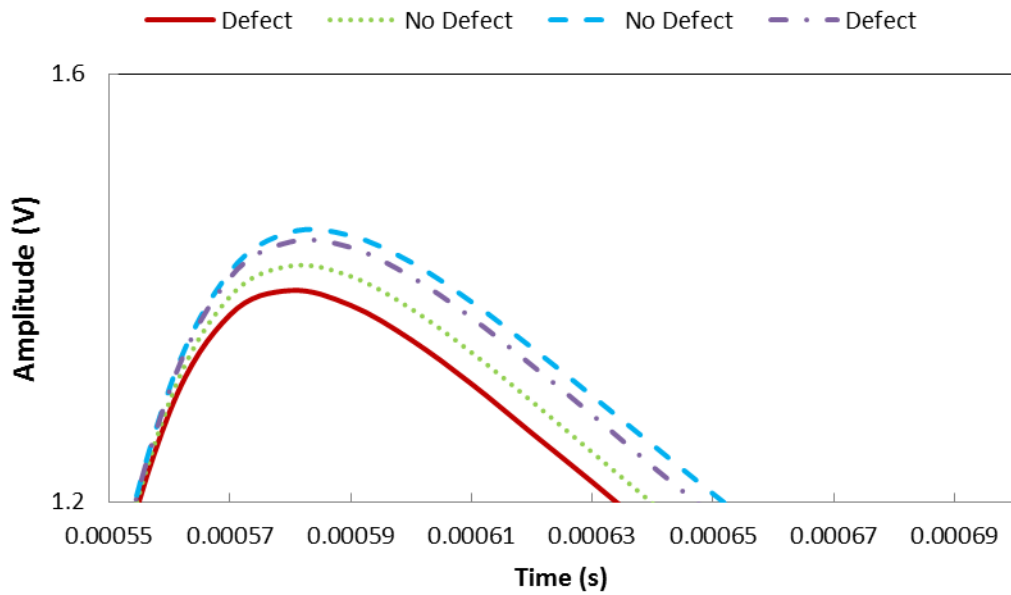


Figure 6: Zoomed view of peaks from Figure 5.

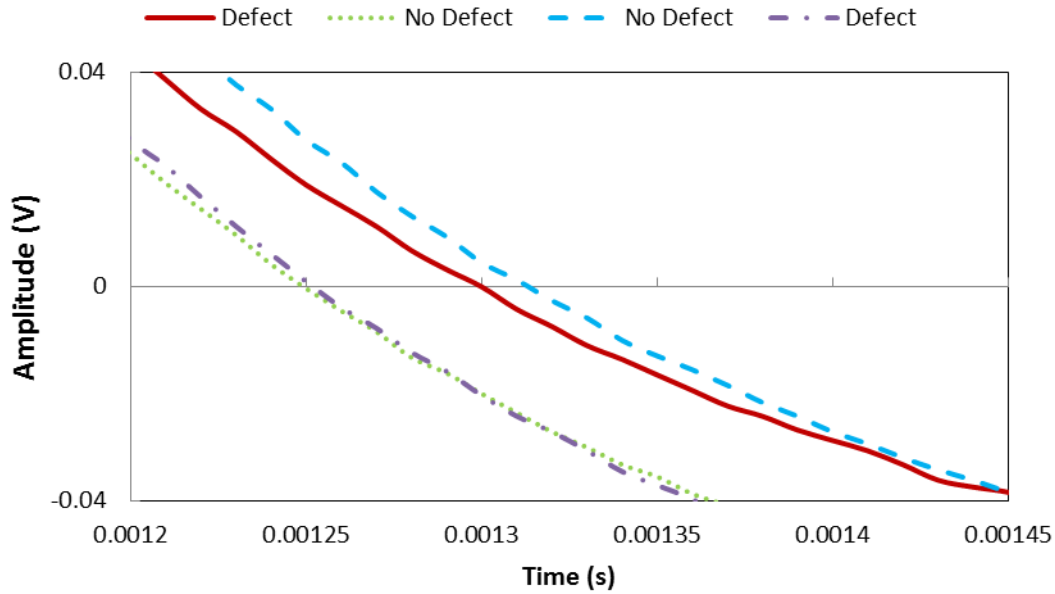


Figure 7: Zoomed view of zero-crossing from Figure 5.

1.3.4 PEC signals and Principal Components Analysis

Interpretation of the data gathered by PEC techniques can be used to characterize defects. However, the time-domain signal characteristics of PEC are not amenable to the identification of small differences in signals obtained in the presence and absence of cracks, as discussed above in Section 1.3.3. Advances have been made in the interpretation of the data by using modified PCA [16]. PCA is a statistical technique that reorients highly correlated multivariate data so that the first few dimensions account for as much of the available information as possible, making visualization of the data more straightforward and subsequent data analysis more manageable [17]. PEC signals are considered multivariate because the data contains more than one dependent variable [17]; i.e. the signals are comprised of many sources of information such as the peak height, signal decay time and zero-crossing points. Typical PEC analysis of aircraft components may produce multiple signals, which contain between 100 and 1000 data points each. When data sets become unmanageable in size, PCA can be used to compress the data into scores and vectors [17]. PCA scores can then be investigated for correlation with a desired variable. In this thesis, the controlled dependent variable is the presence of a defect. PCA has been applied in many different applications such as facial recognition [29] and fault detection for semi-conductor manufacturing [30]. These multivariate

processes are not necessarily similar to PEC in theory, but are similar in the size of data set to be analyzed and the correlated nature of the data.

Recent research using modified PCA techniques, [16] [27] [31] [32], concludes that PCA is an effective method of analyzing results from a PEC probe. The traditional PCA uses an average signal subtraction, whereas the modified version does not use this signal subtraction [16]. Recent work using PCA has been performed by Horan *et al.* [16] [26] [27] and Underhill *et al.* [31] for crack detection in CF-188 inner wing spars. A modified PCA method was used to identify signal variation due to the presence of notches originating at fastener bore holes. The signals' PCA scores, which are based on the second and third eigenvectors of the PCA, provided the necessary discrimination to separate signals when notches were present from signals obtained from no-defect sites [16].

FEM conducted elsewhere [32], utilized the probe design in this thesis work, which is shown in Figure 8 and described in detail in Section 3.2. FEM investigated the effectiveness of PEC in detecting deep lying cracks of different sizes and orientations in multi-layer aluminum structures, utilizing PCA for signal analysis. The FEM simulated the response of a differential PEC probe to top and bottom layer notches around a ferrous fastener. FEM demonstrated that PEC signals are strongly influenced by the presence of an edge or slot, as shown in Figure 8, and by small probe displacements, especially along the length of the crack. PCA was employed to reduce the signals to scores and vectors, where the first and third scores yielded the clearest crack detection results [32].

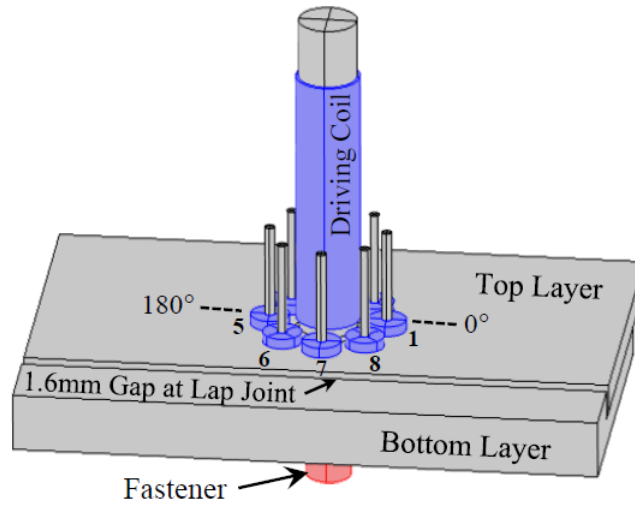


Figure 8: Sample and probe geometry used in FE models [32].

1.3.5 PCA and Mahalanobis Distance

As stated previously in Section 1.3.4, discriminant analysis has been used to create separation between PCA scores, obtained using the PEC technique, from fasteners with notches at their bore, and fasteners without notches at their bore [27]. Scores from cracked (or notched) sites congregated to one side of the cluster of scores from un-cracked sites. However, recent FEM [32] showed that, in this thesis work, both crack orientation and size affects score position, i.e. scores from one crack orientation will be rotated relative to scores from another crack orientation (in the multi-dimensional score space) and discriminant analysis will not provide the necessary separation for detection of cracks in multiple orientations. An alternative approach is to apply a quantitative measure of the distance between groups, regardless of direction, to distinguish between cracks and non-cracks (blanks). To accomplish this, a statistical technique called cluster analysis, specifically Mahalanobis Distance (MD) analysis [17], is applied to the PCA scores. MD, which establishes the statistical separation between sets of scores from similar objects, is used in conjunction with PCA to make the distinction between signals with and without cracks more obvious. MD has been used in health monitoring of electronic products [33], and also in combination with conventional eddy current examination of nuclear fuel cladding for flaw indications [34], but has not presently been used to interpret PCA scores for defect identification.

1.4 Objective

The aim of this thesis is to investigate the feasibility of pulsed eddy current technique to detect cyclic fatigue cracking around ferrous fasteners in the second layer of lap joints. An 8-coil differential array probe was used and the results analyzed using principal components analysis (PCA) and Mahalanobis distance (MD) analysis. The CP-140 aircraft engineering office has determined that the minimum detectable crack size in the lap-joint structure is 0.76 mm (0.03 in), in the transverse direction [9].

1.5 Thesis Scope and Methodology

Section two presents the electromagnetic theory involved in the generation of eddy currents followed by a description of the statistical theory pertaining to principal components analysis. Next, the cluster analysis technique called Mahalanobis Distance is presented, as well as the Hotelling T^2 threshold theory [35] for determining confidence intervals associated with crack detection.

Section three describes the experimental set-up. The first step is to describe the coil-based probe design, and the sensing equipment set up. Next, the single fastener test piece and multiple fastener test pieces are described in detail, including the material, crack lengths, orientations and locations. Finally, the experimental procedures for each test piece case and the signal processing are explained including the analysis method of signal gating.

Section four presents the results from the measurements conducted on the single fastener test piece, and how the PCA scores are affected by off-centering the probe over the fastener, and by the presence of a notch.

Section five presents the results of measurements taken on the three multiple fastener test pieces, the NAVAIR sample, Test Piece #1 and CP-140-TT-1B. Effects on PCA scores due to off-centering, presence of a notch, the height of the fastener head and lift-off, the effect due to the edge of aluminum, and the effect due to fastener distance to the edge are presented. Next, the process used for eigenvector selection is presented using logistic regression analysis. Finally, crack detection results for the NAVAIR sample and test piece #1 are presented for both the absolute and differential modes. Following this the results for the Aurora test piece (CP-140-TT-1B) are presented in differential mode.

Section six discusses the performance of PEC technique combined with the PCA process for second layer crack detection. A comparison with FEM is performed, and the similarities in results are identified. Possible sources of uncertainty are also presented.

Section seven discusses the conclusions of this work, as well as recommendations for future work to make this technique field-viable for second layer crack detection.

2 Theory

2.1 General

The aim of this Section is to first provide an overview of conventional and pulsed eddy current inspection theories followed by a development of the physical principles for PEC inspection techniques using electromagnetic theory. Maxwell's Equations are presented to explain how electromagnetic fields behave in conducting materials. Next, charge dissipation in a conductor will be explained for pulsed eddy current techniques. The theory surrounding principal components analysis is presented, followed by a derivation, as PCA is used to help reduce the signal data quantity to a manageable amount. The output PCA scores are then used to calculate the Mahalanobis Distance, which is compared to a decision threshold, based on reliability analysis, calculated using the Hotelling T^2 theory [35].

2.2 Maxwell's Equations

In order to understand the principles behind eddy current inspection, the electromagnetic equations describing this phenomenon must be examined. We begin with an outline of Maxwell's four Equations [10]:

$$\nabla \cdot \mathbf{E} = \frac{\rho}{\epsilon} \quad (2.1)$$

$$\nabla \times \mathbf{E} = -\frac{\partial \mathbf{B}}{\partial t} \quad (2.2)$$

$$\nabla \cdot \mathbf{B} = 0 \quad (2.3)$$

$$\nabla \times \mathbf{B} = \mu_o \mathbf{J} + \mu_o \epsilon_o \frac{\partial \mathbf{E}}{\partial t} \quad (2.4)$$

where \mathbf{E} is the electric field, \mathbf{B} is the magnetic field, \mathbf{J} is the current density, ρ is the charge density, ϵ is the permittivity and ϵ_o is the permittivity and μ_o is the permeability, both of free space. Equation 2.1 is referred to as Gauss's Law, equation 2.2 is referred to as Faraday's Law, equation 2.3 indicates

that lines of flux are closed on themselves (no monopoles) and equation 2.4 is Ampere's Law with Maxwell's correction.

Inside material, for linear and homogeneous media (uniform conductivity, permeability and permittivity), the following relationships are valid [10]:

$$\mathbf{H} = 1/\mu \mathbf{B} \quad (2.5)$$

$$\mathbf{D} = \epsilon \mathbf{E} \quad (2.6)$$

$$\mathbf{J} = \sigma \mathbf{E} \quad (2.7)$$

where \mathbf{H} is the magnetic field intensity and is related to the magnetic field by the permeability, μ . The electric displacement, \mathbf{D} is related to the electric field \mathbf{E} by permittivity. Equation 2.7 is referred to as Ohm's Law, and is applicable in the conductors to be considered and states that the current density is related to the electric field by the material's conductivity (σ) [10]. Maxwell's equations in matter have the form [10]:

$$\nabla \cdot \mathbf{E} = \frac{\rho_f}{\epsilon} \quad (2.8)$$

$$\nabla \times \mathbf{E} = -\frac{\partial \mathbf{B}}{\partial t} \quad (2.9)$$

$$\nabla \cdot \mathbf{B} = 0 \quad (2.10)$$

$$\nabla \times \mathbf{B} = \mu\sigma \mathbf{E} + \mu\epsilon \frac{\partial \mathbf{E}}{\partial t} \quad (2.11)$$

2.3 Electromagnetic Waves in Conductors

The flow of charge cannot be controlled within a conductor, and according to Ohm's Law (equation 2.7), the current density is proportional to the electric field. Ampere's law and Gauss's Law are used to derive the continuity equation, which by the Law of Conservation of Charge [10] (charge cannot

be created nor destroyed), states that the divergence of the current density is equal to the negative rate of change of the charge density, and is expressed as [10]:

$$\nabla \cdot \mathbf{J}_f = -\frac{\partial \rho_f}{\partial t} \quad (2.12)$$

where \mathbf{J}_f is the free current density. Applying equations 2.7 and 2.8 to equation 2.12 yields [10]:

$$\frac{\partial \rho_f}{\partial t} = -\sigma(\nabla \cdot \mathbf{E}) = -\frac{\sigma}{\epsilon} \rho_f \quad (2.13)$$

For homogeneous linear media, a solution to equation 2.13 is [10]:

$$\rho_f(t) = -e^{-\frac{\sigma}{\epsilon}t} \rho_f(0) \quad (2.14)$$

Any free charge will dissipate in some characteristic time, $\tau \equiv \frac{\epsilon}{\sigma}$, meaning that any free charge on a good conductor will flow out to the surface. For a perfect conductor, where conductivity is effectively very large, $\tau = 0$. In good conducting materials (i.e. copper and aluminum), it is noted that the characteristic time for free charges to dissipate is extremely fast, and is on the order of $\tau = 10^{-14} \text{ s}$ [37], therefore, $\rho_f = 0$. This reduces equation 2.8 to $\nabla \cdot \mathbf{E} = 0$.

2.4 Diffusion Equations

Next, the equations representing how electric and magnetic fields flow out of a conductor will be derived. Applying the curl operator [10] to equation 2.9 yields:

$$\nabla \times (\nabla \times \mathbf{E}) = -\nabla \times \frac{\partial \mathbf{B}}{\partial t} \quad (2.15)$$

Using the following vector identity, where \mathbf{A} is an arbitrary vector [10]:

$$\nabla \times (\nabla \times \mathbf{A}) = \nabla(\nabla \cdot \mathbf{A}) - \nabla^2 \mathbf{A} \quad (2.16)$$

One can apply equation 2.16 to equation 2.15 to yield:

$$\nabla(\nabla \cdot \mathbf{E}) - \nabla^2 \mathbf{E} = -\frac{\partial}{\partial t} (\nabla \times \mathbf{B}) \quad (2.17)$$

Using the result from the previous section ($\nabla \cdot \mathbf{E} = 0$), equation 2.11 can be substituted on the right hand side of equation 2.17 to yield:

$$\nabla^2 \mathbf{E} = \frac{\partial}{\partial t} \left(\mu\sigma \mathbf{E} + \mu\epsilon \frac{\partial \mathbf{E}}{\partial t} \right) \quad (2.18)$$

Rearranging, equation 2.18 becomes:

$$\nabla^2 \mathbf{E} = \mu\sigma \frac{\partial \mathbf{E}}{\partial t} + \mu\epsilon \frac{\partial^2 \mathbf{E}}{\partial t^2} \quad (2.19)$$

Equation 2.19 is Maxwell's modified wave equation [10]. A similar solution can be obtained for the magnetic field \mathbf{B} so that it is expressed independently of the electric field:

$$\nabla^2 \mathbf{B} = \mu\sigma \frac{\partial \mathbf{B}}{\partial t} + \mu\epsilon \frac{\partial^2 \mathbf{B}}{\partial t^2} \quad (2.20)$$

In good conductors, when the conductivity is very large, the following approximation can be used. Copper has a conductivity of 5.8×10^7 siemens-m⁻¹ [10], the multiplication of $\mu\sigma$ will be on the order of 72.9, while the multiplication of $\omega\mu\epsilon$, where ω is the radial frequency associated with the changing fields, will be on the order of $\omega \times 1.112 \times 10^{-17}$. The second term in equations 2.19 and 2.20 can be neglected because of the dominating first term, for frequencies less than approximately 10^8 Hz. A parabolic diffusion equation for the electric and magnetic fields remains [37]:

$$\nabla^2 \mathbf{E} = \mu\sigma \frac{\partial \mathbf{E}}{\partial t} \quad (2.21)$$

$$\nabla^2 \mathbf{B} = \mu\sigma \frac{\partial \mathbf{B}}{\partial t} \quad (2.22)$$

These two equations are similar to the equation for heat diffusion, and they express how the electric and magnetic fields diffuse into the conductor.

2.5 Charge dissipation in a conductor

For an abruptly applied field (a pulsed field) Ohanian [37] suggests that in order to reach equilibrium within the conductor, three steps must be achieved:

1. Expulsion of free charges,
2. Currents and dynamic electric and magnetic fields are expelled, and;
3. Surface currents and wave fields are damped.

Ohanian determined that a crude estimate of solutions to equation 2.22 would be [37]:

$$\frac{\partial \mathbf{B}}{\partial t} \approx \frac{\mathbf{B}}{\tau_D} \quad (2.23)$$

$$\nabla^2 \mathbf{B} \approx \frac{\mathbf{B}}{l^2} \quad (2.24)$$

where l is the characteristic length. Combining these two equations with equation 2.22 yields [37]:

$$\tau_D \approx \mu \sigma l^2 \quad (2.25)$$

where τ_D is the characteristic diffusion time in seconds. The general solution to the diffusion equation (equation 2.22) is of the form [13]:

$$\mathbf{B} = f(e^{-t/\tau_D}) \quad (2.26)$$

The magnetic and electric fields will flow out of the volume of the conductor in some characteristic diffusion time, which has a reasonable dependence on conductivity and permeability. Therefore, as the conductivity increases, so will the diffusion time.

2.6 Skin Depth Theory

For the particular case of a surface coil above a thin conducting plane, Krause *et al.* [13] found that equation 2.25 can be represented as:

$$\tau_D = \mu \sigma D T \quad (2.27)$$

where the square of the characteristic length from equation 2.26 has been substituted by T which is the thickness of the plate, and D is a fit parameter connected to coil dimensions (diameter of the ferrite core and also the pickup coil inner diameter).

A transient skin depth, denoted δ , can be inferred from equation 2.26 for a uniformly applied field above a conducting half-space, and is represented as [13]:

$$\delta = \sqrt{\frac{\tau_D}{\mu\sigma}} \quad (2.28)$$

Comparatively, the skin depth equation for conventional eddy current testing, in good conductors (where $\mu \gg \omega\epsilon$), is approximated as [10]:

$$\delta = \sqrt{\frac{2}{\mu\sigma\omega}} \quad (2.29)$$

2.7 Eddy Current Generation

The generation of eddy currents in electrically conductive materials is based on Faraday's Law (equation 2.9) where a changing magnetic field induces an electric field, or electromotive force (emf), ϵ . Using the curl theorem [10], the emf can be expressed as:

$$\epsilon = \oint \mathbf{E} \cdot d\mathbf{l} = - \int \frac{\partial \mathbf{B}}{\partial t} \cdot d\mathbf{a} \quad (2.30)$$

The magnetic field is related to the magnetic flux, Φ , by the area integral $\Phi = \int \mathbf{B} \cdot d\mathbf{a}$ [10]. Therefore, equation 2.30 can be expressed as:

$$\epsilon = - \frac{d\Phi}{dt} \quad (2.31)$$

The emf generated opposes the change in magnetic flux, denoted by the minus sign in equation 2.31, also known as Lenz's Law [10]. The changing magnetic flux induces eddy currents in the conductive

material, which are sensed via coils, and the net change in coil current or voltage is analyzed during eddy current NDT.

2.8 Equivalent Circuit Diagram

Pulsed eddy current testing begins with the application of a voltage to an excitation coil, which is excited by a step function. While the voltage is applied instantaneously, the current through the excitation coil's wire rises exponentially to a limit based on inductance effects of the coil. The excitation coil, with self-inductance L and resistance R , in the absence of a sample or pick-up coil, can be represented by a simple R-L circuit, shown below in Figure 9, with constant voltage V at time $t=0$, when the switch is closed.

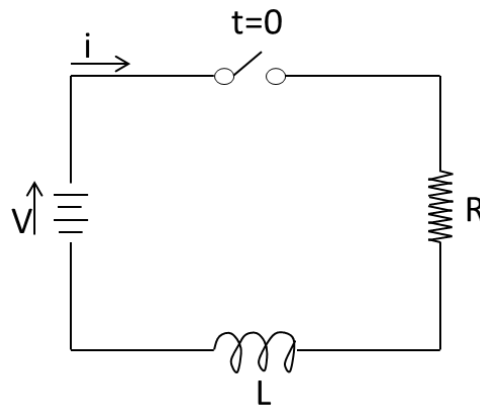


Figure 9: RL circuit representing excitation coil.

Using Kirchhoff's voltage law [10], the sum of voltages around the loop must equal zero, resulting in the following differential equation:

$$V - iR - L \frac{di}{dt} = 0 \quad (2.32)$$

After the switch is closed, the current will build up until some steady state is reached. Equation 2.32 can be solved for $t=0$ to be the following:

$$i(t) = \frac{V}{R} \left(1 - e^{-\frac{R}{L}t} \right) \quad (2.33)$$

At $t=0$, the rise in current is almost instantaneous, and levels out at V/R , as shown in Figure 10. This simple circuit representation shows the primary time dependence associated with the excitation field involved in eddy current testing.

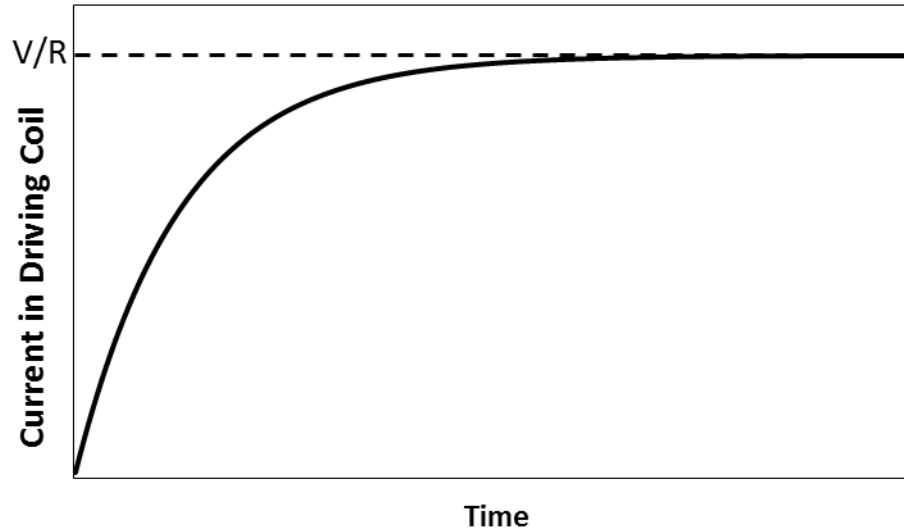


Figure 10: Current in driving coil representing equation 2.33.

To more closely model the actual experiment conducted in this thesis, a second coil (loop 2) may be added to the circuit diagram, which is shown in Figure 11, and all the parameters are defined in Table 1.

Table 1: Description of parameters for Figure 11.

Parameter	Description
L_1	Driving coil self-inductance
R_1	Driving coil resistance
i_1	Current through driving coil
M_{12}	Mutual inductance
L_2	Pick-up coil inductance
R_2	Pick-up coil resistance
i_2	Current in pick-up coil
V_o	Input Voltage

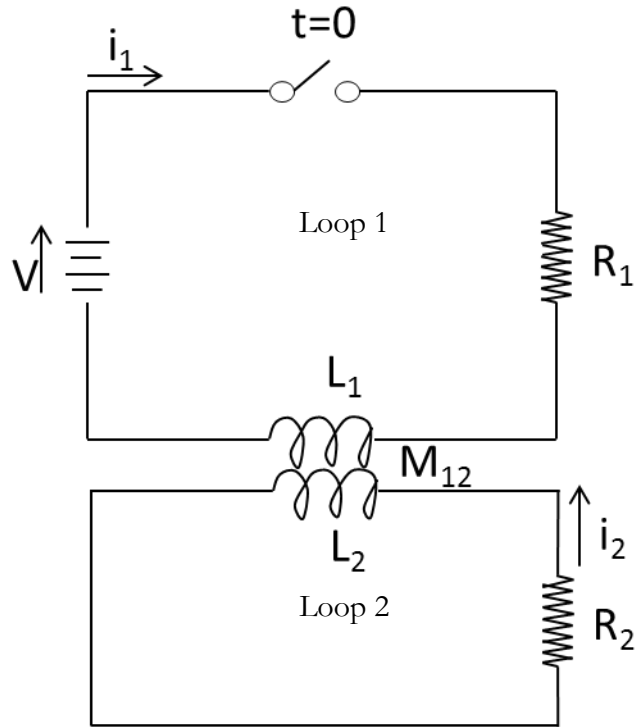


Figure 11: Equivalent circuit diagram for driving coil and pick-up coil.

When the second circuit is introduced in proximity to the first, a mutual inductance coupling occurs between them. Applying Kirchhoff's Second Law to Figure 11 yields [38]:

$$L_1 \frac{di_1}{dt} + R_1 i_1 = M_{12} \frac{di_2}{dt} + V_0 U(t) \quad (2.34)$$

$$L_2 \frac{di_2}{dt} + R_2 i_2 = M_{12} \frac{di_1}{dt} \quad (2.35)$$

where all parameters are described in Table 1 and $U(t)$ defines the step function. Applying the Laplace transformation to equations 2.34 and 2.35, rearranging and solving those equations for the current in loop 2 will yield [38]:

$$i_2(t) = \frac{M_{12} V_0 (e^{-\alpha_2 t} - e^{-\alpha_1 t})}{(\alpha_1 - \alpha_2)(L_1 L_2 - M_{12}^2)} \quad (2.36)$$

where the relaxation times α_1, α_2 are [38]:

$$\alpha_1, \alpha_2 = \frac{(L_1 R_2 + L_2 R_1) \pm \sqrt{(L_1 R_2 + L_2 R_1)^2 - 4R_1 R_2 (L_1 L_2 - M_{12}^2)}}{2(L_1 L_2 - M_{12}^2)} \quad (2.37)$$

The current response in the pick-up coil i_2 is represented by the curve shown in Figure 12.

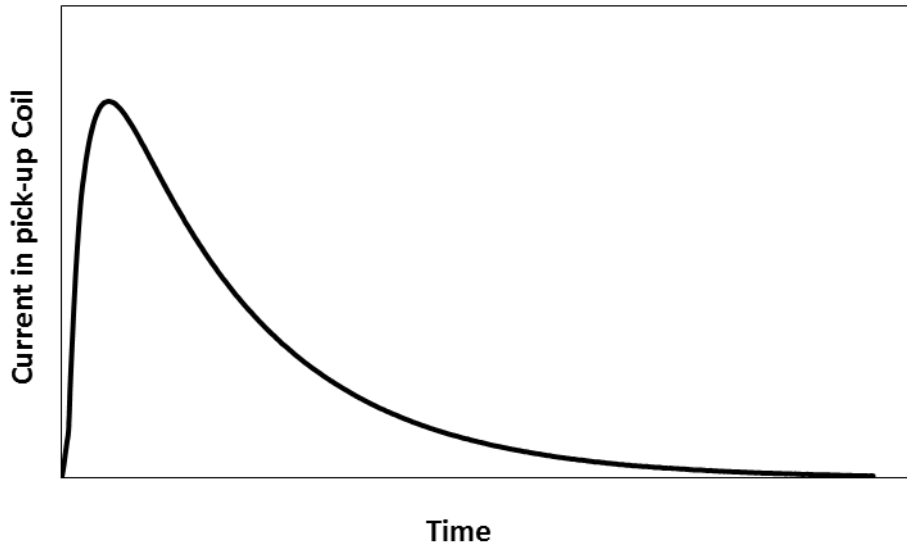


Figure 12: Current response in pick-up coil representing equation 2.36 (i_2).

The system can be further characterized by adding a third circuit to represent the sample. The mutual inductance relationships become inherently more complicated with the addition of the third circuit, as shown in Figure 13, and in addition, boundary value solutions describing diffusion of electric and magnetic fields into the sample, as expressed by equations 2.21 and 2.22, are required. The mutual inductance equations are not solved in this thesis work.

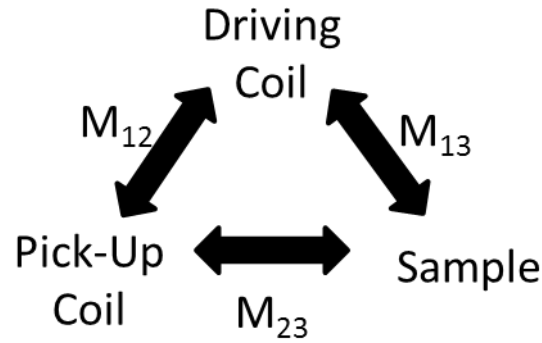


Figure 13: Three-way mutual inductance relationships between driving coil, pick-up coil and sample.

2.9 Principal Components Analysis (PCA)

2.9.1 General

As described previously in Section 1.3.4, Principal Components Analysis (PCA) is a statistical technique used to re-express multivariate data sets, thereby reducing their dimensionality, making it inherently easier to identify patterns in the measured results, which maximize the explained variation.

PCA can provide a means to determine the causes for variation within the signal such as: probe misalignment over fastener, distance to edge of material, material thickness, varying fastener head height, lift-off and presence of a defect. Notably, it is the presence of the defect that is most important to this thesis work. Sophian *et. al* [39] have shown that PCA performed better than the traditional methods of signal analysis for feature extraction such as peak height and arrival time.

2.9.2 PCA Method

The goal of PCA is to find a linear combination of the original data with the maximum variation [17]. The modified PCA method uses a least-squares method of finding the best set of basis vectors to represent the original signal, without average signal subtraction. Assume a data set is comprised of multiple signal measurements containing the same number of data points, \mathbf{Y} . \mathbf{Y} can be represented by a matrix with n rows (data points) and p columns (measurements), a column vector of which is \mathbf{Y}_i . Ultimately, the aim of PCA is to find a column vector, \mathbf{v} , that does the best job of representing a set

of p measurements with n data points, \mathbf{Y} , in a least squares sense, where the column vector \mathbf{Y}_i can be approximated by the column vector \mathbf{U}_i :

$$\mathbf{U}_i = s_i \mathbf{v} \quad (2.38)$$

The goal is to choose a \mathbf{v} that minimizes the sum of squared residuals (denoted SSR) where:

$$SSR = \sum_{i=1}^n \sum_{j=1}^p (Y_{ij} - U_{ij})^2 = \sum_{i=1}^n \sum_{j=1}^p (Y_{ij} - s_j v_j)^2 = \sum_{i=1}^n \sum_{j=1}^p Y_{ij}^2 - 2 \sum_{i=1}^n \sum_{j=1}^p Y_{ij} s_j v_j + \sum_{i=1}^n \sum_{j=1}^p s_j^2 v_j^2 \quad (2.39)$$

The coefficient s_i in equation 2.38 is referred to as the principal component score of a signal \mathbf{Y} . Next, it is assumed that \mathbf{v} can be normalized by:

$$\sum_{i=1}^n v_i v_i = \mathbf{v}^T \mathbf{v} = 1 \quad (2.40)$$

The coefficient, s_i , can be obtained by the scalar product of the transpose of \mathbf{Y} and \mathbf{v} to yield:

$$s_i = \sum_{k=1}^n Y_{ki} v_k \quad (2.41)$$

where Y_{ki} is the k^{th} element of \mathbf{Y}_i . Equation 2.41 can be expressed in matrix notation by:

$$\mathbf{s} = \mathbf{Y}^T \mathbf{v} \quad (2.42)$$

Substituting equation 2.41 into the second term of equation 2.39 yields:

$$SSR = \sum_{i=1}^n \sum_{j=1}^p Y_{ij}^2 - 2 \sum_{j=1}^p s_j^2 + \sum_{i=1}^n \sum_{j=1}^p s_j^2 v_j^2 \quad (2.43)$$

Applying the normalized condition of equation 2.40 to the last term in equation 2.43 reduces it to $\sum_{i=1}^p s_j^2$, therefore, equation 2.43 further reduces to:

$$SSR = \sum_{i=1}^n \sum_{j=1}^p Y_{ij}^2 - \sum_{j=1}^p s_j^2 \quad (2.44)$$

In order to minimize the SSR, we must maximize the second term of equation 2.44. The second term of equation 2.44, subject to the condition of equation 2.40, can be expressed as:

$$\sum_{j=1}^p s_j^2 = \mathbf{s}^T \mathbf{s} = \mathbf{v}^T \mathbf{Y} \mathbf{Y}^T \mathbf{v} \quad (2.45)$$

This constrained optimization problem can be solved by forming the Lagrangian [17]:

$$\Lambda = \mathbf{v}^T \mathbf{Y} \mathbf{Y}^T \mathbf{v} - \lambda (\mathbf{v}^T \mathbf{v} - 1) \quad (2.46)$$

where λ is the Lagrange multiplier. Taking the derivative of equation 2.46 with respect to \mathbf{v} yields:

$$\frac{d\Lambda}{d\mathbf{v}} = 2\mathbf{Y} \mathbf{Y}^T \mathbf{v} - 2\lambda \mathbf{v} \quad (2.47)$$

Setting equation 2.47 equal to zero and solving it yields the standard equation for eigenvectors and eigenvalues [17]:

$$\mathbf{Y} \mathbf{Y}^T \mathbf{v} = \lambda \mathbf{v} \quad (2.48)$$

This shows that an eigenvector of $\mathbf{Y} \mathbf{Y}^T$ will do the best possible job at representing the column vectors in \mathbf{Y} . It therefore shows that the eigenvector with the largest eigenvalue will describe more of \mathbf{Y} than any other vector. The vectors are uncorrelated, and a linear combination of only a few eigenvectors will represent most of the variation in a larger data set.

Normally, the signal average is subtracted out of the matrix, before PCA is performed, as was done by Sophian *et. al* [39]. The modified version of PCA does not use the average signal subtraction, which makes it less sensitive to small changes in scale.

The benefit of PCA is that it only takes about four to five eigenvectors to represent 99.9% of the original signal. In contrast, a Fourier series representation of the data would require a much larger number of components to represent the data. Figure 14 below shows three curves, the first is an unmodified pick-up coil signal or the original signal, the second is the first eigenvector representation of the signal and the third is a reproduction of the original signal using the first four eigenvectors. Note that 99.9% of the original signal is represented by the 1-4 eigenvectors. The resulting scores from the PCA process describe the variation in the measured PEC signals, including the presence of defects.

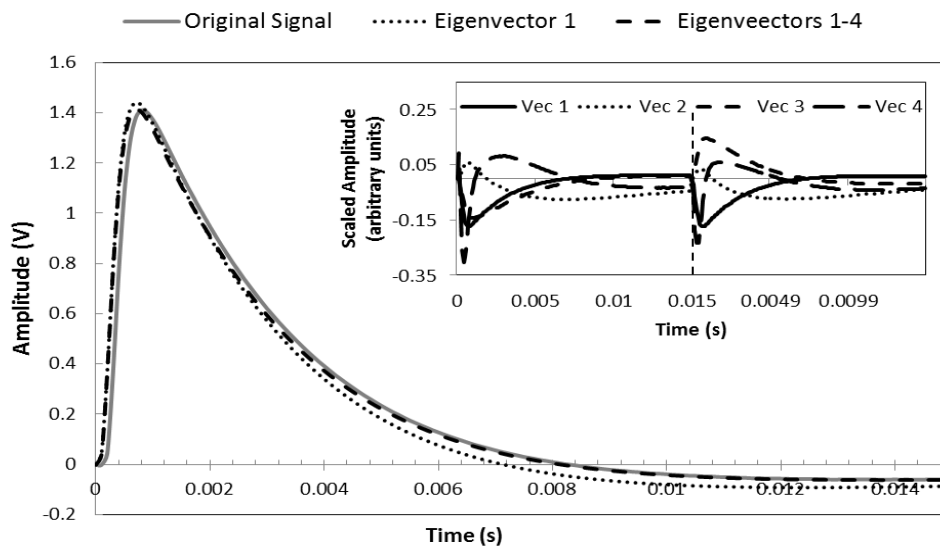


Figure 14: PEC original signal with first eigenvector reproduction, and eigenvectors 1-4 reproduction. The insert shows the four eigenvectors for each coil of the pair, used for the reproduction

2.9.3 PCA Scores

As mentioned above, the coefficients from the PCA process, s_i , are termed the principal component scores. The goal is to be able to use a few scores (1-5), instead of the 1000 data points per signal, to determine whether or not a defect is present. Figure 15 (a) is a sample 3-D representation of the second, third and fourth PCA scores, respectively, in the x, y and z axis, while (b) is a rotated view of the same scores. The figures show scores from fasteners without notches (hollow circles) and scores from notches of varying size and orientations (solid circles). It is difficult to discern from the view in Figure 15 (a), which are the fasteners with notches present at their bore, as they tend to overlap.

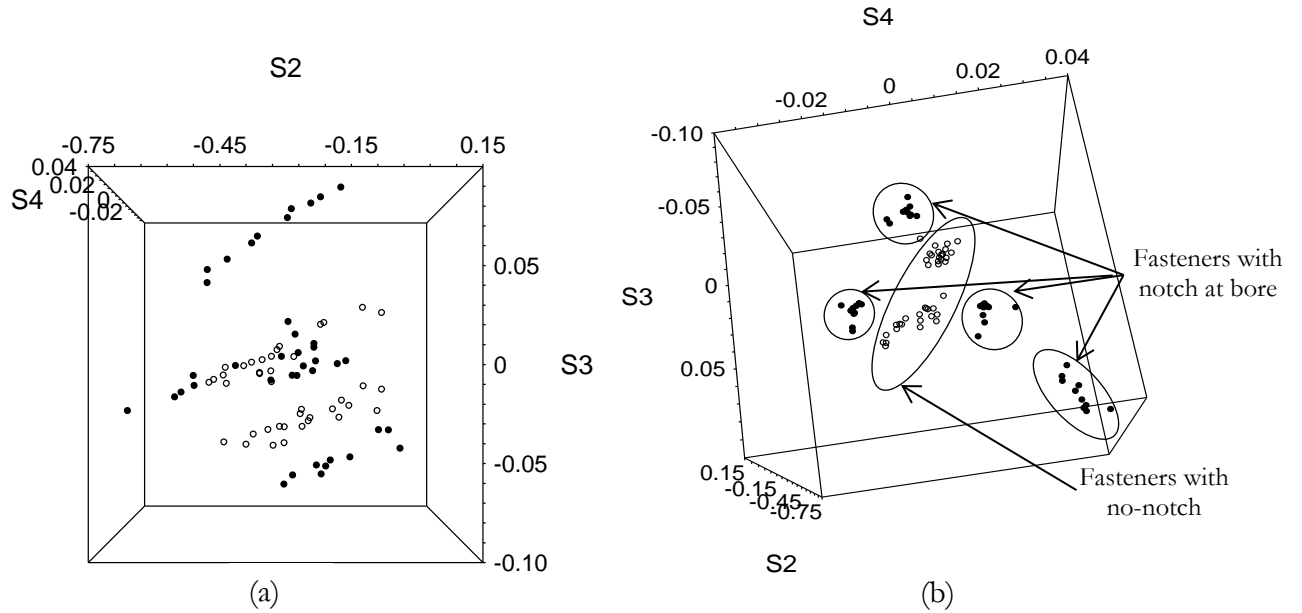


Figure 15: PCA scores viewed in 3D, in the (a) un-rotated view and (b) rotated view for fasteners with (●) and without (○) notches at their bore.

Rotating the view of the PCA scores, which is shown in Figure 15 (b), the groups of scores tend to cluster, showing separation between the groups of scores with notches from the groups of scores without notches. Each cluster is correlated with notch size and orientation.

The figures presented above yield information about the presence of defects based on the amount of separation between the groups. However, separation between clusters of scores does not always occur, and groups can overlap regardless of the view in 3-D. This problem can be overcome by using a cluster analysis, which will be described next in Section 2.10.

2.10 Cluster Analysis Method

2.10.1 Mahalanobis Distance Definition

A cluster analysis can be defined as organizing objects based on their similarities, where similar objects are placed together, and dissimilar objects are placed apart [17]. One type of cluster analysis is a distance measure called the Mahalanobis distance (MD). MD quantitatively describes the proximity of a point, y , from the centroid of a group of points, while adjusting for covariance in the data, and can be thought of as a measure of distance in standard deviations. MD can be calculated by the following equation:

$$MD = \sqrt{(\mathbf{y} - \bar{\mathbf{x}})' \Sigma^{-1} (\mathbf{y} - \bar{\mathbf{x}})} \quad (2.49)$$

where Σ is the covariance matrix of the data matrix X and $\bar{\mathbf{x}}$ is its centroid. In this case, the data matrix consists of PCA scores obtained from signals without notches present. This covariance matrix is then used to calculate MD for all available data (signals with notches and no-notch signals). Therefore, in PCA space, MD is a relative or normalized measure of a notch's distance from the center of the cluster of blanks in standard deviations. MD is then compared to a critical value, or decision threshold, in order to determine if the fastener has a notch or not. The requirement for a decision threshold will be discussed in the next Section.

2.10.2 Decision Threshold

Separating PCA scores from fasteners with notches at their bore from those without requires a threshold. Therefore, the MD^2 for each fastener is compared to a critical value, the Hotelling T^2 [35] in order to assess the potential presence of a notch around a fastener. Values greater than T^2 are interpreted as cracks within the specified confidence interval. The following equation is used to calculate the decision threshold:

$$T^2 = \frac{p(n-1)(n+1)}{n(n-p)} F_{(\alpha; p, n-p)} \quad (2.50)$$

where p is the number of PCA scores (S1, S2, etc), and n is the number of measurements used to construct the covariance matrix, calculated by the number of blanks per test piece times the number of measurements per fastener. Typically the F test, a statistical test which has an F distribution under the null hypothesis [40], at either $\alpha = 99\%$ or 95% confidence level, is used. The confidence level gives the percentage of false positives that can be expected.

2.11 Probability of False Positive (False Calls)

A false positive, or false call (term used in this work is false call), is defined as a system response interpreted as detecting a flaw when none is present at the inspection location [8]. It is difficult to define what an acceptable false call rate would be for a specific technique, as the consequences of a false call can be different depending on the type of inspection. For example, if the cost of a false positive is high, then a very low false call rate is desired due to the amount of time and money

required to re-inspect the flaw site or remove the component from service. For this work, false calls occur when a MD is calculated for a no-notch site that is greater than the specified threshold value. The total amount of false calls is a sum of these events, divided by the total number of blanks in the test piece.

3 Experimental Technique

3.1 General

This section begins by introducing the probe design used in this thesis. Next, the sensing equipment used to conduct the experiments is described by use of a flow chart. Sample characteristics are then described for the samples studied, which include: the single fastener test piece, the multiple fastener test piece considered as the NAVAIR sample, the lab fabricated samples and the Aurora test piece. The experimental technique utilized on these test pieces is then described. Finally, signal gating and processing is explained.

3.2 Coil Probe Design

The probe configuration used in this thesis is based on designs examined in previous studies [2] [15] [16], and incorporates the FEM discussed earlier in Section 1.1.1 [32] for optimization. The probe, as shown in Figure 16, incorporates a central driving coil wound around a 6 mm diameter ferrite core, chosen to match the head diameter of the fasteners. It has been determined that the magnetic flux produced by the coil is magnified in the ferrite, and that it concentrates the magnetic field near the center of the probe [23] [32]. This in turn concentrates the eddy currents near the center of the probe and thereby generates a more sensitive response [2] in the pick-up coil configuration. The orientation of the coil pairs, when placed on the aluminum, is indicated in Figure 16.

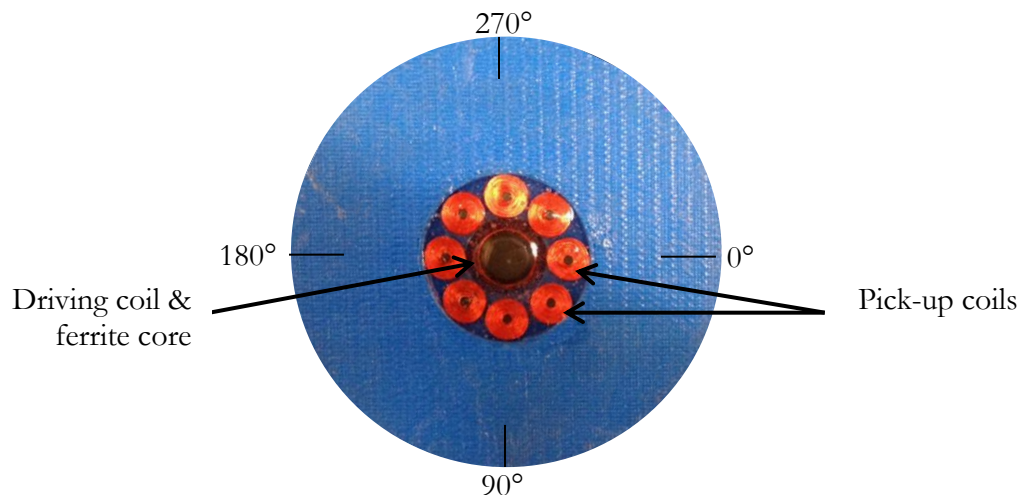


Figure 16: Probe face with central driving coil, ferrite core and eight pick-up coils.

The driving coil has 444 turns of 36 AWG wire. The driving coil and ferrite core are concentrically located inside a probe body, which was printed on a 3-D printer. There are eight 1 mm high pick-up

coils of 400 turns of 44 AWG wire centered on 1 mm diameter ferrite cores, placed within 1.5 mm of the outer diameter of the driving coil. The nearest-neighbor coil center-to-center distance is 5.6 mm. The pick-up coils are matched pairs placed 180° from one another on opposing sides of the drive coil, approximately 14.2 mm apart (center-to-center distance) and may be connected in either absolute or differential mode. In absolute mode, each coil is sampled individually, with eight separate signals collected. In differential mode, the 180° coil pairs are sampled, but the difference in their signals is collected. Therefore, in differential mode, only four signals are collected, one for each coil pair. Eight coils were used so probe rotation is not required, facilitating notch detection in multiple directions. Probe and coil information is located in Table 2. Coil-based sensing probes detect the time rate of change of the magnetic field (refer to equation 2.31) produced by the eddy currents in the aluminum.

Table 2: Driving coil and pick-up coil parameters.

Parameter	Driving Coil with 6 mm ferrite core	Pick-up Coils							
		1	2	3	4	5	6	7	8
Resistance (Ω)	13.5	33.7	35.1	35.0	35.8	33.1	34.0	35.0	34.0

3.3 Sensing Equipment

The probe cable is connected via shielded twisted pair to a custom built amplifier board and the amplified signal is digitized by a National Instruments (NI) 6361 data acquisition board at a group rate of 100 kHz. A Labview program is used to control the pulse parameters. The pulse height and width was 8.7 volts and 10 ms, respectively. Data from the pick-up coils was received through the analog input on the NI card, and then transferred to the computer for storage. The experimental process is depicted in the flow chart in Figure 17.

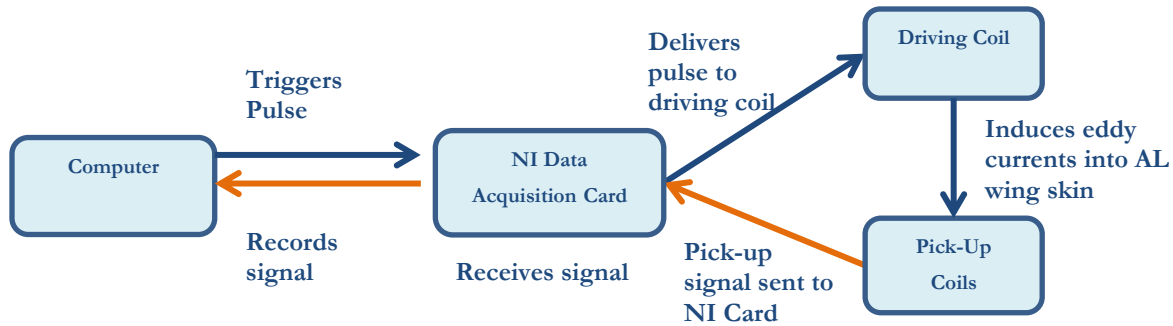


Figure 17: Flow chart depiction of sensing equipment operation cycle.

3.4 Single Fastener Test Piece

In order to understand the multiple fastener case, the single fastener case was studied because it provides information concerning crack detection, without the complications of multiple fasteners, crack sizes and orientations, and edge effects. Three 152 mm x 152 mm x 2.03 mm pieces of 2024-T3 aluminum were stacked on top of each other. A hole was drilled in the middle of the stack, and a ferrous fastener inserted to simulate an isolated fastener, as shown in Figure 18. There were three experimental cases, which consisted of the middle plate either having a notch cut into the bore hole, or no notch. The list of parameters for the experimental cases can be found in Table 3. It is noted that the material in the middle plate is not always 2024-T3, however 7075-T6 is considered electrically representative as shown in Table 3.

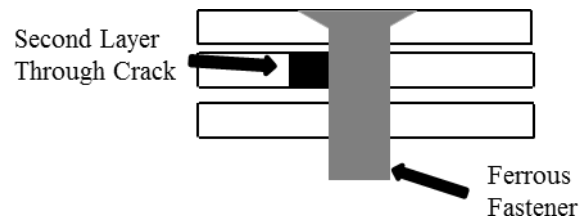


Figure 18: Side view of Single Fastener Test Piece with three plates and centrally located ferrous fastener.

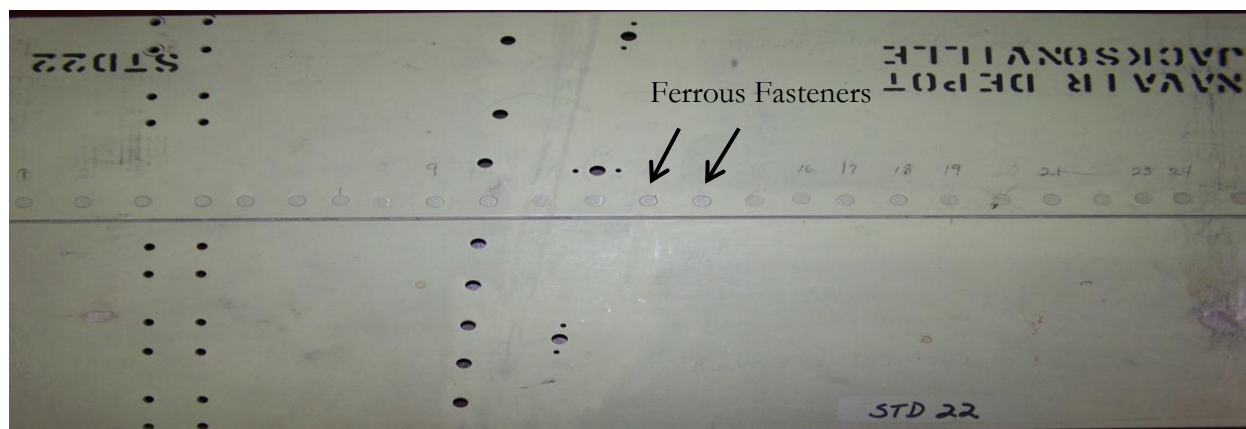
Table 3: Single fastener case experimental parameters.

Case #	Material	Notch Length (mm)	Conductivity (%IACS) ¹
1	Al 2024-T3	No notch	30.0
2	Al 7075-T6	2	31.4
3	Al 7075-T6	8	31.4

3.5 Multiple Fastener Test Pieces

3.5.1 NAVAIR Sample Description

A sample (NAVAIR depot, Jacksonville Florida) has been acquired for testing purposes, and is displayed in Figure 19 and Figure 20. The sample is based on the Lockheed P-3 Orion, which has the same airframe as that of the CP-140 Aurora. It has overall dimensions of 54 cm × 28 cm with a sheet thickness of 2.03 mm [32]. It consists of two separate sections of aluminum plates, which are joined together by a row of ferrous fasteners in a lap joint where the two plates partly overlap, as shown in the side view of Figure 20. Each fastener has a length of 15.0 mm, head diameter of 7.0 mm, shaft diameter of 4.54 mm, electrical conductivity of 3.57×10^6 S/m, and relative magnetic permeability on the order of 70 [32].



¹ http://www.ndt-ed.org/GeneralResources/MaterialProperties/ET/Conductivity_Al.pdf

Figure 19: NAVAIR sample with notches, view from top.

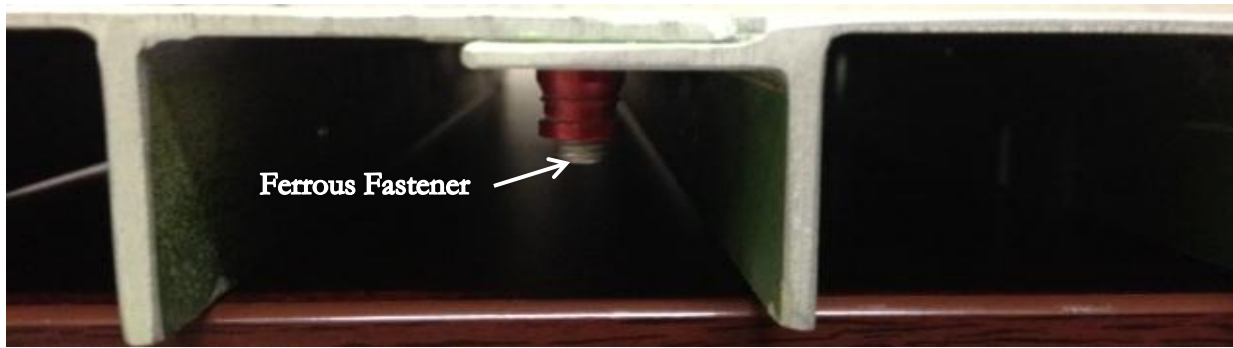


Figure 20: NAVAIR sample with view of fastener.

The NAVAIR sample has electric discharge machined (EDM) notches located in 15 of the fastener bore holes, and eight with no notches (8, 15, 16, 17, 18, 20, 22 and 23). Each notch is cut at a 45° angle to the edge of the bore hole, giving the notch a 1:1 aspect ratio. The notch orientations are based on the schematic shown in Figure 21. This sample contains fasteners with notches in the top layer, bottom layer, and three that contain top and bottom layer notches. The notch lengths and orientations are located in Table 4, where NN stands for no notch.

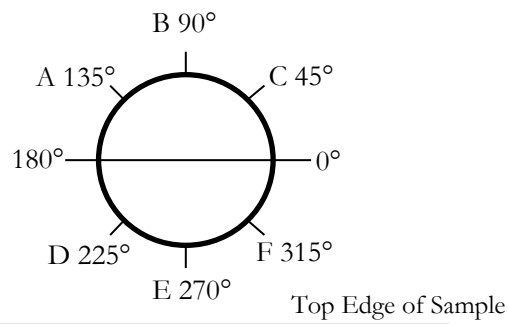


Figure 21: View from top. Notch orientation diagram.

Table 4: NAVAIR sample notch locations and lengths.

Fastener #	Bottom-of-top Layer	Top-of-bottom Layer	Notch Orientation	Actual Notch Length (mm)
1		X	A	3.30
2	X		E	1.90
3		X	D	1.78
4		X	B	0.89
5		X	C	5.46
6	X	X	F/F	3.30/0.89
7		X	E	2.03
9		X	D	1.52
10		X	A	2.79
11		X	B	0.89
12	X	X	C/D	5.46/3.30
13		X	E	1.52
14		X	F	5.08
19	X		D	2.79
21	X	X	C/C	0.89/2.79

3.5.2 Test Piece #1 Description

Using the NAVAIR sample as a template, two test pieces were constructed in the lab. The test pieces, fabricated of 2024-T3 aluminum, measure 61 cm \times 13.2 cm with sheet thickness of 2.03 mm. Twenty-nine holes of diameter 4.15 mm were drilled equidistant from each other (approximately 2.54 cm). Each fastener hole in the top layer was then countersunk 100° to a depth of 1 mm. The fasteners tested in test piece #1 were ferrous fasteners of type HL-19-5-5. Each fastener was alloy steel with a length of 8.0 mm, head diameter of 6.5 mm, and shaft diameter of 4.13 mm. The technical information about these fasteners is located in Annex A.

For each fastener hole where a notch was to be cut, a set of Webber micro accurate gage blocks (in millimeters) was used to accurately mark the notch length along the surface. Then, a jeweller's saw was used to cut notches into the bottom layer fastener holes at 45° angles, to the desired aspect ratio of 1:1, as shown in Figure 21. The width of the blade was 0.3 mm for notch lengths above 0.9 mm, and 0.17 mm for notch lengths below 0.9 mm. Afterward, notch lengths were measured to confirm the actual length using a picture microscope (with Pixel Link software). A 3.12 mm (0.125 inch) notch is shown in Figure 22, and the notch width was measured to be 0.38 mm. Notch orientations reflect those of the NAVAIR sample, as shown in Figure 21. Figure 23 below shows test piece #1,

which has ten fasteners that have no notches in the bore (# 4, 5, 7, 10, 11, 12, 13, 20, 29), and 19 fasteners that have notches in the top of the bottom layer only. Additional information concerning the parameters of test piece #1 such as notch orientation and actual notch length is shown in Table 5.

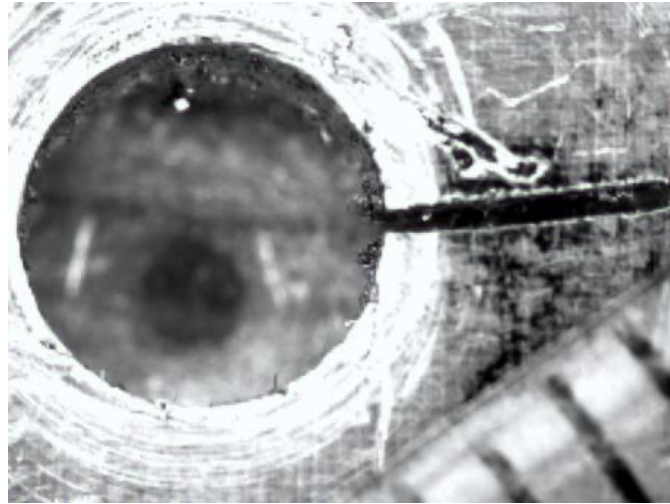


Figure 22: Microscopic photo of notch cut into fastener hole (11x magnification).



Figure 23: Picture of test piece #1.

Table 5: Test piece #1 notch parameters.

Fastener #	Notch Orientation	Actual Notch Length (mm)
2	D	1.97
3	A	1.17
6	B	1.94
8	F	1.46
9	C	1.43
14	E	3.20
15	B	3.26
16	B	1.97
17	E	1.92
18	E	0.82
19	A	1.46
21	B	2.03
22	F	1.24
23	E	0.94
24	D	1.36
25	A	1.51
26	A	1.80
27	F	2.81
28	F	0.83

3.5.3 Test Piece #2 Description

Test piece #2 was also fabricated in the lab, using the same technique as described above in Section 3.5.2. The test piece contains twenty-nine HL-19-5-5 fasteners, but does not contain any notches at the fastener bore holes. This test piece was fabricated to assess effects such as height of fastener head on PCA scores, lift off (probe above aluminum) and effect of fastener type without having the scores affected by the presence of notches.

3.5.4 CP-140-TT-1B Test Piece

A wing skin section from a CP-140 Aurora was obtained from the Aerospace and Telecommunications Engineering Support Squadron (ATESS). It has overall dimensions of 76.2 cm × 20.5 cm × 3 cm with a top sheet thickness of 2.58 mm (considerably thicker than the NAVAIR sample and Test piece #1) and a bottom sheet thickness of 2.29 mm. The sample has the same lap joint construction as the NAVAIR sample mentioned in Section 3.5.1, and is shown in Figure 24. The fasteners are of type HLT-51-6, with head diameter of approximately 7.5 mm and shaft

diameter of 4.8 mm, as per fastener specs in Annex B. The sample has EDM notches located in 21 of the fastener bore holes, and 12 with no notches (1, 2, 3, 4, 8, 12, 14, 22, 30-33). Notches can be located in either top-of-bottom layer or bottom-of-top layer. Notch orientations are similar to those outlined in Figure 21. However, for this sample, notch orientations and lengths are presented in more detail in Table 6. For fasteners that contain multiple notches at their bore, a numbering system is used (such as fasteners 16, 17, 18, 19, 21 and 28), indicated by an additional bracketed number. For fasteners that contain notches at their bore with irregular orientations (such as fasteners 9 and 19), a lettering system is used, and schematics of these notches are shown in Figure 25.

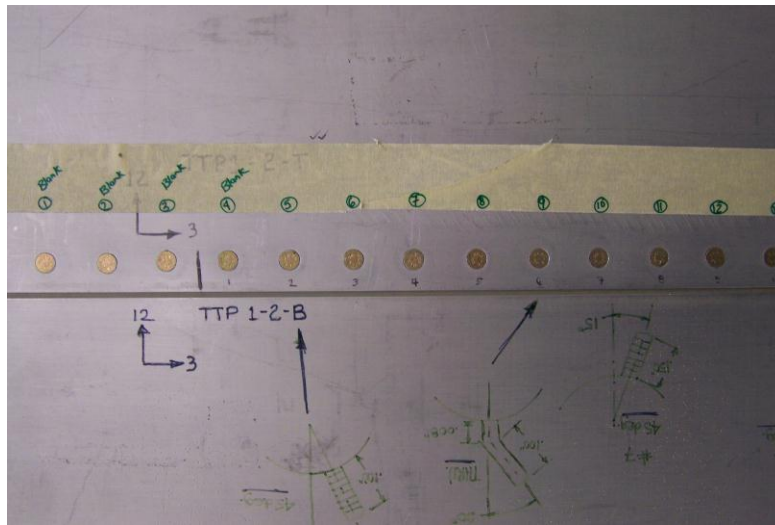


Figure 24: Picture of section of CP-140-TT-1B test piece.

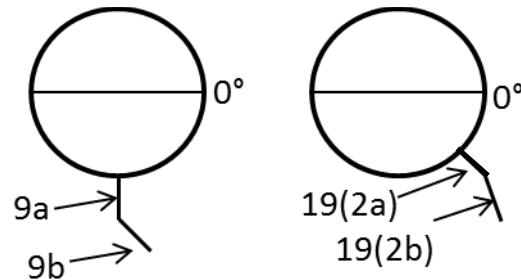


Figure 25: Schematics of notches located at fasteners 9 and 19 of CP-140-TT-1B Aurora Sample.

Table 6: CP-140-TT-1B notch parameters.

Fastener #	Bottom-of-top Layer	Top-of-bottom Layer	Notch Orientation	Actual Notch Length (mm)
5		X	315°	2.54
6	X		180°	3.30
7	X		60°	1.53
9a		X	270°	0.20
9b		X	315° from 9a	2.54
10		X	45°	3.81
11	X		105°	2.92
13	X		60°	1.72
15		X	0°	3.30
16 (1)		X	180°	2.03
16 (2)		X	90°	3.81
17 (1)	X		270°	Unknown
17 (2)		X	180°	2.03
18 (1)	X		315°	2.03
18 (2)		X	45°	2.03
19 (1)		X	270°	2.54
19 (2a)		X	330°	2.03
19 (2b)		X	30° from 19 (2a)	2.54
20	X		255°	2.54
21 (1)	X		270°	2.54
21 (2)		X	90°	2.54
23		X	75°	2.54
24	X		315°	Unknown
25		X	240°	2.92
26	X		60°	3.81
27		X	300°	1.53
28 (1)	X		300°	1.53
28 (2)		X	60°	1.53
29		X	105°	2.03

3.6 Experimental Procedure

3.6.1 Probe Alignment

Alignment of the probe over the fastener is achieved with an acrylic alignment guide, shown in Figure 26. The alignment tool has a thin clear sheet with a center hole the same size as fastener head, which is used to align the probe over the fastener head. The alignment tool, probe and sample are

shown in Figure 27. For each measurement, alignment of the probe's 0th position occurs along the row of fasteners, subsequently, the other coil pairs will then be aligned over the potential crack propagation directions. For each individual measurement, the alignment tool was removed and replaced over the fastener. This process is achieved by eye, as to best represent the actual inspection technique performed by an NDT technician. Centering errors can occur on the order of approximately 1-2 mm utilizing this technique. During laboratory experiments, multiple measurements are taken at each fastener. This ensures that variability due to probe placement is properly represented in the data set.

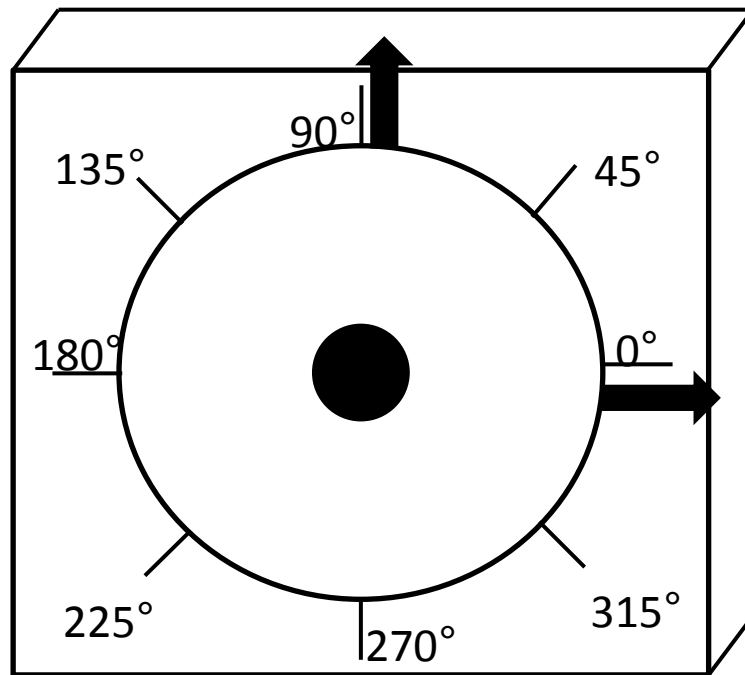


Figure 26: Alignment tool, showing the direction of shimming (0° and 90°).

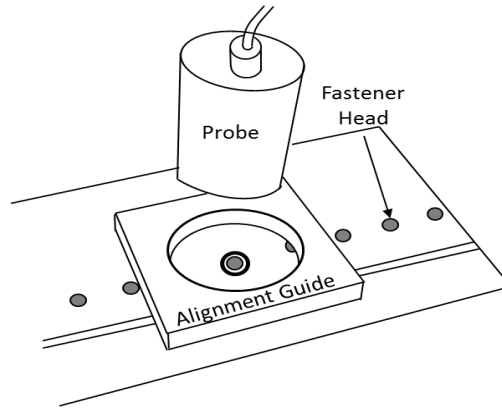


Figure 27: Probe with alignment guide and sample.

3.6.2 Single Fastener Experimental Procedure

In order to analyze the effect of certain parameters on PCA scores, experiments were performed on the single fastener sample. First, a shimming experiment was conducted to assess the effect of off-centeredness on PCA scores. The alignment tool, shown in Figure 26, was centered over the fastener, and clamped into place. This is considered the 0th case. Nine measurements were taken, one at each 45° angle (0°, 45°, 90°, 135°, 180°, 225°, 270°, 315°, 0°), and this process was repeated three times. Then, the alignment tool was shifted in either the 0° or 90° direction by an amount of 0.125 mm, 0.25 mm and 0.375 mm. For each displacement, twenty-seven measurements were taken, three at each rotation angle. Figure 26 shows the two directions in which the alignment tool was shifted (0° and 90°). The shimming experimental details are outlined in Table 7.

Table 7: Shimming experimental parameters.

Case #	Direction of Alignment Tool Shift	Displacement Amount (mm)
0	N/A	0
1	90°	0.125
2	90°	0.250
3	90°	0.375
4	N/A	0
5	0°	0.125
6	0°	0.250
7	0°	0.375

3.6.3 Multiple Fastener Test Piece Experimental Procedure

Alignment of the probe over the fastener is achieved using the procedure outlined in Section 3.6.1, for each of the four multiple fastener test pieces. The number of measurements obtained per fastener varied between test pieces, and is detailed in Table 8. As mentioned previously, multiple measurements were taken to assess variability due to probe placement, but were also used to assess repeatability of measurements.

Table 8: Number of measurements taken per test piece.

Test piece	Number of Measurements/Fastener	
	Absolute	Differential
NAVAIR	10	10
Test Piece #1	2	2
Test Piece #2	10	0
CP-140-TT-1B	0	4

3.7 Summary of Experiments

Table 9 below summarizes the tests conducted on each test piece. The results of these experiments will be presented in Sections 4 and 5.

Table 9: Summary table of experiments conducted on each test piece, in sequence.

Test Sequence	Specimen	Probe Off-Centeredness	Notch	Presence of Edge	Distance to Edge	Fastener Head Height	Lift-Off	Effect of Temperature
1	Single Fastener Test Piece	X	X					
2	Test Piece #1		X					X
3	Test Piece #2					X	X	
4	NAVAIR Sample	X	X	X				
5	CP-140-TT-1B		X		X			

3.8 Signal Processing

3.8.1 Signal Gating

Analyzing the whole signal is not appropriate for PEC responses, when PCA will be applied. Figure 28 shows a PEC signal from a fastener without a notch present. Previous experience indicates that including the rapidly changing signal between 0 and 0.00058 seconds causes the PCA to concentrate on representing the large variations in the signal that this induces. The virtually exponential decay of the signal means that there is almost no signal to analyze after 0.0015 seconds [32]. Precise determination of where the notch information is contained is difficult to achieve. The modeling reveals that the highest concentration of eddy currents, greater than 90%, occurs near the flaw site between 0.0004 and 0.001 seconds, as shown in Figure 29. For the purposes of this thesis, the signal “gating” [26] occurs from 0.00058 to 0.0015 seconds, in order to encompass the portion of the signal with the greatest amount of crack detection information.

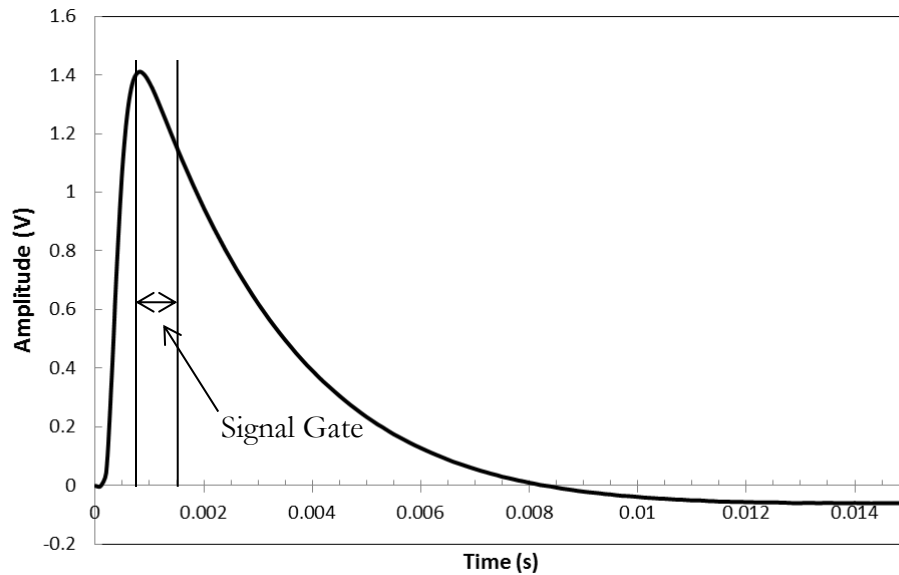


Figure 28: Raw PEC data signal from a fastener without a notch, indicating the gate.

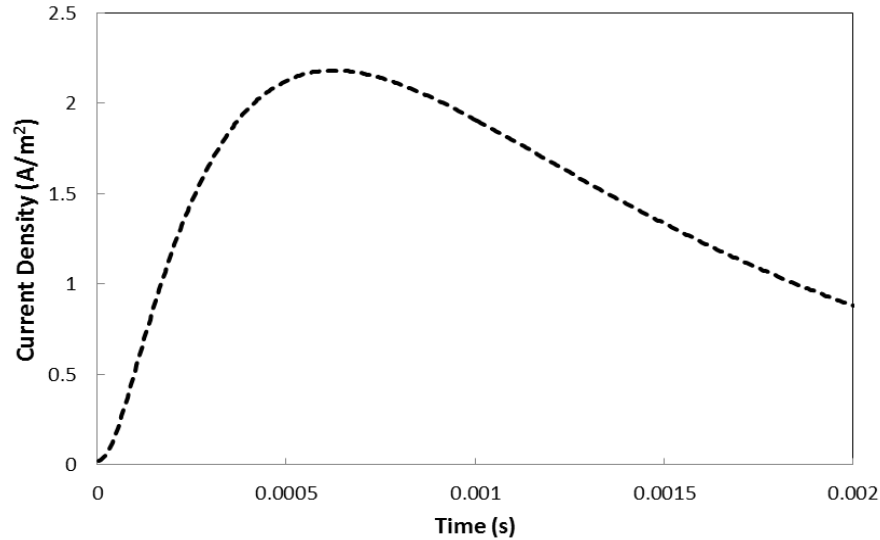


Figure 29: Eddy current density curve from finite element modeling.²

3.8.2 Signal Analysis

The modified PCA process is applied to the windowed data described in Section 3.8.1 using a Labview program. For differential analysis, the PCA scores are calculated for each of the four signals separately. The coil pairs were analyzed individually because they are not identical, and, therefore, the eigenvectors describing their response are expected to be slightly different. In absolute mode, each of the eight coils produces a response signal. The 180° coil pair signals are selected, concatenated, gated and PCA is applied to the gated data. In differential mode, four signals are produced (one for each coil pair). Therefore concatenation of the coil pairs is not necessary. The outcome of this process is a set of PCA scores for each fastener. Once the scores are obtained, the centroid and covariance matrix for the signals from blanks was determined for each coil pair. The Mahalanobis distance was then calculated for each fastener, by coil pair, using equation 2.49. The distance calculations were done on a per coil pair basis because coil pairs are not completely equivalent and so the response from each pair to a crack can be expected to be different. In addition, because the probe had a set orientation, each coil pair can be expected to have different sensitivity to a crack depending on both the crack's relative orientation to the probe and its relative orientation to the lap joint.

² FEM Courtesy of Dr. Vijay Babbar, Department of Physics, Royal Military College of Canada, Kingston, Ontario

The Mahalanobis Distance for each fastener is then compared to the threshold value, calculated using equation 2.50. Fasteners with a distance greater than the threshold are considered as having a notch present, and those below are considered blank. The results from each coil pair for each fastener were then logically ORed, i.e. a positive for one coil pair counted as a crack detected for that fastener. The data processing sequence is outlined in Figure 30.



Figure 30: Data processing sequence for PEC signals.

4 Results and Analysis of Single Fastener Case

4.1 General

This section discusses the results obtained from the single fastener test piece, and the PCA score correlation with different variables, such as off-centering, and the presence of a notch. It is desirable to isolate the different effects on the PCA scores by varying one parameter while holding the others fixed so that the most appropriate scores for notch/crack detection may be identified.

4.2 Off-Centering Effects

After collecting and recording the data in differential mode, for the cases outlined in Table 7, the PCA scores were calculated for each coil pair. The FEM [32] indicated that misalignment of the probe over the fastener head affects the PCA scores S1 and S2, the greater the displacement, the larger the PCA score becomes. In order to assess the effect of misaligning the probe over the fastener, the PCA scores were plotted against each other, in different combinations. Figure 31 is a plot of the first and second PCA scores for the single fastener with no notch present for the centered case, and for probe displacement cases of 0.125 mm, 0.250 mm and 0.375 mm. The displacement direction is indicated in each figure, and the arrows indicate the direction of increasing off-centeredness. Displacing the probe from the centered position causes PCA score S1 to become larger, as indicated by the positive horizontal shift of the points in Figure 31. Displacement of the probe over the fastener does not cause any effect on the second PCA score (S2), as there is no shift in the amplitude of the vertical axis.

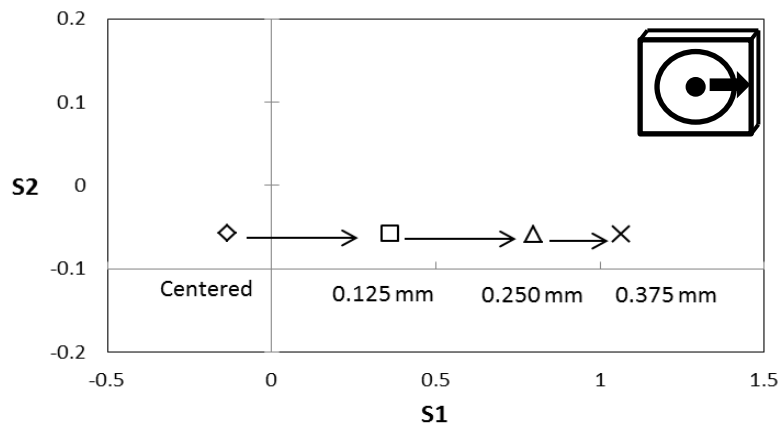


Figure 31: Plot of PCA scores S2 versus S1 for single fastener with no notch, showing off-centered results.

Figure 32 is a plot of the same test conducted as outlined in Table 7, but is a plot of the first and third PCA scores (S1 and S3). It is shown that similar to the second PCA score, the third score (S3) does not contain off-centering information, because there is no shift in the vertical axis direction as the probe center is shifted relative to the center of the fastener head. In addition, the fourth and fifth PCA scores are plotted in Figure 33, where the amplitude change in the horizontal and vertical axes is very small. Therefore, there is a minor effect of off-centering on the fourth and fifth PCA scores (1% and 3% of S1, respectively).

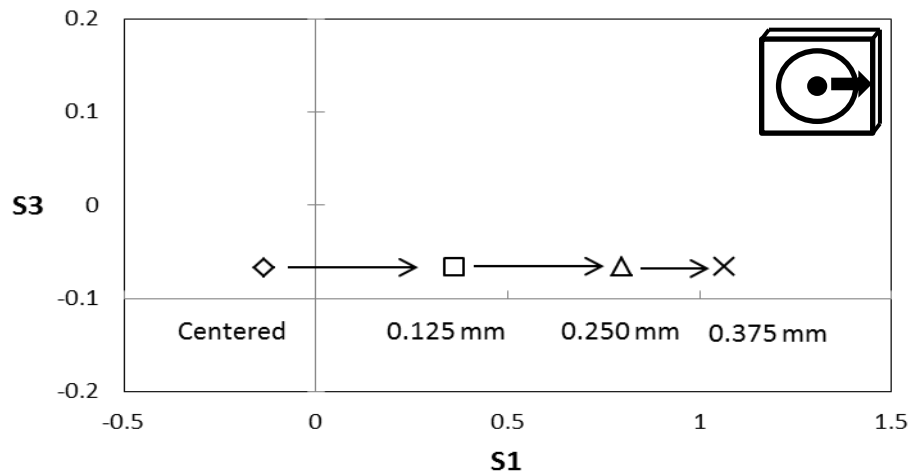


Figure 32: Plot of PCA scores S3 versus S1 for single fastener with no notch, showing off-centered results.

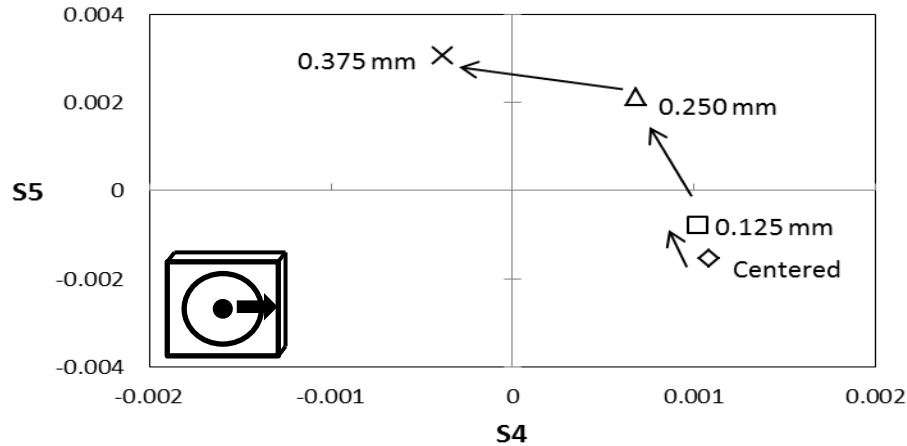


Figure 33: Plot of PCA scores S5 versus S4 for single fastener with no notch, showing off-centered results.

4.3 Notch Effects

Another correlation to be studied using PCA on PEC signals is the presence of a notch. Above in Section 4.2, the off-centering correlation is with PCA scores S1, S4 and S5, with no correlation with scores S2 and S3. These results stem from experiments conducted for three cases; the no-notch, 2 mm and 8 mm cases. The notches were through notches and located in the second layer, which was under 2 mm thick aluminum (see Section 3.4 for more detail). In addition, the notches were aligned with 0° (see Figure 26 for alignment reference). In Figure 34, the first and second PCA scores are plotted for the centered probe over the fastener for the three cases, where the arrows indicate direction of increasing notch length. In both the horizontal and vertical directions, the score values increase either positively or negatively due to the presence of the notch. In Figure 35, the second and third PCA scores are plotted for the same three cases. The effect on the second PCA score is larger than the effect on the third PCA score, but there still seems to be an effect, although minor, on S3 due to the presence of a crack. Figure 36 is a plot of the fourth and fifth PCA scores, which shows an effect on the fourth but not the fifth score due to the presence of a crack. Therefore, the first, second, third and fourth PCA scores show effects due to the presence of a crack in the second layer for the single fastener case.

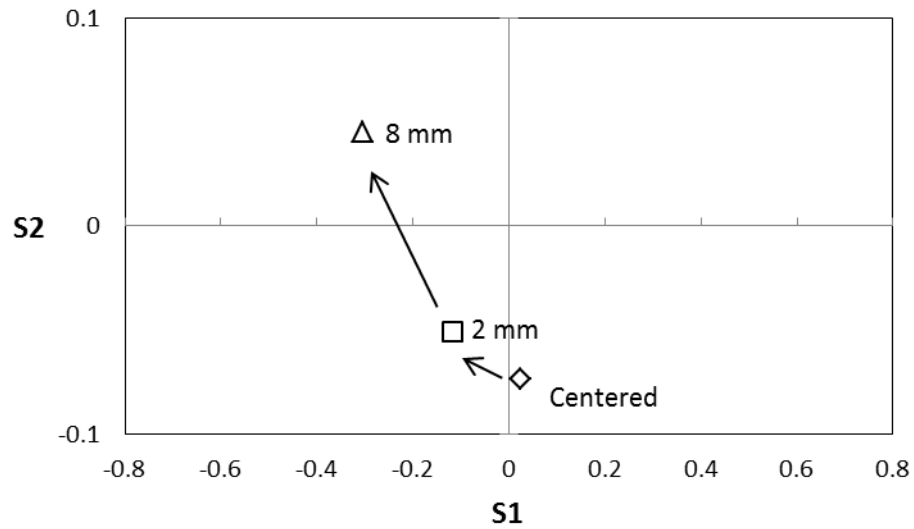


Figure 34: Plot of PCA scores S2 versus S1 for single fastener case of no notch (\diamond), 2 mm (\square) and 8 mm (Δ) notch. Arrows indicate direction of increasing notch length.

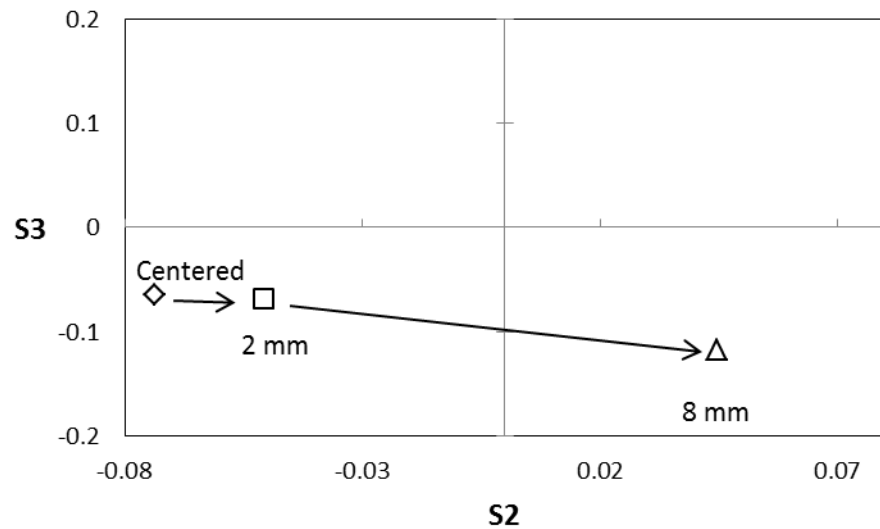


Figure 35: Plot of PCA scores S3 versus S2 for single fastener case of no notch (\diamond), 2 mm (\square) and 8 mm (Δ) notch. Arrows indicate direction of increasing notch length.

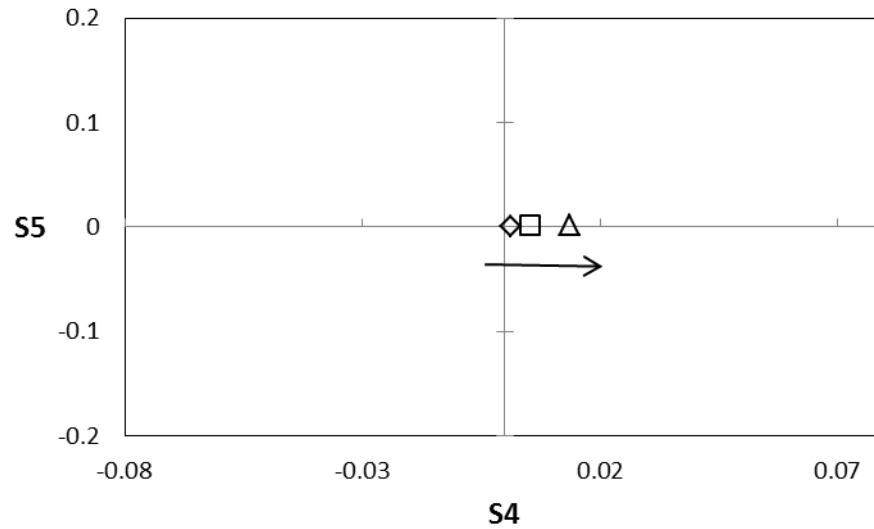


Figure 36: Plot of PCA scores S5 versus S4 for single fastener case of no notch (◇), 2 mm (□) and 8 mm (△) notch. Arrows indicate direction of increasing notch length.

Off centering and presence of a notch were the only two effects that were analysed for the single fastener test piece. These results demonstrate correlation of PCA scores with off-centeredness and presence/absence of a notch. In order to understand how other factors such as fastener head height, presence of the edge and lift-off affect the PCA scores, the multi-fastener test pieces were investigated next.

5 Results and Analysis of Multiple Fastener Case

5.1 General

This section describes the effect on the PCA scores due to off-centering, presence of a notch, height of the fastener head and lift off, presence and distance of fastener from the edge. Second, the process used for eigenvector selection is presented using logistic regression analysis. Third, crack detection results for the NAVAIR sample and test piece #1 are presented for both the absolute and differential modes. Fourth, the results for the Aurora test piece (CP-140-TT-1B) are presented for only the differential mode.

5.2 Off-Centering Effects

The off-centering effects for the single fastener test piece were presented above in Section 4.2, where PCA score S1 showed the biggest effect due to displacement of the probe. To confirm that the same effects occurred on the multiple fastener test pieces, seven experiments were conducted between two separate fasteners on the NAVAIR sample. These were fastener 1, which contained a 3.3 mm notch at 315° in the second layer, and fastener 22, no notch present. The seven experiments are outlined in Table 10, and displacement directions are outlined in Figure 26 .

Table 10: NAVAIR sample experimental cases for off-centering and notch effects on PCA scores.

Case #	Fastener	Notch Length (mm)	Displacement Amount (mm)	Displacement Direction
1	22	0	0	Nil
2	22	0	0.125	90°
3	22	0	0.250	90°
4	22	0	0.125	180°
5	22	0	0.250	180°
6	1	3.3 @ 315°	0	Nil
7	1	3.3 @ 315°	0.375	90°

Figure 37 is a plot of the first and second PCA scores (S1 and S2), from the 0° coil pair, for the experiments outlined in Table 10. It is observable on this graph in points 2-5, that displacing the probe away from the centered position (point 1, no notch present) has a large effect on the first PCA score S1, and only a very minor effect on S2. In addition, there seems to be a minor effect on the third, and fifth scores (S3 and S5) shown in Figure 38 and Figure 40, and no effect on the fourth score, shown in Figure 39. As stated previously, off-centering was correlated the most with S1 in the

single fastener case, with a weaker correlation with S4 and S5. For the multiple fastener case, off-centering effects are correlated the most with S1, and a weaker correlation was observed for S2, S3 and S5. Since the biggest effect is shown on the first score, the results are consistent with the single fastener case. The fact that more correlation with PCA scores was shown on the multiple fastener test piece can be attributed to effects due to adjacent fasteners or the presence of the edge.

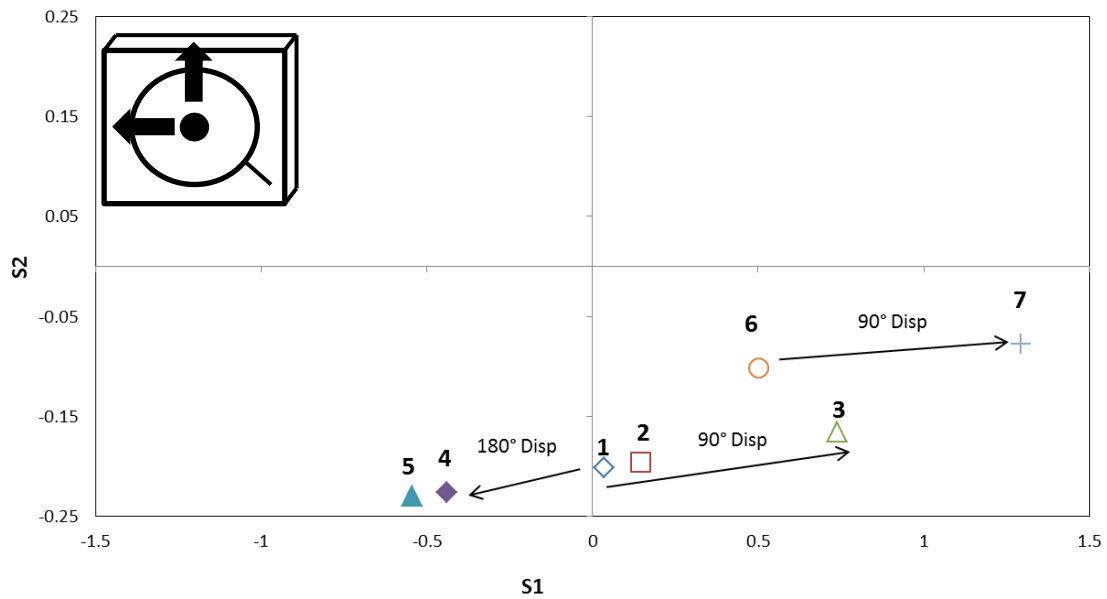


Figure 37: Plot of S2 versus S1. Numbers correspond to Table 10 cases. For probe displacement (disp), arrows indicate direction of increasing displacement.

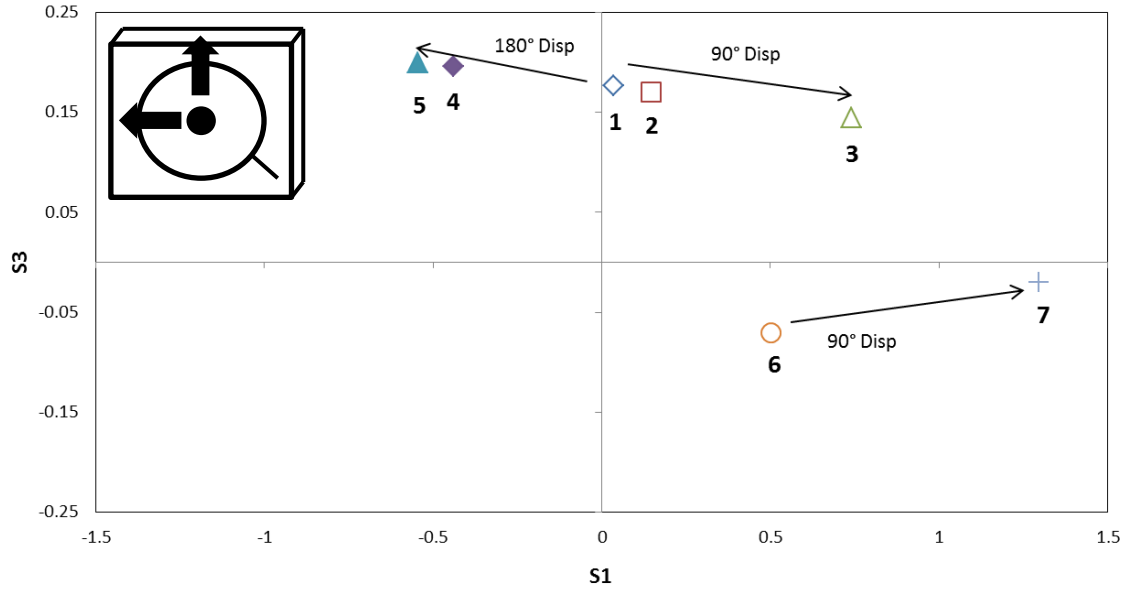


Figure 38: Plot of S_3 versus S_1 . Numbers correspond to Table 10 cases. For probe displacement (disp), arrows indicate direction of increasing displacement.

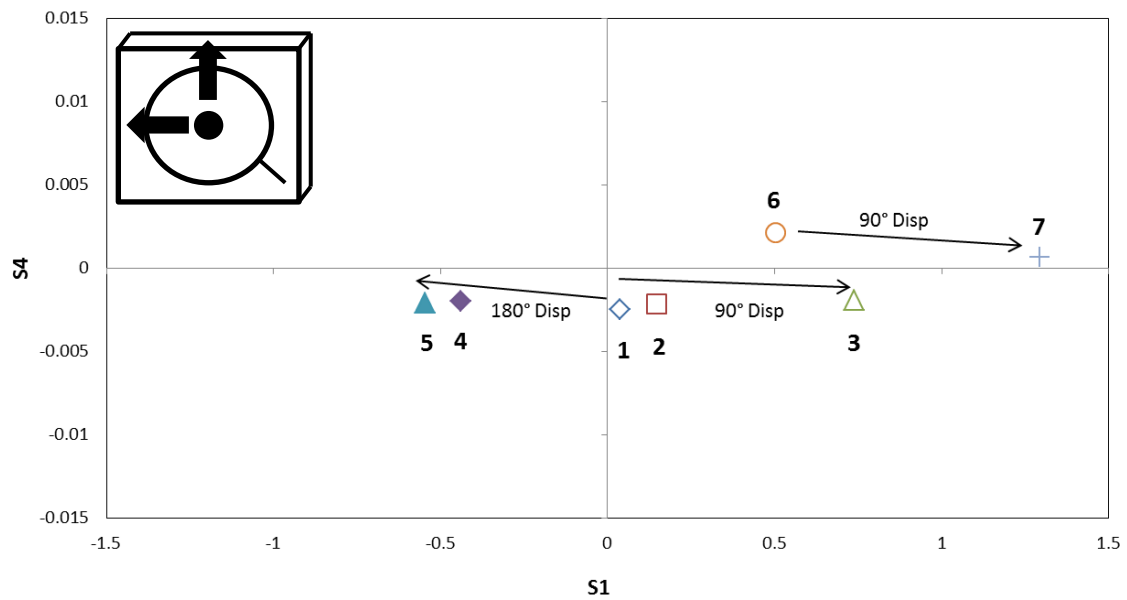


Figure 39: Plot of S_4 versus S_1 . Numbers correspond to Table 10 cases. For probe displacement (disp), arrows indicate direction of increasing displacement.

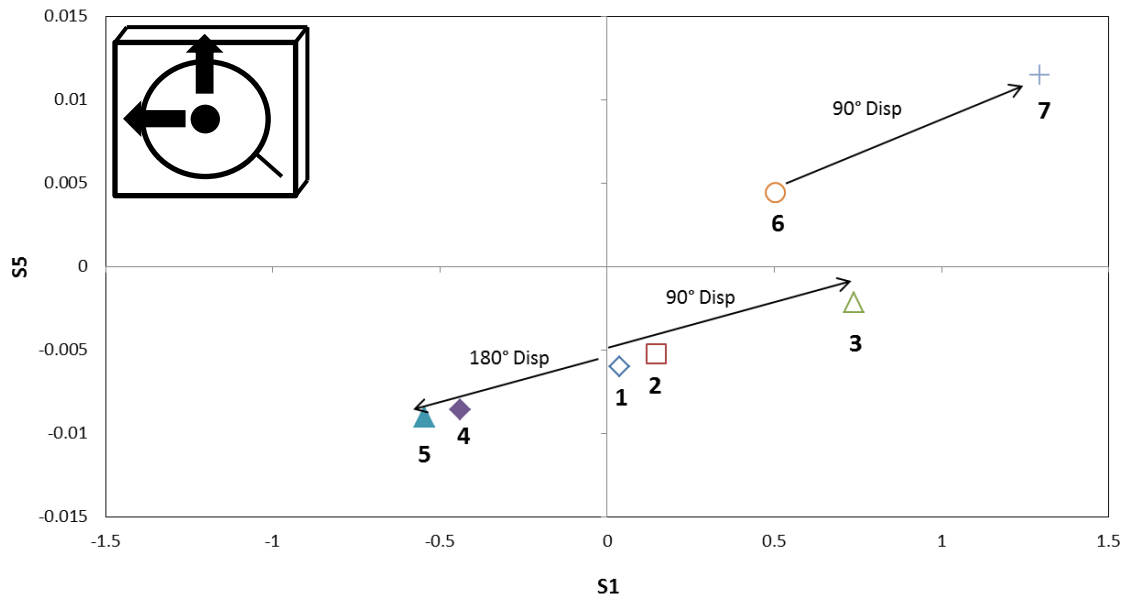


Figure 40: Plot of S5 versus S1. Numbers correspond to Table 10 cases. For probe displacement (disp), arrows indicate direction of increasing displacement.

5.3 Notch Effects

Again, considering the results of the single fastener case presented in Section 4.3, the presence of a notch tended to correlate with the first and second scores, with minor correlation with the third and fourth PCA scores. Considering point number 6 in Figure 37, which was measured for a 3.3 mm notch with no displacement, correlation is observed with the first score S1, and a weaker correlation with the second (S2). For the same point (6) in Figure 38, there is an observed correlation with PCA score S3 due to the presence of a notch, while in Figure 39 and Figure 40, there is a weak correlation with S4 and S5. Clearly there are similarities between the single fastener case and the multiple fastener case, but the differences may be attributed to the presence of adjacent fasteners or the presence of the edge.

5.4 Effect Due to Height of Fastener Head and Lift-Off

Additional variables affecting the transient response are the height of fastener head relative to the aluminum surface, and the height of the probe above the aluminum surface, considered as lift-off. Results from the investigation of effect of height of fastener head relative to the aluminum surface

are presented in the next section. Subsequently, effects due to lift-off are then presented in Section 5.4.2.

5.4.1 Fastener Head Height Effects

While this variable is not a large factor on actual aircraft, since fastener holes are countersunk with high precision, it was a factor in lab settings, as it is challenging to countersink fastener heads with a high degree of accuracy, while fabricating test pieces (Test piece #1 and #2). The height of the fastener heads relative to the aluminum was measured on Test Piece #2 using a depth measuring device. This information is available in Table 11, where a negative number means the fastener head is below the aluminum surface, and a positive number means it is above. All fastener holes in this test piece do not have notches.

Table 11: Test Piece #2 HL-19-5-5 fastener head height relative to aluminum surface, for no notch sites.

Fastener #	Fastener Height (mm)	Fastener #	Fastener Height (mm)
9	0.29	6, 7, 29	0.01
1	0.255	17	-0.01
2, 5	0.23	19	-0.04
8	0.22	20, 27	-0.05
12	0.21	23	-0.13
3	0.20	28	-0.14
10, 11	0.17	18	-0.15
4	0.15	21	-0.19
13, 14, 22	0.05	25	-0.2
16	0.03	24	-0.21
15	0.02	26	-0.23

The experiment consisted of ten measurements on each of the twenty-nine fasteners in Test Piece #2. Figure 41 shows the plot of S1 versus fastener head height in millimeters, where it can be shown that as the fastener head rises above the aluminum surface, there is a slight decline in the size of the PCA score S1. Figure 42 shows the correlation of fastener head height relative to aluminum with PCA score S2. As the fastener head rises above the aluminum surface, the S2 score decreases. Figure 43 shows the plot of fastener head height relative to aluminum with the third PCA score. No correlation is observed with fastener head height and S3. The lack of correlation with fastener head

height and S3 is an important observation; recall Section 4.3, the presence of a notch is indicated on PCA score S3. Figure 44 and Figure 45 show similar relationships between fastener head height and S4 and S5, respectively, where it is observed that there is no effect of changing fastener head height on the amplitude of the fourth and fifth PCA scores.

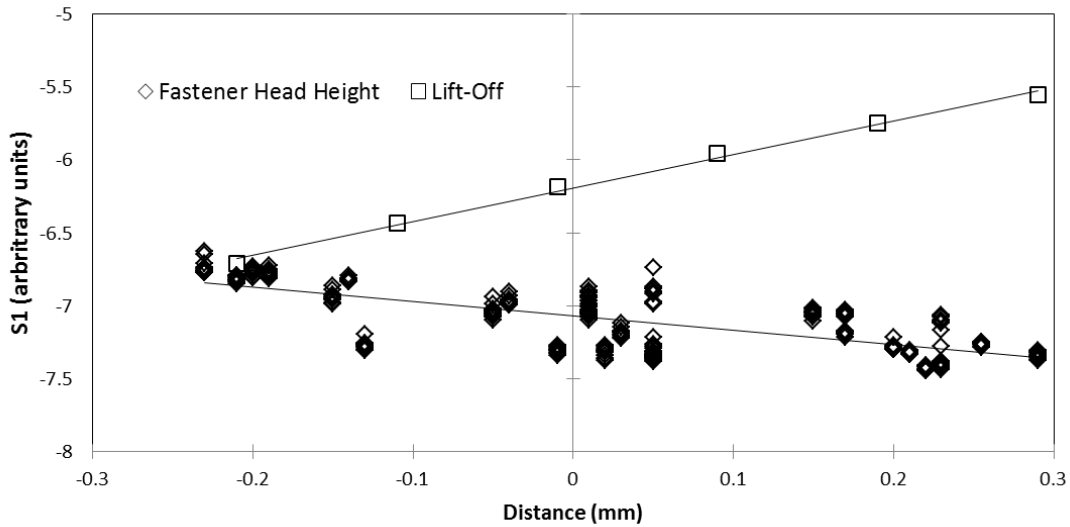


Figure 41: Effect of fastener head height distance and lift-off distance on first PCA score (S1).

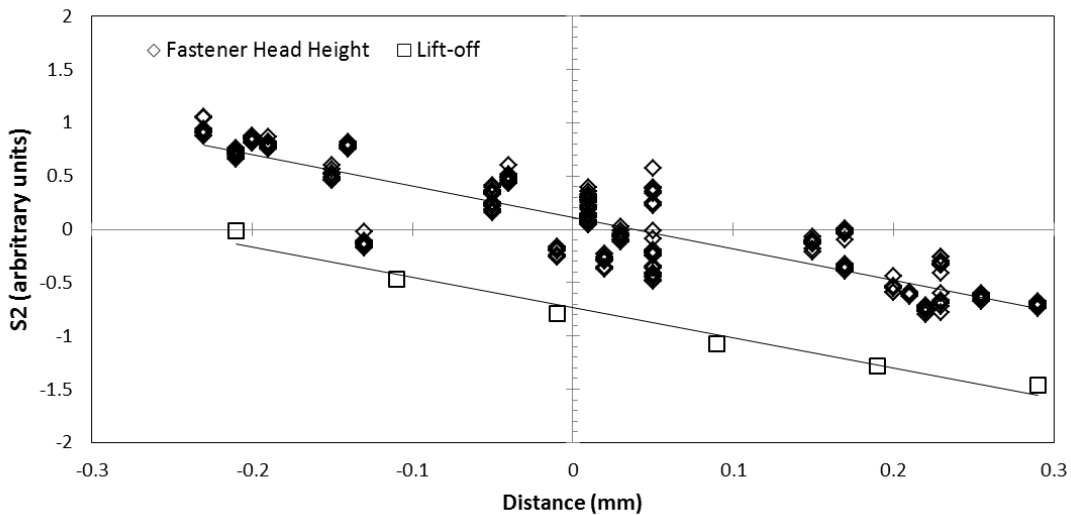


Figure 42: Effect of fastener head height distance and lift-off distance on second PCA score (S2).

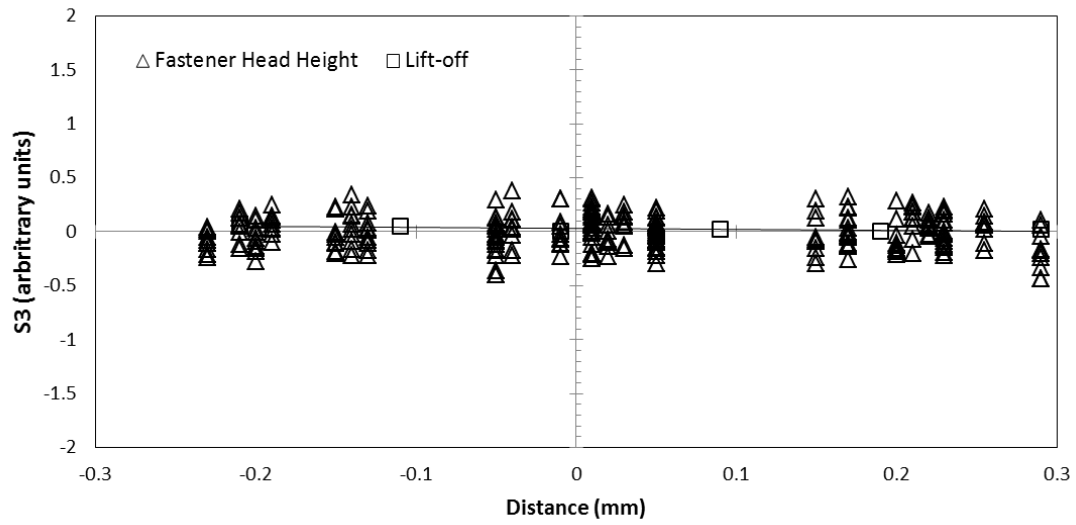


Figure 43: Effect of fastener head height distance and lift-off distance on the third PCA score (S3).

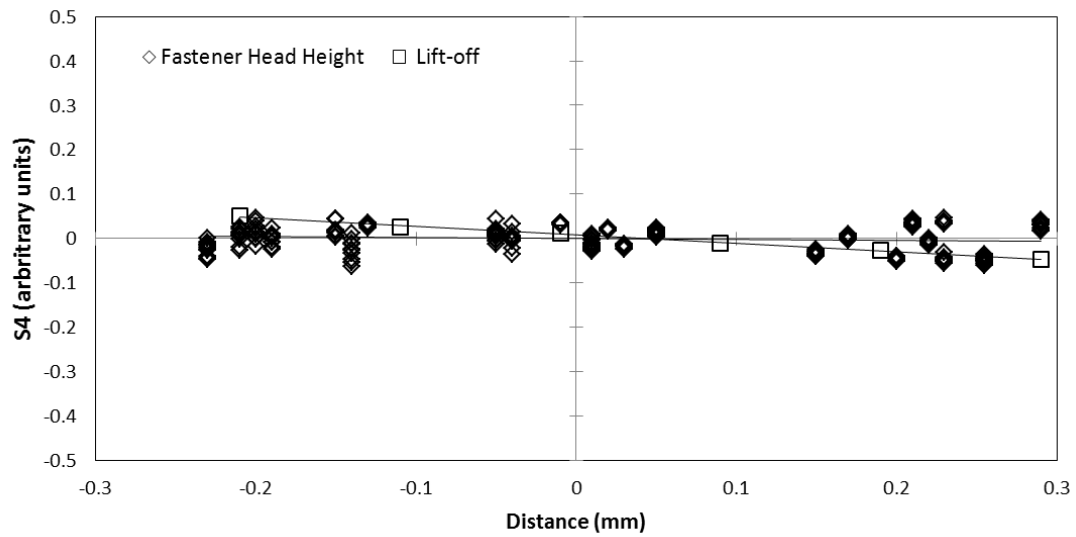


Figure 44: Effect of fastener head height distance and lift-off distance on the fourth PCA score (S4).

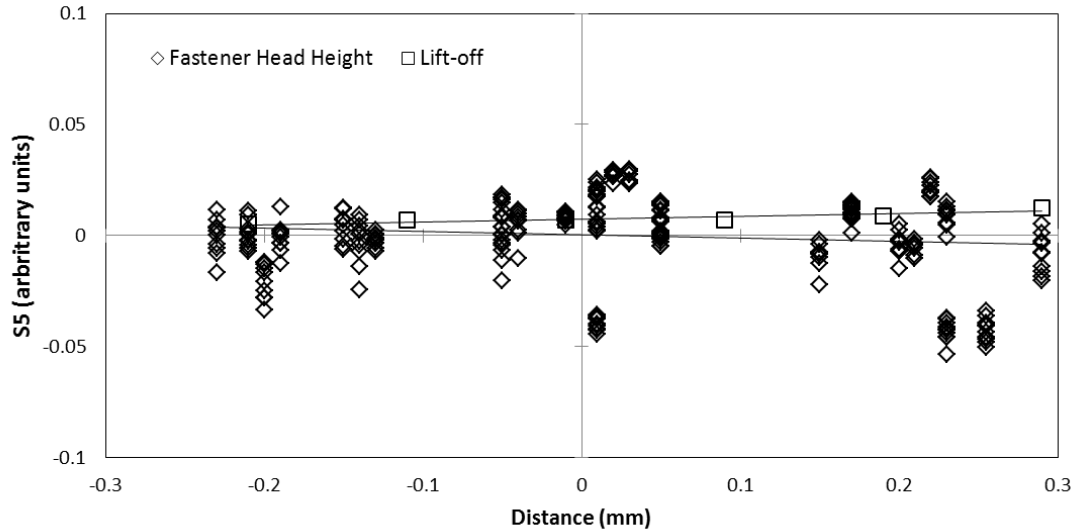


Figure 45: Effect of fastener head height distance and lift-off distance on the fifth PCA score (S5).

Following these experiments and subsequent data analysis, a new top piece for each of test piece #1 and #2 were fabricated with a more precise countersink operation, due to the large effect of fastener head height on PCA scores. This was completed to better simulate actual wing structures and reduce the effect due to varying fastener head height on measured results.

5.4.2 Lift-off Effects

Another variable assessed was probe lift-off above the fastener in the aluminum. Test piece #2 was used to conduct this experiment, where six measurements were taken on fasteners 24, 25 and 26, and their starting head heights were -0.2, -0.21 and -0.23, respectively. Starting at zero lift-off, a shim of thickness 0.10 mm was added under the probe so as to raise it above the aluminum. A total of five shims were added under the probe, raising it a total of 0.5 mm above the aluminum. The six points from the lift-off experimental results are plotted above in Figure 41. A linear trendline was fit through the data that shows a positive linear effect on the first PCA score as the probe is raised above the aluminum. Figure 42 above also shows the effect of lift-off on the second PCA score. A linear trendline that was fit through the data shows a positive linear trend on the second score with increasing lift-off. Figure 43 above shows the plot of the third PCA score with lift-off, where the trendline through the S3 data has a slope value of zero, so there is no correlation of lift-off with the third score as the probe is raised above the aluminum surface. Furthermore, Figure 44 above is a plot of the fourth PCA score with lift-off and there is a slight negative slope to the trend-line

through the lift-off data. Using linear regression, this slight slope is shown to be significant using 95% confidence, meaning that the fourth PCA score is correlated with lift-off. In addition, Figure 45 above, a plot of the fifth PCA score variation with lift-off, shows a slight positive slope to the trend-line through the lift-off data. Again, using linear regression and 95% confidence, the fifth PCA score is shown to be correlated with lift-off.

In conclusion, lift-off is observed to be significantly correlated with the first, second, fourth and fifth scores, but not the third. This preserves the third score for identification of notches, independent of lift-off and head height variations.

5.5 Effect Due to Edge

PEC signals are sensitive to geometrical discontinuities within the sample. In the case of the lap-joint, there is an edge on the top and bottom piece of each of the three multi-layer test pieces (NAVAIR, test piece #1 and Aurora Samples). Ideally, when no defect is present, each of the four coil pairs should produce no signal other than that due to differences in coil-pair balancing. However, the presence of the edge on the outer surface of the top plate (at 270°) and the outer surface of the bottom plate (at 90°) present geometrical differences, which can significantly affect signals. Figure 46 shows no-crack differential signals obtained from all four coil pairs. The first coil pair is aligned with 0° , where each coil is identically located with respect to the edge, and negligible effects on the signal are observed. The 45° and 135° coil pairs are ideally mirror images of one another, with one coil close to the gap for each pair, so they produce significant signals. They are not identical signals due to imbalance within the coil pairs. The 90° coil pair has one coil placed close to the edge with the other coil furthest from the edge. This coil pair produced the largest signal due to the proximity of one of the coils to the edge. A similar correlation was observed in FEM [32], where the third coil pair (aligned perpendicular to the edge) produced the largest signal.

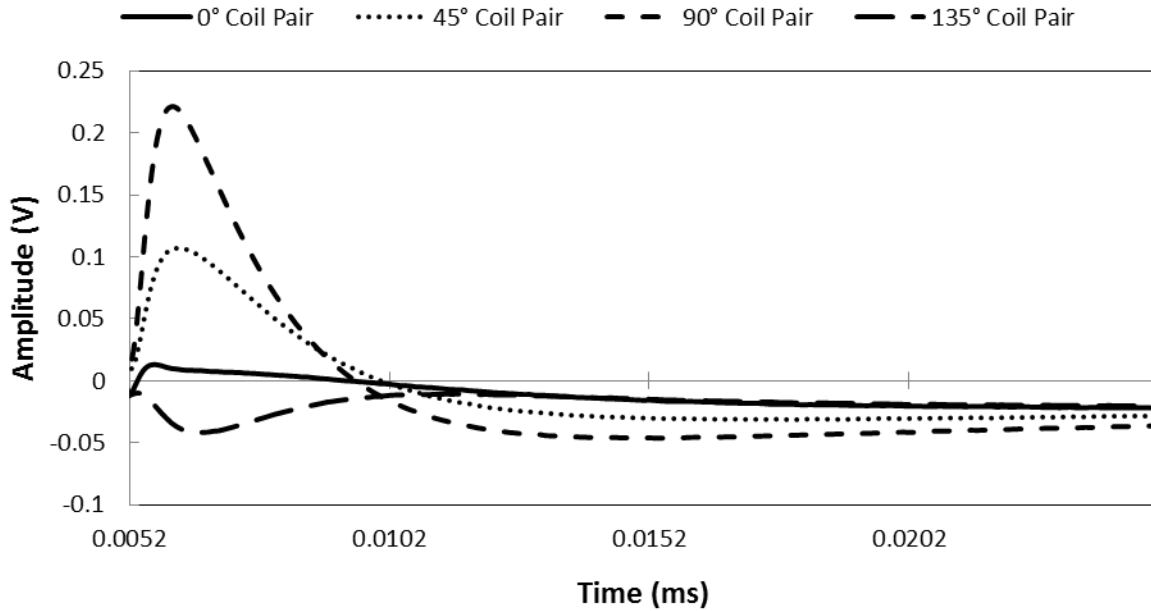


Figure 46: Experimental no-crack differential signals from all four coil pairs.

5.6 Effect Due to Fastener Distance from Edge

Section 5.5 showed how the coil pair signals are affected by the presence of the edge. This result suggests an investigation into the effect of fastener distance from the edge, should be performed. Some variability in fastener distance to the edge of the aluminum is observed on actual aircraft structures, possibly since these were manually located. The distance from the edge of the fastener to the edge of aluminum was measured on no-notch fasteners (1, 2, 3, 4, 30, 31, 32, and 33) on the CP-140-TT-1B Aurora sample, and these distances are presented in Table 12.

Table 12: Distance from edge of fastener to edge of aluminum.

Fastener #	Distance to Edge (mm)
30	6.21
33	6.34
2	6.44
31	6.50
32	6.68
1	6.72
3	6.99
4	7.05

PCA scores obtained from measurements taken on the Aurora sample were examined for each coil pair. For the 90° coil pair, which showed the biggest effect due to the edge as presented in Section 5.5, the first, second and third PCA scores showed negligible correlation with fastener distance to edge. The fourth and fifth scores were plotted with distance from the fastener edge to the edge of aluminum and are shown in Figure 47 and Figure 48, respectively. There is an observed correlation with fastener distance to the edge of aluminum and PCA scores S4 and S5. Since the presence of a notch is correlated most strongly with the third PCA score, and a weaker, but significant correlation is observed on the fourth and fifth scores, the effect due to the edge is expected to have only a minor effect on notch detection capability.

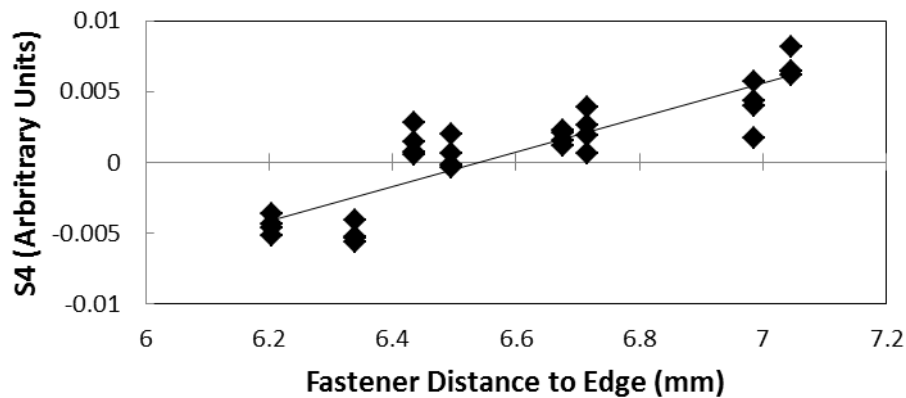


Figure 47: PCA score S4 plotted with fastener distance to edge in millimeters.

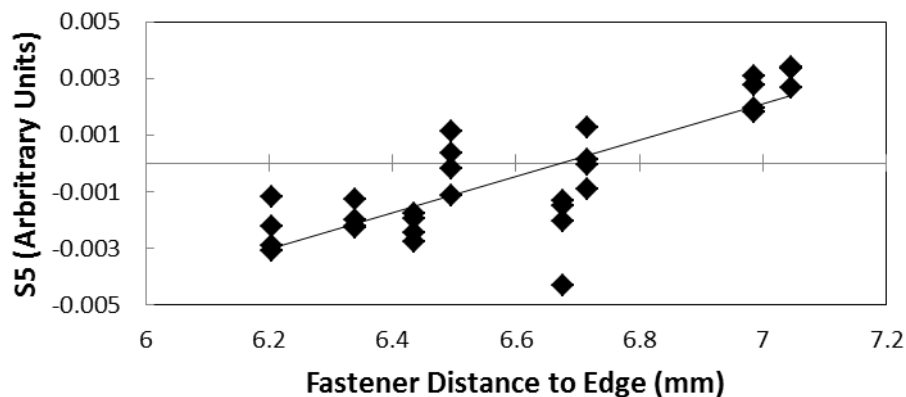


Figure 48: PCA score S5 plotted with fastener distance to edge in millimeters.

5.7 Effect of Temperature on Probe Performance

A separate group of tests was conducted on Test Piece #1 to assess the possible effect of temperature on probe functionality. Six fasteners, that do not contain notches at their bore, were tested in a temperature controlled chamber, where the probe and sample was conditioned to three temperature settings (9°, 20° and 30° Celsius). There was no observed effect on the first three PCA scores, and the results of these tests are presented in Annex C.

5.8 Results on NAVAIR Sample

5.8.1 Test Piece Summary

The NAVAIR sample contains EDM notches in the bore holes of 15 out of 23 fastener locations. The top layer thickness is 2 mm. The fasteners are of type HL-19 and have a head diameter of 7 mm. The notches range in length from 0.89 to 5.46 mm and are located in both the top-of-bottom layer and bottom-of-top layer.

5.8.2 Eigenvector Selection

The first five eigenvectors for the third coil pair, resulting from differential mode analysis on the NAVAIR sample, are shown in Figure 49. The first vector represents an average of all the data that went into the analysis, and the subsequent vectors account for the observed variation. As stated in Section 2, only the first few eigenvectors are required to accurately reproduce the original signal as represented by the residual sum of squares calculated between the original and reproduced data. In this thesis work, five eigenvectors are used to reproduce the original signal for three reasons. First, Figure 50 shows the results obtained from logistic regression [17] to the hit/miss data on second layer cracks obtained when the scores of 1-3, 1-4 and 1-5 eigenvectors are used to calculate the Mahalanobis distance. A 99% confidence level was used to calculate the Hotelling T^2 value. From this figure it can be seen that using four eigenvectors ($a_{50} = 1.55$ mm) rather than three ($a_{50} = 2.35$ mm) improved the detectability for smaller cracks, but offers little improvement at larger crack sizes. On the other hand, using five eigenvectors ($a_{50} = 0.90$ mm), the whole curve shifts significantly to the left. Therefore, using five eigenvectors rather than three or four, gives substantially better crack detection.

Second, FEM [32] suggested that the highest concentration of eddy currents occurs between 0.0004 - 0.001 seconds (see Figure 29). The fourth and fifth eigenvectors, shown in Figure 49, reach peak

amplitude in the same timeframe where eddy currents are the strongest in the second layer. The correlation of eigenvector peak amplitude with higher current density is consistent with the observation of improved detectability, as shown in Figure 50.

Finally, the signal-to-noise ratio of the eigenvectors severely degrades past the fifth vector, making it ineffective to reliably use more than five vectors for signal analysis.

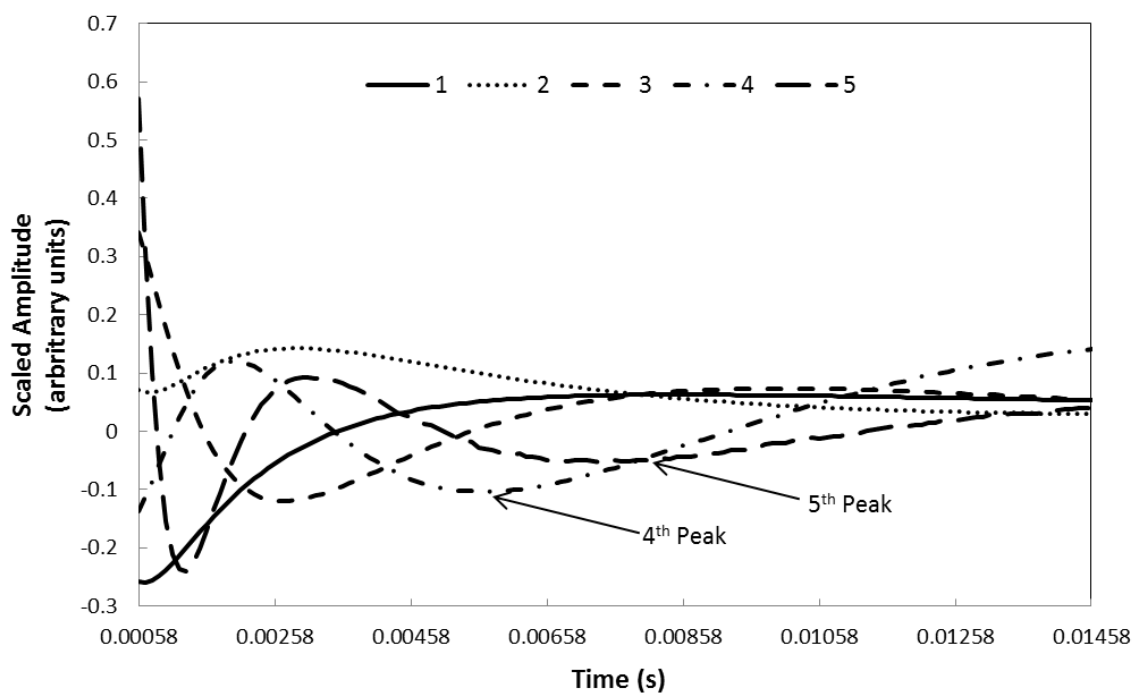


Figure 49: First five eigenvectors of PCA on data from NAVAIR third coil pair (differential mode).

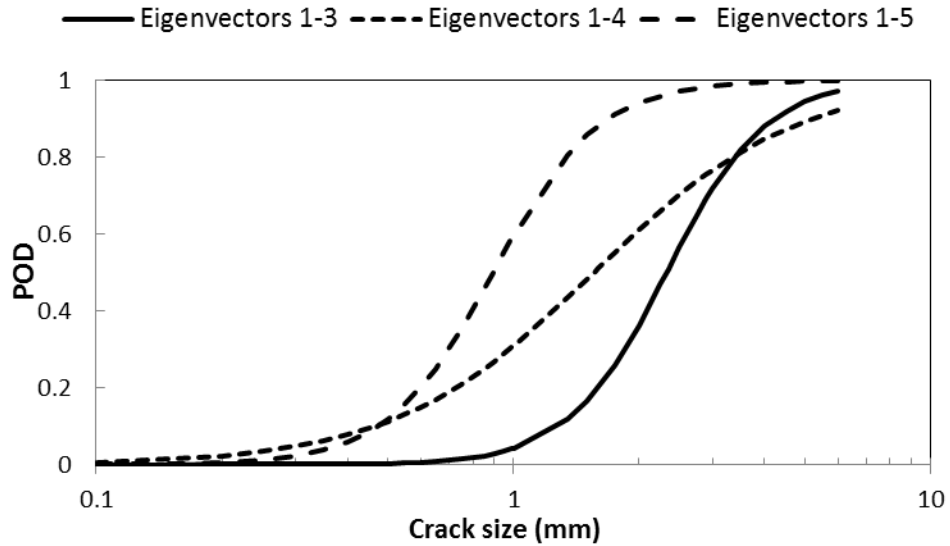


Figure 50: Results from logistic regression performed on hit miss data from NAVAIR sample using 1-3, 1-4 and 1-5 eigenvectors. Horizontal axis is on a log scale.

5.8.3 Absolute Mode Crack Detection Test Results

The experimental process described in Section 3.6.3 was performed on the NAVAIR sample using the probe in absolute mode. After data collection, the PCA process was applied to the signals. The first step is to gate the signal at the appropriate time where defect information is believed to be located. With coils in absolute mode, the eight coil pairs output eight individual signals. The signals corresponding to coil pairs 180° from one another are selected, concatenated and gated in the same time interval. PCA is conducted on each coil pair separately and once completed the scores are available to be examined.

The PCA scores from four fasteners with notches and four fasteners without notches are shown in Figure 51. The solid filled circles, squares and triangles are scores from fasteners with notches at their bore. The hollow circles are scores from fasteners with no notches at their bore. The group of scores in black circles are scores from the smallest notch (0.89 mm). There is overlap between this group and the group of blanks. This poses a problem for crack detection, as the notches can be disguised as blanks in PCA space, as stated previously in Section 2.9.3.

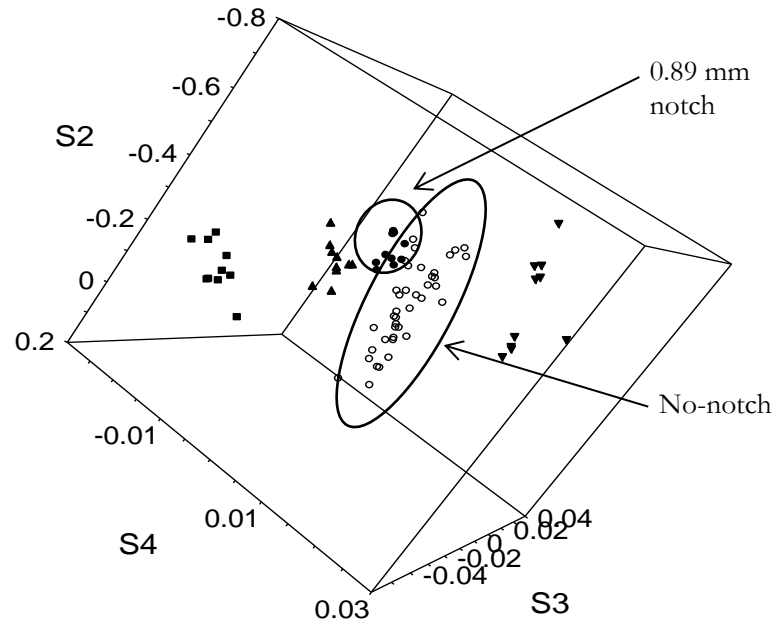


Figure 51: 3-D view of NAVAIR data PCA scores S2, 3 & 4.

In order to better distinguish between notches and blanks, the Mahalanobis Distance is calculated for each fastener. It is apparent from Figure 51 that PCA scores S2, S3 and S4 could be used to calculate the MD, as they appear to provide good separation for some fasteners with notches. However, five scores (S1-S5) are used to calculate the MD as some information is also located in S1 and S5 as discussed earlier in Section 5.8.2. Using scores S1-S5 increases crack detection and lowers false call rates. The MD is then compared to the threshold, calculated using equation 2.50. The threshold calculated for this experiment was 4.2 at 99% confidence and 3.5 for 95% confidence. There are no units associated with the MD, as it is a relative measure of distance from the centroid of the cluster of blanks, in terms of standard deviations. The MD was plotted for each fastener and the plot is shown in Figure 52, along with the decision thresholds, while results of this test are shown in Table 13. It is worth noting that the MD associated with fasteners 5 and 14 corresponds to the biggest second layer notches, at 5.46 mm and 5.08 mm, respectively. As the notches decrease in size, so does the MD as indicated by MD values for fasteners 4 and 11. This indicates that there is a correlation of MD with notch size, which will be investigated further in Section 5.8.5.

Table 13: NAVAIR Sample crack detection results in absolute mode.

Confidence (%)	Crack Detection (%)	False Call Rate (%)
99	75	4
95	85	9

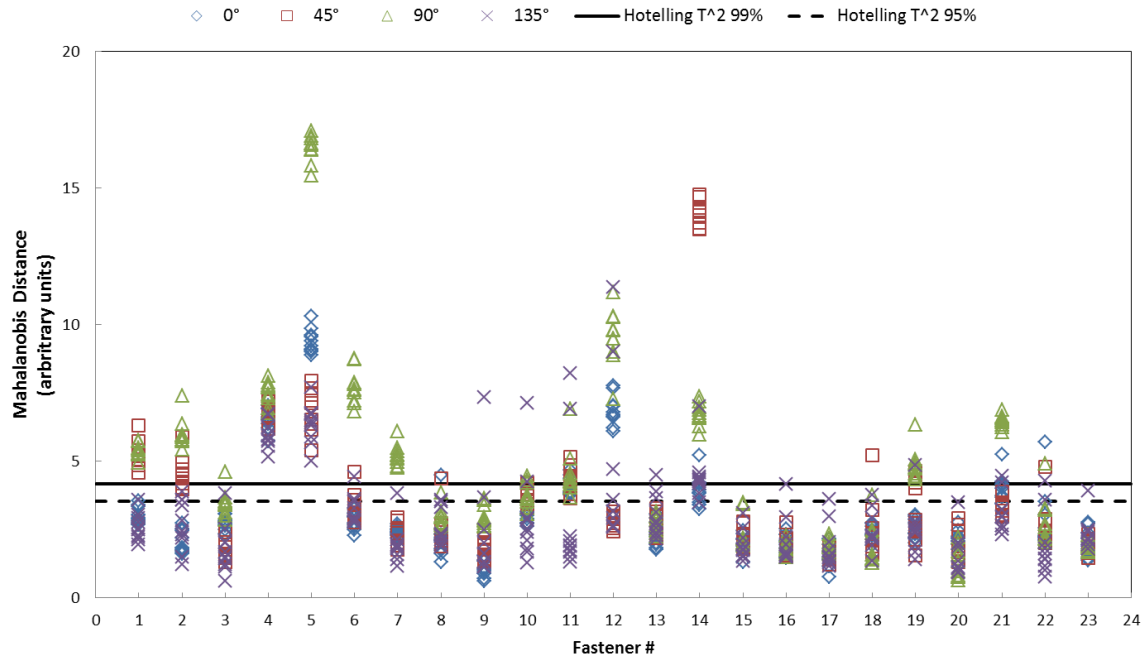


Figure 52: NAVAIR Sample Mahalanobis Distance versus fastener # in absolute mode.

Considering the 99% confidence results, approximately 25% of the cracks were missed with a false call rate of 4%. Cracks located at fasteners 3, 9, 10, and 13, which correspond to sizes 1.78 mm, 1.52 mm, 2.79 mm, and 1.52 mm, respectively, were missed. When considering the 95% confidence interval results, 15% of the cracks were not detected with a false call rate of 9%. Cracks located at fasteners 3, 9 and 13, which correspond to sizes 1.78 mm, 1.52 mm, and 1.52 mm, respectively, were missed.

5.8.4 Differential Mode Crack Detection Test Results

The experimental process described in Section 3.6.3 was also performed on the NAVAIR sample using the probe in differential mode. In differential mode there are four output channels

corresponding to four coil pairs. The signals are gated and then PCA is performed on the signal pair from each channel individually. Once the PCA scores are output, they are used to calculate the MD for each fastener. The MD is calculated using scores S1-S5, and the distances are plotted against the fastener number in Figure 53. The crack detection results are displayed in Table 14. The threshold calculated for this experiment was 4.2 at 99% confidence and 3.5 for 95% confidence.

Table 14: NAVAIR Sample crack detection results in differential mode.

Confidence (%)	Crack Detection (%)	False Call Rate (%)
99	97	4
95	100	10

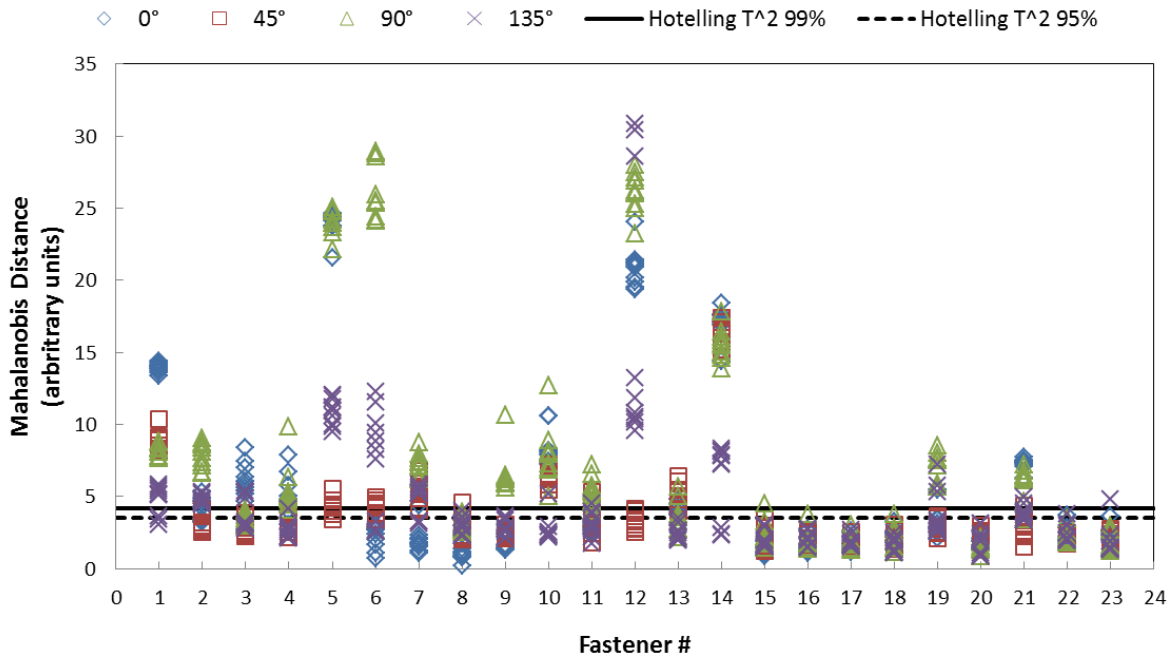


Figure 53: NAVAIR Sample Mahalanobis Distance versus fastener # in differential mode.

Considering the 99% confidence results, approximately 3% of the cracks were missed, with false call rate of 4%. Out of ten measurements taken per fastener, cracks located at fasteners 4, 11 and 13, which correspond to sizes 0.89 mm, 0.89 mm and 1.52 mm, respectively, were only missed once or twice out of those ten measurements. When considering the 95% confidence results, no cracks were missed as a crack detection rate of 100% was achieved, but with a false call rate of 10%.

5.8.5 Mahalanobis Distance versus Crack Size

As stated in Section 5.8.3, the MD values appear to be correlated with notch size. Referring to Figure 53, fasteners with the largest crack size, greater than 5.08 mm (fasteners 5, 12 and 14), tend to produce the largest distance values. In addition, fasteners with the smallest crack size of 0.89 mm (fasteners 4 and 11) tend to have smaller distance sizes. To investigate this, the largest Mahalanobis Distance was plotted with crack size (mm) for each of the 100 measurements (ten measurements on each of ten second layer cracks) and the results are displayed in Figure 54. A line of best fit was inserted through the data, showing that the relationship between the distance and crack size is approximately linear with the R^2 value equal to 0.89. Both threshold values (4.2 at 99% confidence and 3.5 for 95% confidence) are depicted on the graph. It is noted that all the cracks fall above the 95% threshold value. This important observation shows the potential for crack sizing using Mahalanobis Distance.

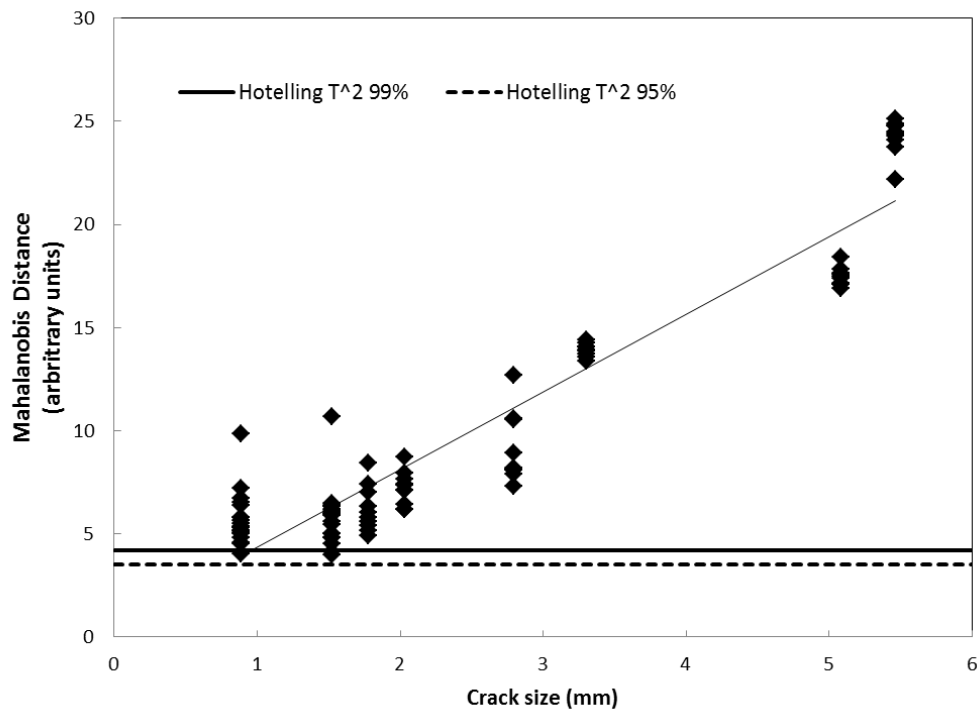


Figure 54: Mahalanobis Distance versus crack size for NAVAIR Sample second layer cracks in differential mode.

5.9 Results on Test Piece #1

5.9.1 Test Piece Summary

Test Piece #1 was fabricated in the lab using 2024-T3 aluminum sheets joined together by a row of fasteners. The top sheet thickness was 2 mm and the fastener head diameter was 6.5 mm. The piece contains twenty-nine fasteners of type HL-19. Ten of the fastener holes do not have notches at their bore. The notches in the remaining 19 fastener holes are in the top-of-bottom layer, and range in length from 0.83 – 3.26 mm, with minimum notch size slightly less than the minimum 0.89 mm in the NAVAIR sample.

5.9.2 Eigenvector Selection

Test piece #1 data, using absolute mode analysis, was analyzed with the same number of eigenvectors that were used to calculate crack detection results on the NAVAIR sample (vectors 1-5). In order to ensure maximum crack detection results, alternate combinations of scores were investigated. It was determined on this test piece, in absolute mode, that using eigenvectors three, four and five to calculate the MD instead of eigenvectors 1-5 yielded better crack detection. Figure 55 shows the first five eigenvectors of absolute mode PCA data on Test Piece #1 from the third coil pair. The third and fourth eigenvectors have the biggest contribution in the desired timeframe where eddy current density is greatest (0.4 - 1.0 ms, see Section 3.8.1).

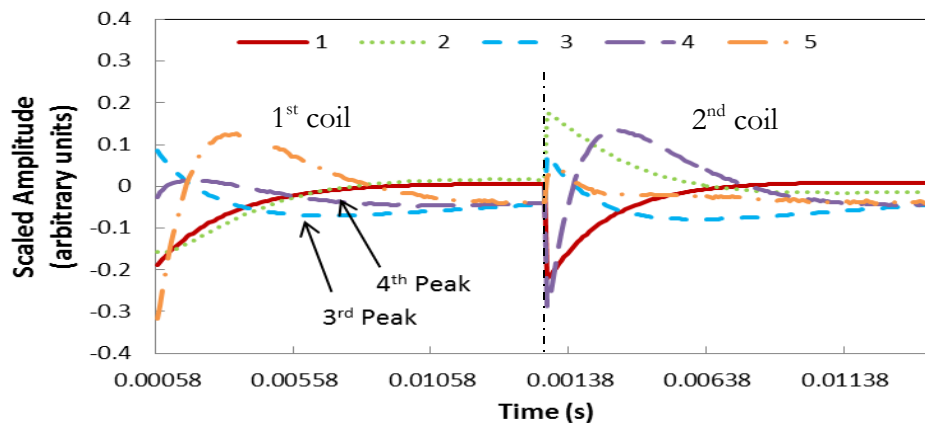


Figure 55: First five eigenvectors of PCA on data from Test Piece #1 third coil pair (concatenated signals) in absolute mode.

This is in contrast to the NAVAIR sample shown in Figure 49, where the fourth and fifth vectors peaked in the desired timeframe. Figure 56 shows the results obtained from logistic regression [17] to the hit/miss data on second layer cracks obtained when scores 3-5 are used to calculate the MD. In addition, in Figure 56, scores from 1-5 eigenvectors are used to calculate the MD. A 95% confidence level was used to calculate the Hotelling T^2 value for the hit/miss analysis. From this figure it can be seen that using a combination of the third, fourth and fifth scores ($a_{50} = 1.04$ mm) rather than five ($a_{50} = 1.45$ mm) improved the detectability of the majority of crack sizes by shifting the whole curve to the left. This is counter-intuitive, as one would assume that more terms would provide better results. However, if scores without information are added to the MD calculation, the Hotelling T^2 value increases faster than the increase in MD.

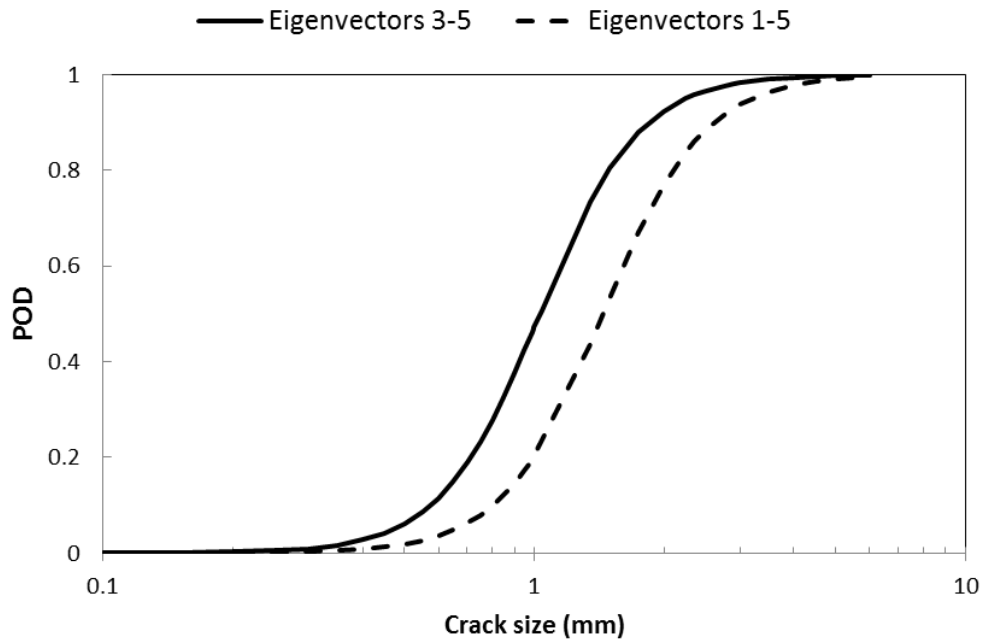


Figure 56: Results from logistic regression performed on hit miss data from Test Piece #1 using eigenvectors 3-5 and 1-5. Horizontal axis is on a log scale.

5.9.3 Absolute Mode Crack Detection Results

The experimental process described in Section 3.6.3 was performed on Test Piece #1 using the probe in absolute mode. After signal gating and PCA, the scores S3-S5 were then used to calculate the MD for each fastener, as stated in Section 5.9.2. The MD is plotted against fastener number and is displayed in Figure 57, while the crack detection results are shown in Table 15. The threshold

calculated for this experiment was 4.6 at 99% confidence and 3.5 for 95% confidence. As discussed in Section 5.8.4, the larger crack sizes, greater than 2.8 mm (fasteners 14 and 15), tend to produce larger MD values. This will be investigated in the next section.

Table 15: Test piece #1 crack detection results in absolute mode.

Confidence (%)	Crack Detection (%)	False Call Rate (%)
99	53	0
95	82	0

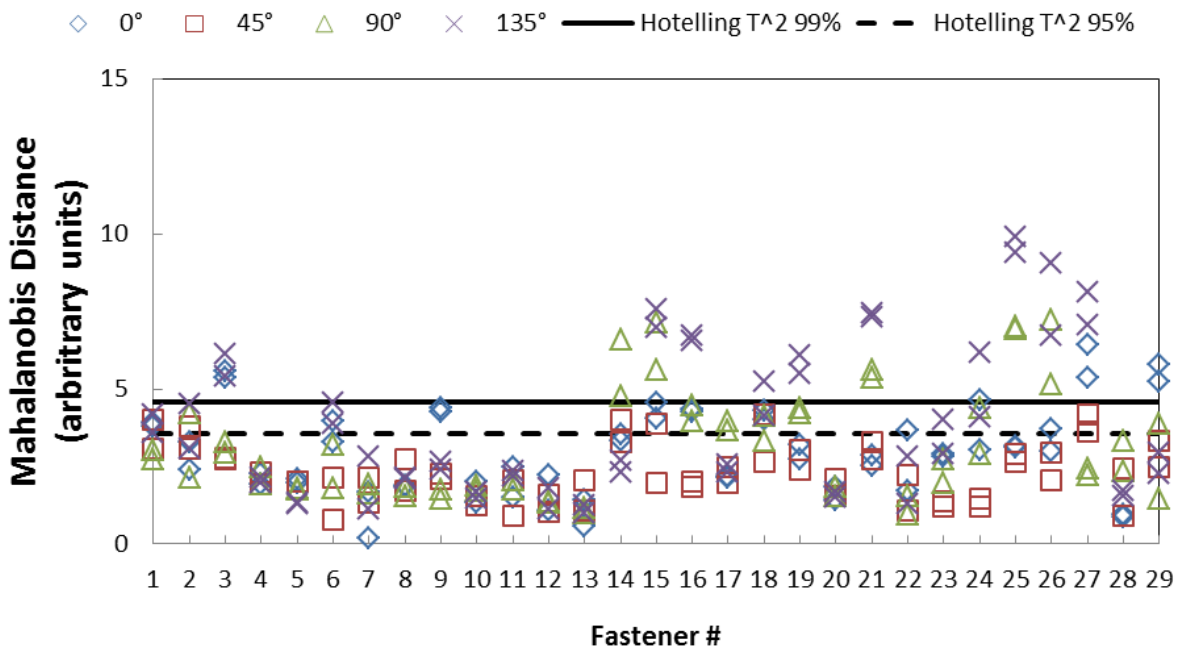


Figure 57: Test Piece#1 Mahalanobis Distance versus fastener # in absolute mode.

Considering the 99% confidence results, approximately 47% of the cracks were missed. Out of the two measurements taken per fastener, cracks located at fasteners 23 and 28, which were 0.94 mm and 0.83 mm, respectively, were missed two out of two times. Three cracks located at fasteners 8, 9 and 22 corresponding to sizes 1.47 mm, 1.43 mm, and 1.24 mm, respectively, were also not detected. In addition, cracks located at fasteners 2, 6 and 17, which were 1.97 mm, 1.94 mm and 1.92 mm, respectively, were completely missed. When considering the 95% confidence results, cracks located at fasteners 8, 22 and 28 were not detected. The larger number of misses is attributed to using the

probe in absolute mode. Differential mode, which will be investigated next, was more successful than absolute mode, as on the NAVAIR sample (see Section 5.8.4).

5.9.4 Differential Mode Crack Detection Results

The experimental process described in Section 3.6.3 was performed on Test Piece #1 using the probe in differential mode. After signal gating and PCA, the scores were used to calculate the MD for each fastener using scores S1-S5. The MD is plotted against fastener number and is displayed in Figure 58. The crack detection results are shown in Table 16. The threshold calculated for this experiment was 6.2 at 99% confidence and 4.8 for 95% confidence.

Table 16: Test Piece #1 crack detection results in differential mode.

Confidence (%)	Crack Detection (%)	False Call Rate (%)
99	82	0
95	92	0

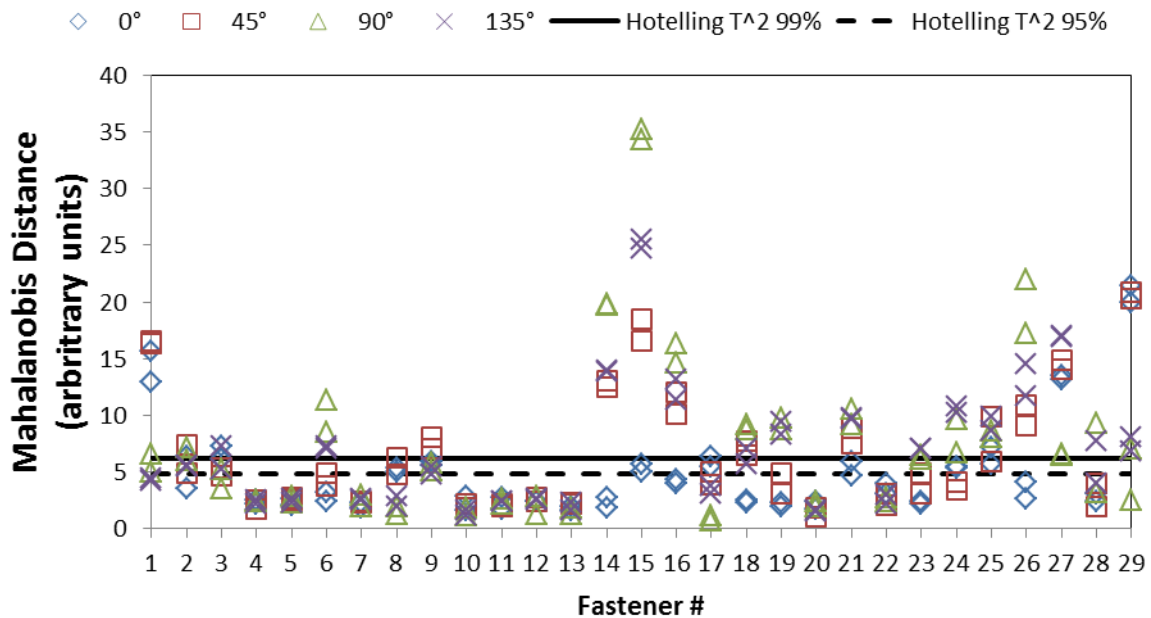


Figure 58: Test Piece#1 Mahalanobis Distance versus fastener # in differential mode.

Considering the 99% confidence results, approximately 18% of the cracks were missed with no false calls. Out of two measurements taken per fastener, a crack located at fasteners 22, 1.24 mm in

length, was not detected. Cracks located at fasteners 28, 3, 8, 17, and 2 corresponding to sizes 0.83 mm, 1.17 mm, 1.46 mm, 1.92 mm, and 1.97 mm, respectively, were missed once out of two measurements. When considering the 95% confidence results, a crack located at fastener 22 was missed twice out of two measurements and a crack at fastener 28 was missed once out of two measurements. No false calls were made in this case either.

5.9.5 Mahalanobis Distance versus Crack Size

As stated in Section 5.8.3 and Section 5.8.4, the MD values appear to be correlated with notch size. Referring to Figure 58, fasteners with the largest crack size, greater than 2.8 mm (fasteners 14 and 15), tend to produce the largest distance values. In addition, fasteners with the smallest crack size of 0.83 mm (fasteners 18 and 28) tend to have smaller distance sizes. The largest Mahalanobis Distance was plotted with crack size for each of the 190 measurements (ten each on 19 second layer cracks) and the results are displayed in Figure 59. A line of best fit was inserted through the data, once again showing that the relationship between the distance and crack size is approximately linear (R^2 value equals 0.6). Both threshold values (6.2 at 99% confidence and 4.8 for 95% confidence) are depicted on the graph. It is noted that all the cracks greater than 1.23 mm fall above the 95% threshold value.

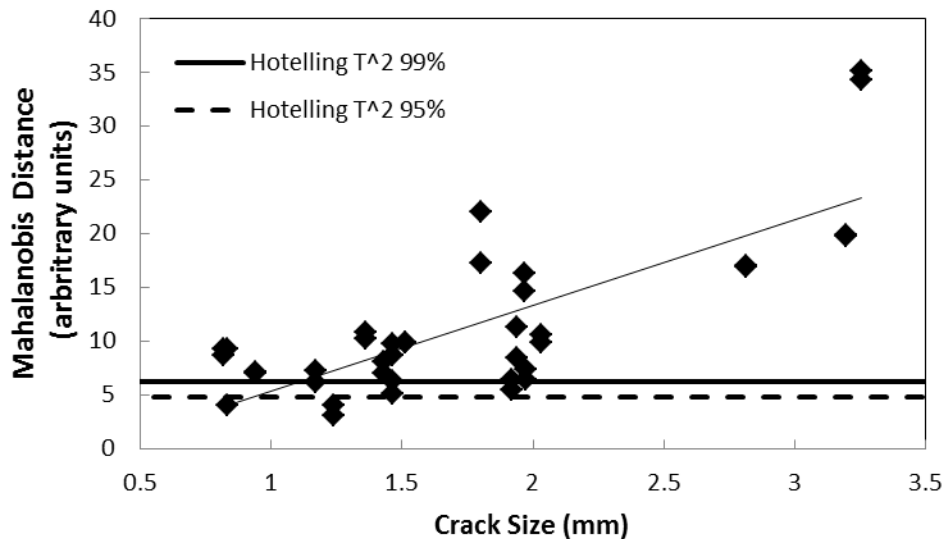


Figure 59: Mahalanobis Distance versus crack size for Test Piece #1 in differential mode.

5.10 Results on Test Piece CP-140-TT-1B

5.10.1 Test Piece Summary

This test piece, which was provided by ATESS, Trenton, contains 33 fasteners, with notches in 21 of the fastener bore holes located in the bottom-of-top layer and top-of-bottom layer. The notches range in length from 1.53 – 3.81 mm. The top layer thickness is 2.58 mm, the fastener head diameter is 7 mm and the fasteners are of type HL-51 (not the same as the NAVAIR sample and Test Piece #1).

5.10.2 Differential Mode Crack Detection Results

The experimental process described in Section 3.6.3 was performed on the Aurora Test Piece (CP-140-TT-1B) using the probe in differential mode. Only differential mode is considered here because previous samples indicated that differential analysis generated better results than absolute mode. After signal gating and PCA, the scores were used to calculate the MD for each fastener using scores S1-S5. The MD is plotted against fastener number and is displayed in Figure 60, while the crack detection results are shown in Table 17. The threshold calculated for this experiment was 4.4 at 99% confidence and 3.7 for 95% confidence.

Table 17: Test piece CP-140-TT-1B crack detection results in differential mode.

Confidence (%)	Crack Detection (%)	False Call Rate (%)
99	86	13
95	90	21

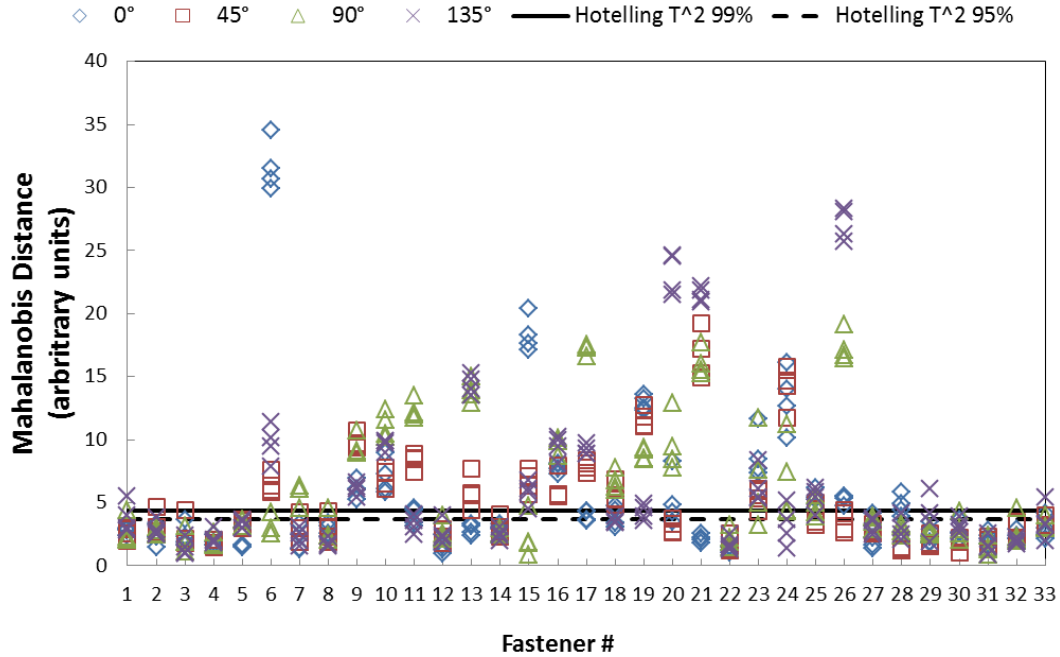


Figure 60: CP-140-TT-1B Mahalanobis Distance versus fastener # in differential mode.

Considering the 99% confidence results, approximately 14% of the cracks were missed. Out of four measurements taken per fastener, three second layer cracks located at fasteners 5, 27 and 29 corresponding to lengths of 2.54 mm, 1.52 mm and 2.03 mm were not detected. When considering the 95% confidence results, a notch located at fastener 27 (1.52 mm length) was missed twice out of four measurements and a notch at fastener 29 (2.03 mm length) was missed twice out of four measurements. The false call rate did increase from 13% to 21%, which is a high rate that is dependent on the threshold used (Hotelling T^2 value).

For these results, the threshold was calculated using $n=48$ (refer to equation 2.50), the number of blank fasteners (12) times the number of measurements (4). This is the same calculation used for previous threshold values. If we decrease the value for 'n' for these results to 12 (number of blanks alone), the threshold values for 99% and 95% confidence are 7.9 and 5.8, respectively. Subsequently, raising the threshold value lowers the crack detection rates to 64% and 80%, respectively, for 99% and 95% confidence and the false call rates decrease to zero for both confidence intervals.

5.10.3 Mahalanobis Distance versus Crack Size Results

As stated in Section 5.8.3 and Section 5.8.4, the MD values are observed to be correlated with notch size. As shown in Figure 60, fasteners with the largest first layer crack size, greater than 3.2 mm (fasteners 6 and 26), tend to produce the largest MD values. In addition, fasteners with the smallest first layer cracks, smaller than 1.3 mm (fasteners 7, 13 and 28), tend to produce smaller distance values. Also shown in Figure 60, fasteners with the largest second layer crack size, greater than 3.7 mm (fasteners 10 and 16), tend to produce the largest distance values (for second layer only cracks). In addition, the fastener with the smallest second layer crack, smaller than 1.6 mm (fastener 27), tend to produce smaller distance values.

The largest Mahalanobis Distance was plotted with crack size (in millimetres) for four first layer and four second layer notches and the results are displayed in Figure 61. A line of best fit was inserted through the data, once again showing that the relationship between MD and crack size is approximately linear (R^2 values equal 0.57 and 0.75 for the first layer best fit line and second layer best fit line, respectively). Both threshold values (5.1 at 99% confidence and 4.2 for 95% confidence) are depicted on the graph. First, it is noted that all the first layer cracks fall above the 99% line, and second layer cracks, greater than 2.5 mm, fall above the 95% threshold value. Second, the first layer cracks tend to produce a greater distance value for the same crack size, i.e. a 3.8 mm crack in the first layer produces a distance value on average of 27.1, while a 3.8 mm crack in the second layer produces a distance value on average of 11.2. This means that there is a possibility of not only sizing cracks in either the first or second layer, but potentially being able to determine in which layer the crack resides. Difficulty may arise when a fastener contains both and top and bottom layer cracks at its bore because it is difficult to discern which crack contributes to the value output of the Mahalanobis Distance calculation.

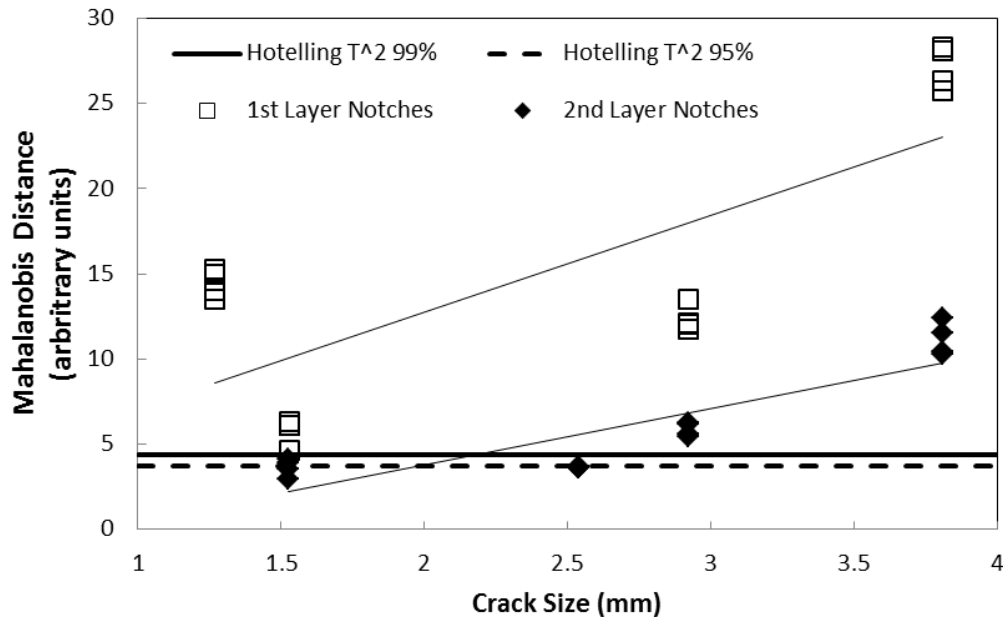


Figure 61: Mahalanobis Distance versus crack size for test piece CP-140-TT-1B in differential mode.

5.11 Comparison of Test Piece Results (Differential Analysis)

Section 5.10.3 discussed how false call rates and crack detection results can vary by changing the threshold value. In order to compare the results of each test piece, a comparison of no false calls, 5% and 10% false call rates and crack detection results are shown in Table 18. There is no confidence interval associated with these results, as an arbitrary threshold value was sought to give 5% false call rates. An 87% crack detection rate was achieved on the NAVAIR sample with no false calls, a 100% crack detection with no false calls on Test Piece #1 and an 80% crack detection with no false calls was obtained for the CP-140-TT-1B Aurora sample.

A 100% crack detection accompanied by a 5% false call rate could be achieved for the NAVAIR sample and Test Piece #1. However, only 82% crack detection on the CP-140-TT-1B Aurora test piece could be achieved when the false call rate was lowered to 5%. In addition, all second layer cracks were missed when the false call rate was lowered to 5%. Should a 10% false call rate be tolerated, the Aurora sample crack detection rate only increases to 85%. If a 100% crack detection rate was desired on the Aurora sample, it would be accompanied by a 65% false call rate. This

analysis shows the importance of threshold values, and how to distinguish acceptable false call rates. A discussion on the implication of false calls is included in the following section.

Table 18: Crack detection results for no false calls, 5% and 10% false call rate.

False Call Rate (%)	Crack Detection Results (%)		
	NAVAIR	Test Piece #1	CP-140-TT-1B
0	87	100	80
5	100	100	82
10	100	100	85

6 Discussion

6.1 PCA and Crack Orientation

One of the benefits of viewing PCA scores in three dimensions is that repetitive measurements tend to cluster together, demonstrating the repeatability of the technique. A second benefit is that scores obtained when a crack is present at the borehole cluster separately from scores obtained without a crack. This allows calculation of the distance between clusters, and detection of cracks as outlined in Section 5. Viewing the PCA scores before calculation of MD can yield additional crack information. Figure 62 shows a three dimensional PCA space of principal component scores S2, S3 and S4 obtained from the NAVAIR sample in differential mode. Fasteners 8, 17, 20 and 22 are fasteners without notches at their bore, and each graph contains two groups of scores from two separate fasteners with notches at their bore, but the notch locations are 180° from each other. In Figure 62 (a), fastener 5 has a notch at orientation C (reference Figure 62 (c) for notch orientations), while fastener 3 has a notch at D (180° from C), and the scores separate in the PCA space to either side of the cluster of blanks. The same effect occurs in Figure 62 (b), where fastener 1 has a notch at orientation A, and fastener 14 has a notch at orientation F, 180° from A. The scores from these two fasteners lie on either side of the cluster of blanks. In addition, notch orientations A and C are both on the side closest to the edge of aluminum (see Figure 62 (c), where the second layer aluminum edge is located at 90°) and both sets of scores in the PCA space tend to congregate on the same side relative to the cluster of scores from the no-notch fasteners. The same results occur for notch orientations D and F. Figure 62 (d) shows fastener 4, which has a notch at orientation B, and fastener 13, which has a notch at orientation E. These scores separate from one another, but are not located on either side of the cluster of blanks, as in the other two graphs. This is partly due to edge effects, where the notch at fastener 4 is pointing in the direction of the edge of aluminum in the bottom layer.

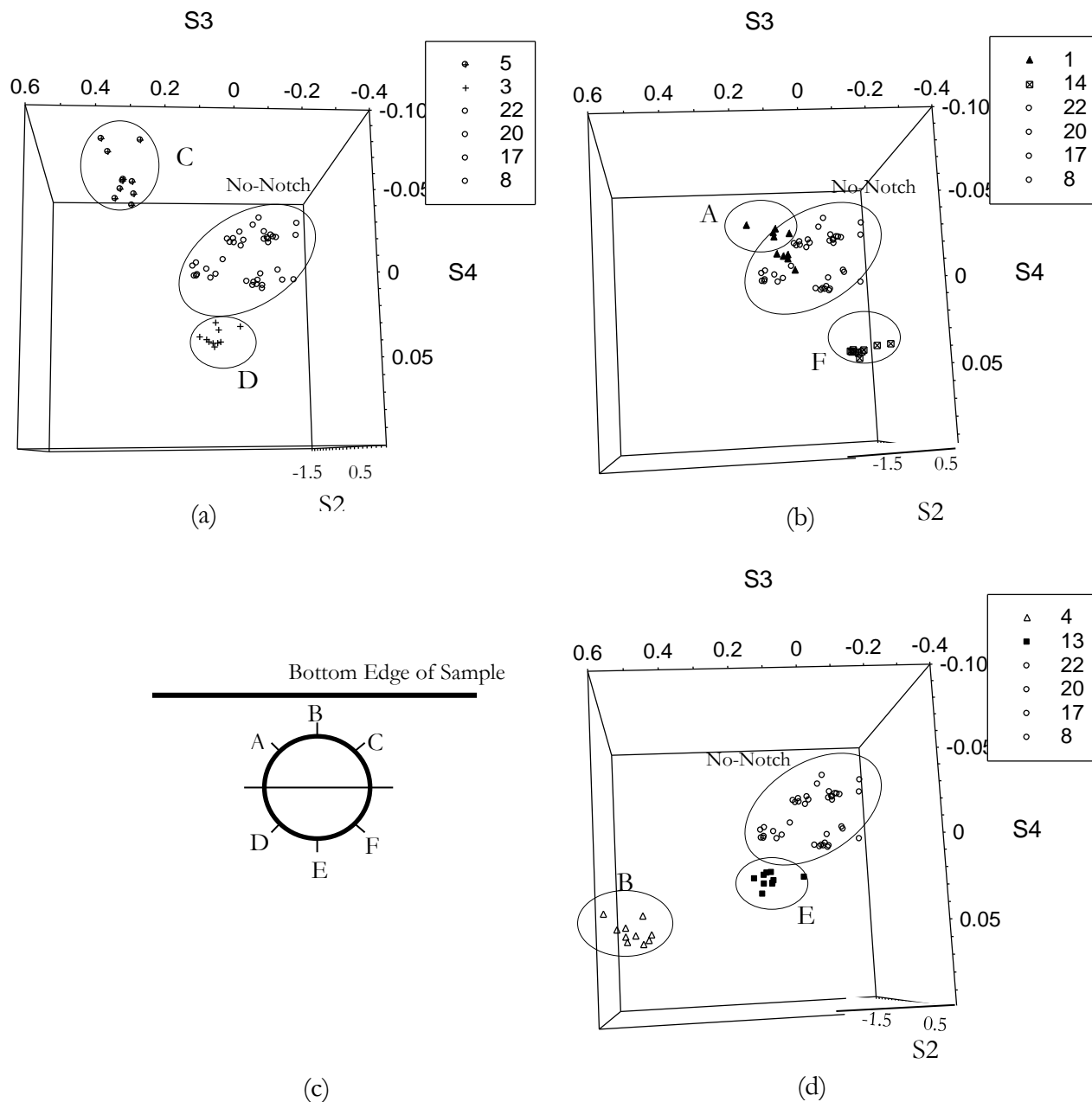


Figure 62: Three dimensional depiction of PCA scores S2, S3 and S4 from NAVAIR differential data. Labels refer to notch orientation as defined in the inserted figure.

6.2 Absolute versus Differential Analysis

Absolute and differential analysis methods were tested on two of the multi-layer test pieces (NAVAIR and Test Piece #1). Differential mode was chosen to analyze the Aurora sample because it yielded better crack detection results on the two previous test pieces. In addition, differential analysis was more robust and consistent than absolute, as absolute analysis required a different

combination of scores for the MD calculation, whereas differential analysis utilized scores 1-5 for each test piece.

6.3 Comparison to FEM

Considering the FEM [32] discussed earlier in Section 1.3.4, displacement effects were detected on the first PCA score. Similar experiments conducted on the single fastener test piece and NAVAIR sample showed that the effect of displacing the probe over the fastener was large on the first score, but also had a very minor effect on the second, third and fifth scores. The FEM showed that the first and third scores provided clear identification of notches, despite large effects due to displacement of the probe [32]. Results presented in this work showed the presence of a crack was most strongly correlated with the third score, with weaker correlation with remaining scores (1, 2, 4 and 5). The FEM results did not require more than three PCA eigenvectors to reproduce signals. However, FEM did not investigate additional factors such as: lift-off, fastener head height and distance of fastener from the edge, nor did it simulate coil imbalance effects. Due to the logistic regression results, presented in Section 5.8.2, showing that five eigenvectors produced better crack detection results than three (three were used in the FEM), this thesis work shows that PCA can extract additional information contained in the measured PEC signals. The FEM simulations demonstrated that PEC has the potential to successfully detect cracks, their depths and orientation in a dual layered aluminum structure. In addition, there was good agreement between the modeling, and the experimental results presented in Sections 4 and 5, as the FEM demonstrated the same sensitivity to notch orientation.

6.4 PCA Score Correlations with Variables

The results presented in Section 5 showed how different variables are correlated with PCA scores. A summary of these correlations is presented in Table 19, for the multiple fastener test piece results in differential mode. Fastener head height was an important variable to account for in the laboratory setting, but was effectively eliminated by re-countersinking the top pieces of Test Pieces #1 and 2. It is important to note that the correlation with the presence of a notch is not separate from other variables, such as off-centering, lift-off and distance to the edge. This is due to the large number of variables affecting the transient coil response and is consistent with the requirement of using five eigenvectors (and their representative scores) to calculate the MD for crack detection.

Table 19: Summary of PCA correlations with different variables.

PCA Score	Off-Centering (NAVAIR Sample)	Notch (NAVAIR Sample)	Fastener Head Height (Test Piece #2)	Lift-Off (Test Piece #2)	Distance to Edge (CP-140-TT-1B)
S1	Yes	Yes	Yes	Yes	No
S2	Yes (Weak)	Yes	Yes	Yes	No
S3	Yes (Weak)	Yes	No	No	No
S4	No	Yes (Weak)	No	Yes (Weak)	Yes
S5	Yes (Weak)	Yes (Weak)	No	Yes (Weak)	Yes

6.5 Minimum Detectable Flaw Size

6.5.1 General

The differential mode results from the NAVAIR sample, where the smallest notch size was 0.89 mm, showed that 100% of the notches (top and bottom layer) were detected, at 95% confidence. On test piece #1, the smallest notch size was 0.82 mm (fastener 18), where the overall notch detection result was 92% (one crack of size 0.83 mm was missed) for the differential analysis at 95% confidence.

The CP-140 test piece results were not as favourable as the results on the NAVAIR sample and the lab fabricated test piece. Ninety percent of the EDM notches were detected at 95% confidence, where two second layer notches, 1.52 mm and 2.03 mm, were missed. One of the reasons why fewer second layer cracks were detected in the Aurora test piece is that the first layer aluminum was of thickness 2.58 mm, thicker by 0.55 mm than the NAVAIR sample and test piece #1. Detection would be hampered by the requisite penetration depth as described in Equation 2.28, resulting in poorer crack detection results. In addition, the fasteners were a different type in the Aurora sample (HL-51) than the fasteners in the NAVAIR sample and test piece #1 (HL-19). A variation in fastener type will correspond to different material and alloying, and subsequently diverse values of permeability and conductivity (using conventional eddy current, it was determined that the different

fasteners do demonstrate a lower permeability). A change in fastener permeability will affect magnetization of the fastener, and subsequently the magnitude of the induced eddy currents [25].

NAVAIR and Test Piece #1 are very comparable at 5% false call rate, as shown in Table 18 in Section 5.11. Test Piece #1, with 100% detection at 0% false call rate compared with the NAVAIR sample's 87% detection at 0% false call rate, yielded slightly better results. This can be attributed to a smaller diameter fastener, which relative to the ferrite core diameter, improves detection [2].

A goal is to determine the minimum flaw size that is detectable using PEC. For comparison, in conventional techniques, where fastener removal is employed, the targeted minimum detectable flaw size for second layer cracks in a multi-layer aluminum lap joint is 0.76 mm (0.030 inches). Using this PEC technique, fastener removal is not required, eliminating the risk of collateral damage to the surface and bore hole caused during fastener removal.

6.5.2 First Layer Notches

The smallest first layer notch (bottom-of-top layer) out of the three multi-layer samples (NAVAIR sample, Test Piece #1 and Aurora sample) was 1.27 mm. If we consider that the minimum reliably detectable flaw size using the conventional eddy current technique 140-306-E [6] for first and second layer cracks is 2.54 mm, then results using the PEC probe in differential mode exceed this detectability. All first layer notches (1.27 mm and larger) were detected, at 95% confidence. Therefore, this PEC technique shows potential to improve the minimum detectable flaw size for first layer cracks to 1.27 mm, without removing fasteners.

6.5.3 Second Layer Notch Detection

The smallest second layer notch out of all three multiple-layer test pieces was 0.82 mm. The Canadian Armed Forces eddy current surface inspection technique [6] for first and second layer defects in CP-140 Aurora lap joint fastener holes can reliably detect first and second layer notches 2.54 mm in length. However, it has limitations in detecting defects in the 0°, 90°, 180° and 270° defect locations, and also requires probe rotation. Test results from the three multi-layer test pieces show that this PEC technique has surpassed the minimum detectable flaw size of 2.54 mm achievable using technique 140-306-E, and that the technique is approaching the BHEC minimum detectable flaw size (defined in Section 1.1) of 0.76 mm, where fastener removal is required. This is comparable to the results obtained here for the NAVAIR and Test Piece #1 samples, where

minimum flaw sizes of 0.89 mm and 0.83 mm, respectively, could be detected with 5% false call rate. Further work is required to establish a minimum detectable flaw size ($a_{90/95}$) for PEC technique.

6.6 False Call Rates

The probability of false calls was defined in Section 2.11, and false call rates were calculated for each set of results on each test piece, depending on confidence level (either 99% or 95%). Considering the 95% confidence interval results for the NAVAIR sample and Test Piece #1 differential data, false call rates were 10% and 0%, respectively. On the Aurora test piece, the differential mode test results yielded a 21% false call rate.

The costs associated with false calls are important for understanding the effectiveness of a technique. Using a 95% confidence interval, a 5% false call rate could be expected; however, two of the test pieces had false call rates above 5%. A larger sample set, including a significant number of blanks, would help improve the statistics of this comparison. If a crack is detected, above the critical crack size, the operator could flag the fastener location, remove the fastener, and perform a BHEC inspection [7], which is capable of reliably detecting 0.76 mm flaws.

6.7 Sources of Uncertainty

6.7.1 Coil Balancing

Coil-based probes are used for conventional eddy current testing and are also being utilized for research in pulsed eddy current techniques. Coil-based probes with two or more coils require careful construction for coil pair matching, to ensure that each coil pair responds in a similar manner. Each individual coil was sensitive to placement in the probe, i.e. the signal amplitude varied with distance from probe face. Achieving exact coil balance for eight coils (four coil pairs) was difficult to achieve. Coil imbalance explains why some coil pairs were more sensitive to the presence of cracks than others.

7 Conclusions and Recommendations

7.1 Conclusions

The motivation for this thesis work was detection of second layer cracks in aluminum lap joints, without ferrous fastener removal, thereby reducing inspection times and potential damage to aircraft. A pulsed eddy current technique was developed, which is capable of detecting cyclic fatigue cracks emanating from around fastener holes in variable directions, with fasteners present. The capability of the technique was shown to approach that of conventional BHEC, and has the added benefit of not requiring fastener removal.

A probe design, consisting of a driving coil wound on a ferrite core with symmetrically located pick-up coils placed over the fastener, is utilized. The probe takes advantage of magnetization by the driving coil of the ferrous fastener, which then acts as a pathway for flux, allowing for deeper penetration of the eddy currents into the surrounding aluminum structure. The probe design has eight pick-up coils, which were used to detect notches emanating in multiple directions from around the fasteners.

A method to distinguish subtle differences between signals from fasteners with and without cracks at their bore was employed due to the similarity between signals from the crack and no-crack case. This statistical technique, called Principal Components Analysis, reduced signals to scores and vectors that describe the maximum amount of variation between them. The relative distance, or Mahalanobis Distance, of a cluster of PCA scores in the presence of a notch to the cluster of PCA scores from blanks was calculated. The distance values were compared to a threshold value, calculated using Hotelling T^2 theory and based on 99% and 95% confidence intervals.

Experiments conducted on three multiple fastener test pieces of similar construction show that notches ranging in size from 0.8-5.5 mm were detectable using the coil-based probe centered over ferrous fasteners. The three samples consisted of 2024-T3 aluminum, but contained different fastener types and sizes. Optimum results were obtained using analysis of differential signals from opposing paired coils, and PCA scores 1-5 at 95% confidence interval. The NAVAIR sample contained HL-19 fasteners with head diameter of 7 mm and first layer thickness of 2 mm. EDM notches, ranging in size from 0.89 mm to 5.46 mm, were present in the first and second layers. Crack detection of 100% was achieved, with 5% false calls. Test piece #1 was lab fabricated,

contained HL-19 fasteners with head diameter of 6.5 mm and had a first layer thickness of 2 mm. Notches ranging in size from 0.82 mm to 3.26 mm were present in the second layer. Test piece #1 yielded 100% crack detection, with 5% false calls. The CP-140 Aurora piece contained HL-51 fasteners with head diameter of 7 mm, and first layer thickness of 2.58 mm. This test piece yielded 82% crack detection with 5% false calls.

Mahalanobis Distance was shown to be correlated with crack size. Smaller cracks tended to produce smaller MD values, whereas larger cracks produced much larger MD values. In addition, first layer cracks produced MD values larger than second layer cracks, for the same crack size. This result identifies a potential means for sizing cracks and identifying in which layer they reside.

Out of all the test pieces, all first layer notches were detected, showing a major improvement over the current method of first layer crack detection with fasteners installed [6], which can only reliably detect flaws of length 2.54 mm and greater. PEC second layer notch detection surpasses the minimum detectable flaw size provided using conventional EC technique 140-306-E [6], and approaches the minimum detectable flaw size for BHEC. Should a flaw be detected, a BHEC inspection [7] could be performed, after fastener removal, to confirm the presence of a crack.

These results provide strong evidence that pulsed eddy current has the capability for second layer crack detection in multi-layer aluminum structures, such as lap joints, approaching the target crack size of 0.76 mm (the minimum detectable flaw size using BHEC [9]). Principal components analysis has been demonstrated as a viable method of reducing signals to fewer dimensions, making subsequent discrimination between scores from fasteners with notches present and fasteners without, easier. PCA also provides a mechanism for compensating for additional variables that may affect PEC signal response (lift-off, fastener head height and variable distance from edge). Introducing Mahalanobis Distance analysis of the PCA scores provided a reliable and consistent way of further discriminating between the two groups of scores, and also shows promise for crack sizing.

7.2 Recommendations

The Mahalanobis Distance analysis is dependent on known samples; in other words, knowing which fasteners do not contain notches at their bore. This is because the covariance matrix is made up of PCA scores from blanks, which is then applied to the other fasteners to calculate their MD values. In order to apply this method to an unknown set of measurements, it would be more expeditious to search for “outliers” or PCA scores that do not belong with the PCA scores from blanks, based only

on their position in the PCA space (not requiring calibration). It is suggested that the fast algorithm for the minimum covariance determinant estimator [41], which generates an initial estimate of the covariance matrix and uses a selective iterative process to determine the minimum covariance matrix, be used. This process would seek to identify outliers in the data (in our case, an outlier would be a PCA score belonging to a fastener with a crack present). This work requires large data sets, and the assumption that the majority of data points are from fasteners that do not contain cracks at their bore, which is normally the case for typical aircraft structure inspections.

The test pieces used for this thesis work all contain notches, which were either electrically discharge machined (EDM) or cut with a band saw blade. In order to determine if this process will reliably detect cyclic fatigue cracking from around ferrous fasteners in the second layer, testing should be conducted on actual fatigue cracks, grown in a lab setting, ideally on test pieces taken from service.

Occasionally, fasteners are replaced during maintenance procedures by different types. These fasteners can be made of different ferrous materials, titanium or even aluminum. It is beneficial to conduct measurements using different fastener materials in order to understand the PEC system response, and subsequently the crack detection ability.

Results from this work showed clusters of PCA scores from one crack orientation separated from clusters from other crack orientations, with respect to blanks. It is recommended that crack propagation directions be analyzed using vector analysis, potentially in spherical coordinates, where the MD value represents the distance from the origin (center of the blank cluster) and angles are measured in polar and azimuthal coordinates [10].

Giant Magnetoresistive Sensors (GMRs) have been used in previous studies, specifically for detecting SCC around ferrous fasteners in the inner wing spar of CF-188 aircraft [26]. GMRs detect the magnetic field directly, and were successful in detecting SCC in the aforementioned work. Yang *et al.* [42] designed a system using a multilayer coil to generate the magnetic field, and GMRs to sense the transient field. Using time and frequency domain features, they successfully detected small cracks under fasteners at depths up to 10 mm. It would be relevant to construct a probe using the same driving coil ferrite core combination, but with GMRs as the sensing element to determine if the same level or improved crack detection is possible.

Surface and internal damage caused by fastener removal/re-installation can cause noise in the acquired signals that may cause false calls to arise. An investigation into the sensitivity of this PEC system to surface and fastener hole damage is suggested to ensure accurate and reliable results.

When an optimized probe design is achieved, whether by using coils or GMRs, a hit/miss or a-hat versus a probability of detection (POD) study should be carried out to determine the $a_{90/95}$, i.e. the crack size above which 90% of the cracks are detected 95% of the time. This study requires a minimum number of flawed and unflawed sites, as well as a proper crack size distribution around the target size to be detected. In addition, the first layer thickness should be varied in order to assess the ability of PEC to detect second layer cracks at a variety of first layer depths.

This technique could potentially be applied to other applications where second layer cracking occurs. This does not have to be specific to wing skin applications, but could possibly extend to any area of the aircraft where either backside access is prohibited, and the first layer is not too thick so as to allow for good penetration and detection of transient eddy current induced fields.

References

- [1] D. E. Bray and R. K. Stanley, *Nondestructive Evaluation, A Tool for Design, Manufacturing and Service*, United States of America: McGraw Hill Inc, 1989.
- [2] P. P. Whalen, "Transient Eddy Current Inspection in the Presence of Ferrous Fasteners in Multi-Layered Aluminum Structures, Master Applied Science Thesis," RMC, Kingston, 2010.
- [3] *Materials Handbook, Non-Destructive Evaluation and Quality Control*, Ninth ed., vol. 17, Metals Park, Ohio: ASM International, 1098.
- [4] A. Sophian, G. Y. Tian, D. Taylor and J. Rudlin, "Design of a pulsed eddy current sensor for detection of defects in aircraft lap joints," *Sensors and Actuators*, vol. 101, pp. 92-98, 2002.
- [5] N. E. Dowling, *Mechanical Behaviour of Materials*, 4th ed., New Jersey: Pearson Education Inc., 2013.
- [6] Canadian Forces Eddy Current Inspection, "Technique # 140-306-E, CP-140 Wing Planks Lap Joint Fastener Holes," 2007.
- [7] Canadian Forces Eddy Current Inspection, "General Bolt Hole Technique for Metallic Structures," 2008.
- [8] Department of Defense, *Nondestructive Evaluation System Reliability Assessment*, MIL HDBK 1823A, Department of Defense, 2009.
- [9] R. Short, *CP140 minimum Inspectable Flaw Sizes for DTA Following Select NDI*, 2012.
- [10] J. D. Griffiths, *Introduction to Electrodynamics*, Upper Saddle River: Prentice-Hall, 1999.
- [11] V. S. Cecco, G. Van Drunen and F. L. Sharp, *Manual on Eddy Current Method*, vol. 1, Chalk River, ON: Chalk River Nuclear Laboratories, 1981.
- [12] R. A. Smith and G. R. Hugo, "Deep corrosion and crack detection in aging aircraft using

- transient eddy current NDE," in *5th Joint NASA/FAA/DoD Aging Aircraft Conference*, 2001.
- [13] T. W. Krause, C. Mandache and J. H. Lefebvre, "Diffusion of Pulsed Eddy Currents in Thin Conducting Plates," vol. 975, 2008, pp. 368-375.
- [14] I. Z. Abidin, C. Mandache, G. Y. Tian and M. Morozov, "Pulsed eddy current testing with variable duty cycle on rivet joints," *NDT&E International*, vol. 42, no. 7, pp. 599-605, 2009.
- [15] T. J. Cadeau, "Increased Field Depth Penetration with Pulsed Eddy Current," RMC, Kingston, 2008.
- [16] P. Horan, P. Underhill and T. W. Krause, "Pulsed eddy current detection of cracks in F/A-18 inner wing spar without wing skin removal using modified principal components analysis," *NDT&E International*, vol. 55, pp. 21-27, 2013.
- [17] J. Lattin, J. D. Carroll and P. E. Green, *Analyzing Multivariate Data*, Pacific Grove: Brooks/Cole, 2003, pp. 4, 264-275.
- [18] Y. He, F. Luo, M. Pan, F. Weng, X. Hu, J. Gao and B. Liu, "Pulsed eddy current technique for defect detection in aircraft riveted structures," *NDT&E International*, vol. 43, pp. 176-181, 2009.
- [19] V. B. Wwdensky, "Concerning the eddy currents generated by a spontaneous change of magnetization," *Annalen de Physik*, vol. 64, pp. 609-620, 1921.
- [20] J. D. Jackson, *Classical Electrodynamics*, California: John Wiley & Sons, INC, 1999.
- [21] C. V. Dodd and W. E. Deeds, "Analytical solutions to eddy current coil probe problems," *Journal of Applied Physics*, vol. 39, no. 6, pp. 2829-2838, 1968.
- [22] D. P. Desjardins, T. W. Krause, A. Tetervak and L. Clapham, "Concerning the derivation of exact solutions to inductive circuit problems for eddy current testing," *NDT&E International*, no. Submitted, 2014.
- [23] D. R. Desjardins, G. Vallieres, P. P. Whalen and T. W. Krause, "Advances in Transient (Pulsed) Eddy Current For Inspection of Multi-Layer Aluminum Structures in the Presence of Ferrous

- Fasteners," *Review of Progress in Quantitative Nondestructive Evaluation*, pp. 400-407, 2012.
- [24] M. N. Sadiku, *Elements of Electromagnetics*, Third ed., New York: Oxford University Press, 2001.
- [25] V. K. Babbar, P. P. Whalen and T. W. Krause, "Pulsed Eddy Current Probe Development to Detect Inner Layer Cracks near Ferrous Fasteners Using COMSOL Modeling Software," in *COMSOL Conference*, Boston, 2012.
- [26] P. F. Horan, Pulsed eddy current inspection of CF-188 inner wing spar, Master's Applied Science Thesis, Kingston: RMC, 2013.
- [27] P. F. Horan, P. R. Underhill and T. W. Krause, "Real Time Pulsed Eddy Current Detection of Cracks in F/A-18 Inner Wing Spar Using Discriminant Separation of Modified Principal Components Analysis Scores," *IEEE Sensors*, vol. 14, no. 1, pp. 171-177, 2014.
- [28] S. Giguere, B. A. Lepine and J. M. Dubois, "Pulsed Eddy Current Technology: Characertizing Material Loss with Gap and Lift-off Variations," *Research in Non-destructive Evaluation*, vol. 13, pp. 119-129, 2001.
- [29] K. I. Kim, K. Jung and H. J. Kim, "Face recognition using kernel principal components analysis," *IEEE Signal Processing Letters*, vol. 9, no. 2, pp. 40-42, 2002.
- [30] J. Yu, "Fault detection using principal components-based gaussian mixture model for semiconductor manufacturing processes," *IEEE Transactions on Semiconductor Manufacturing*, vol. 24, no. 3, pp. 432-444, 2011.
- [31] P. R. Underhill, A. Tetervak and T. W. Krause, "PEC Detection of Cracks in Aluminum Structures in the Presence of Ferrous Fasteners using Modified Principal Component Analysis," in *Smart Materials and CINDE Conference*, Montreal, Nov 2-4 2011.
- [32] V. K. Babbar, P. R. Underhill, C. Stott and T. W. Krause, "Finite Element Modeling of Second Layer Crack Detection in Aircraft Bolt Holes with Ferrous Fasteners Present," *NDT&E International*, vol. 65, pp. 64-71, 2014.

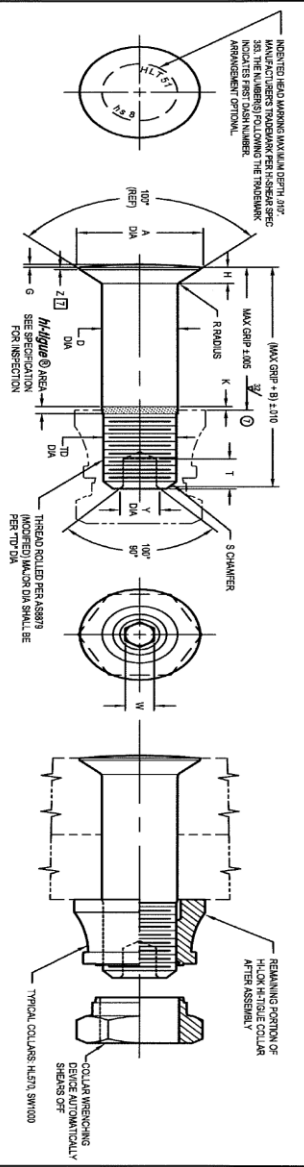
- [33] G. Niu, S. Sinch, S. W. Holland and M. Pechy, "Health monitoring of electronic products based on Mahalanobis Distance and Weibull decision metrics," *Microelectronics Reliability*, vol. 51, pp. 279-284, 2011.
- [34] G. Cosarinsky, M. Ruch, G. Rugirello and G. Domizzi, "Eddy Current Testing Reliability Improvement; Application to Nuclear Fuel Cladding Tubes," in *VIII Congreso Regional de ENDE*, 2011.
- [35] R. De Maesschalck, D. Jouan-Rimbaud and D. L. Massart, "Tutorial: The Mahalanobis Distance," *Chemometrics and Intelligent Laboratory Systems*, pp. 1-18, 2000.
- [36] "NDT Resource Center," 2001. [Online]. Available: <http://www.ndt-ed.org/GeneralResources/Formula/ECFormula/Cond-Resist/CondResist.htm>. [Accessed 25 11 2012].
- [37] H. C. Ohanian, "On the approach to electro- and magneto-static equilibrium," in *American Association of Physics Teachers*, 1983, pp. 1020-1022.
- [38] S. Goldman, Transformation Calculus and Electrical Transients, New York: Prentice Hall Inc., 1949, pp. 90-92.
- [39] A. Sophian, G. Y. Tian, D. Taylor and J. Rudlin, "A feature extraction technique based in principal component analysis for pulsed eddy current NDT," *NDT&E International*, vol. 36, pp. 37-41, 2003.
- [40] "e-Handbook of Statistical Methods," NIST/SEMATECH, [Online]. Available: <http://www.itl.nist.gov/div898/handbook/eda/section3/eda3665.htm>. [Accessed 9 January 2014].
- [41] P. J. Rousseeuw and K. V. Driessen, "A Fast Algorithm for the Minimum Covariance Determinant Estimator," *Technometrics*, vol. 41, no. 3, pp. 212-223, 1999.
- [42] G. Yang, A. Tamburrino and L. Upda, "Pulsed Eddy Current Based Giant Magneto-resistive System for the Inspection of Aircraft Structures," *IEEE*, vol. 46, no. 3, 2010.

Annex B

HL-51 Technical Information



HILSI CORPORATION, U.S.A. — (Parent/Holder) — (Country) — (City) — (State) — (Zip) — (Country) — (City) — (State) — (Zip) — (Country) — (City) — (State) — (Zip)
 HILSI CORPORATION, INC., U.S.A. — (Country) — (City) — (State) — (Zip) — (Country) — (City) — (State) — (Zip) — (Country) — (City) — (State) — (Zip)
 HILSI CORPORATION, INC., U.S.A. — (Country) — (City) — (State) — (Zip) — (Country) — (City) — (State) — (Zip) — (Country) — (City) — (State) — (Zip)
 HILSI CORPORATION, INC., U.S.A. — (Country) — (City) — (State) — (Zip) — (Country) — (City) — (State) — (Zip) — (Country) — (City) — (State) — (Zip)
 HILSI CORPORATION, INC., U.S.A. — (Country) — (City) — (State) — (Zip) — (Country) — (City) — (State) — (Zip) — (Country) — (City) — (State) — (Zip)



FIRST DASH NO.	PN	A	B	D	TD	F	G	H	K	R	Z	S	THREAD	SOCKET		DOUBLE SHEAR POUNDS MINIMUM	TENSION POUNDS MINIMUM
														W	T		
5	532	2672	312	1635	1595	0.04	0.15	0.410	0.13	0.25	0.10	1.02° x 45°	8-32UNF-3A	0.801	1.35	5.280	1,700
6	316	2964	325	1935	1840	0.05	0.15	0.470	0.16	0.30	0.15	1.02° x 45°	10-32UNF-3A	0.895	1.55	7.080	2,500
8	1/4	3848	385	2485	2440	0.06	0.15	0.610	0.21	0.30	0.15	1.02° x 45°	1/4-20UNF-3A	0.967	1.59	12.260	4,400
10	5/16	4739	500	3120	3050	0.07	0.15	0.750	0.28	0.40	0.15	3/84° x 45°	5/16-24UNF-3A	1.285	1.79	19,160	7,000
12	3/8	5554	545	3740	3640	0.08	0.10	0.790	0.30	0.40	0.15	3/84° x 45°	3/8-24UNF-3A	1.577	2.20	27,500	10,000
14	7/16	6920	635	4385	4270	0.09	0.10	0.944	0.35	0.50	0.22	3/84° x 45°	7/16-20UNF-3A	1.850	2.30	37,500	12,500
16	1/2	7540	685	4590	4500	0.10	0.15	1.038	0.39	0.60	0.22	3/84° x 45°	1/2-20UNF-3A	2.292	2.50	49,100	18,000

GENERAL NOTES:
 1. Head edge out of roundness shall not exceed "F".
 2. Concentricity. Circular surface of head to "D" diameter within .005 FIR.
 3. "F" is dimensioned from maximum "D" diameter.
 4. Surface texture per ANSI B46.1.
 5. Dimensions to be met before finish, except threads.
 6. Hole preparation per NAS918.
 7. Curved or full edge manufacturer's option.
 8. Evidence of broken edge across parts.
 9. Use HLT51 for oversize replacement.

MATERIAL: PH13-8Mo stainless steel per AMS5923.
HEAT TREAT: 125,000 psi shear minimum.
FINISH: HLT51(X) = Passivate per H-Shear Spec. 258 and only alcohol lube per H-Shear Spec. 305.
 HLT51(D)(X) = Solid film lube per ASS972 Type I and only alcohol lube per H-Shear Spec. 305.
 HLT51(T)(X) = Solid film lube per ASS972 Type I and only alcohol lube per H-Shear Spec. 292, and only HLT51(V)(X) = Hikka 2 solid film lube per H-Shear Spec. 305.
 HLT51(W)(X) = Hikka 2 solid film lube per H-Shear Spec. 305, on head, and only alcohol lube per H-Shear Spec. 305.
 HLT51(Y)(X) = Solid film lube per ASS972 Type I, while paint on head, and only alcohol lube per H-Shear Spec. 305.

HOW TO ORDER
EXAMPLE: P/N Part Number Only
 HLT51TB88
 816 or 12 Maximum Grip Length
 8102 or 14 Nominal Diameter Pin
 Finish
 Pin Part Number

CODE: First dash number indicates nominal diameter in 1/32nds.
 Second dash number indicates maximum grip in 1/16ths.
 See finish note for explanation of code letters.

DRAWN	DATE	TITLE
OP S.	1-20-77	H-FIGURE PIN
APPROVED	1-20-77	100° FLUSH-CROWN SHEAR HEAD
DESIGN	1-20-77	PH13-8Mo STAINLESS STEEL
REVISION	DATE	SYMBOL NUMBER
1	1-2-73	HLT51

H-FIGURE PIN AND COLLAR AFTER ASSEMBLY registered trademark of H-Shear Corporation.
 © 2013 H-Shear Corporation

Annex C

Temperature Testing Results on Probe

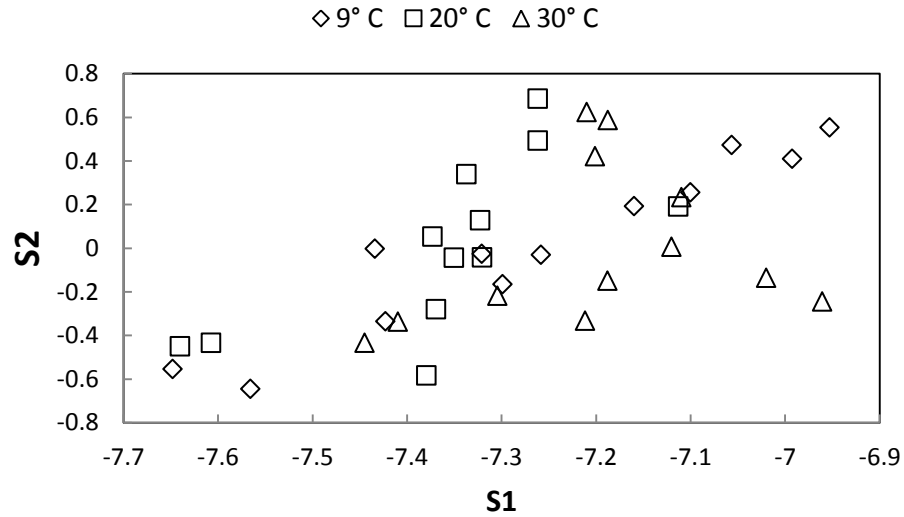


Figure C-1: PCA scores S2 vs S1 for temperature testing results.

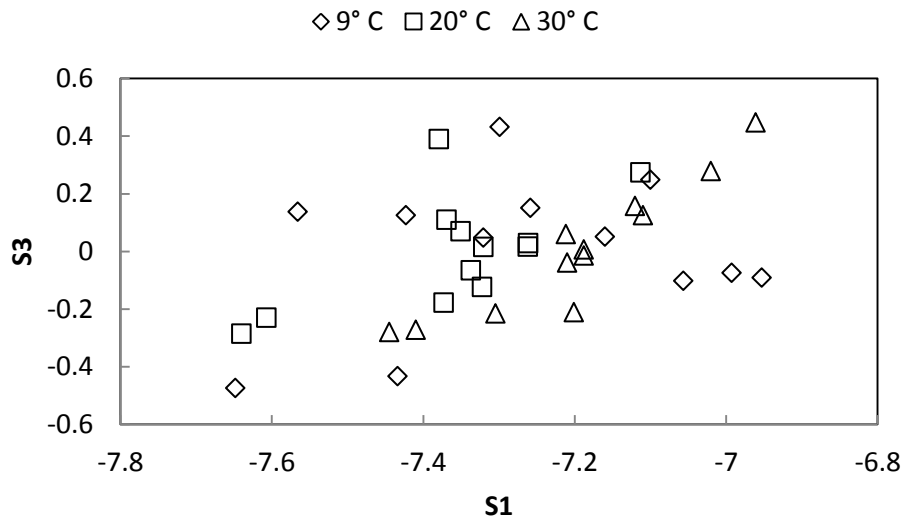


Figure C-2: PCA scores S3 vs S1 for temperature testing results.

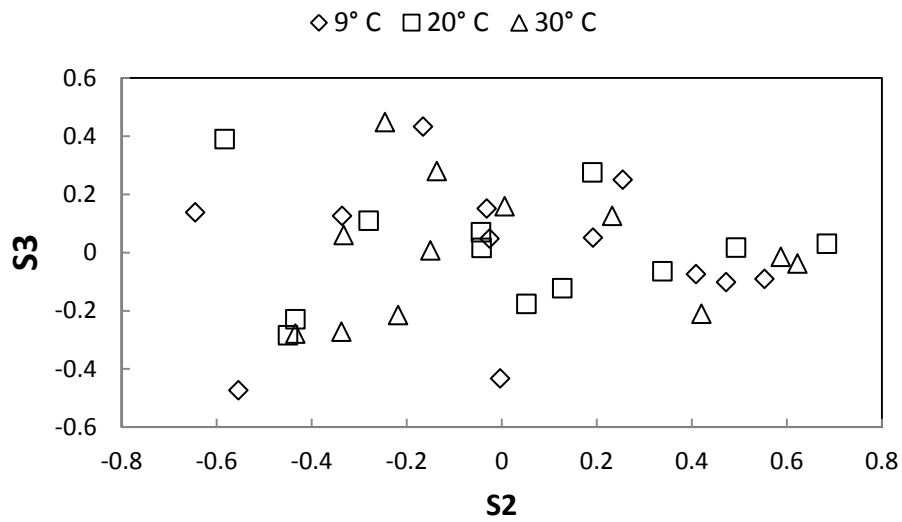


Figure C-3: PCA scores S3 vs S2 for temperature testing results.

Curriculum Vitae

Curriculum Vitae

Captain Colette Stott, né Gardiner, was born in Glace Bay Nova Scotia on 24 September 1985. She obtained a Bachelors of Mechanical Engineering Degree from the Department of Mechanical Engineering at the Royal Military College of Canada in May 2008. Upon graduation, she attended Aerospace Engineering Officer Basic Training in Borden Ontario, and was subsequently posted to 427 Special Operations Aviation Squadron in Petawawa Ontario. She served as the Maintenance Support Officer, and the Deputy Squadron Aircraft Maintenance Engineering Officer, as well as the Aircraft Fluids Safety Officer until 2012.

Upon completing her tour in Petawawa, Colette was posted to Kingston Ontario to complete a Masters of Applied Science in Chemistry and Chemical Engineering at the Royal Military College of Canada.

Papers published in referred, peer reviewed, scholarly journals:

V. K. Babbar, P. R. Underhill, C. Stott and T. W. Krause, "Finite Element Modeling of Second Layer Crack Detection in Aircraft Bolt Holes with Ferrous Fasteners Present," *NDT&E International*, vol. 65, pp. 64-71, 2014.

Submitted Papers:

C.A. Stott, P.R. Underhill, T.W. Krause, 'Pulsed Eddy Current Detection of Cracks in Multilayer Aluminum Lap Joints', IEEE Sensors Journal, submitted June 2014.

Invited Talks and Papers Presented at Major Conferences and Symposia:

C.A. Stott, P.R. Underhill and T.W. Krause, 'Pulsed Eddy Current Detection of Second Layer Cracks in Aluminum Aircraft Lap Joints using Cluster Analysis', Invited Talk to the Department of Physics Colloquium, Royal Military College of Canada, Kingston, ON, 10 April, 2014.

C.A. Stott, P.R. Underhill and T.W. Krause, 'Detection of second layer fatigue cracks around ferrous fasteners in lap joints of a CP-140 Aurora', NDT in Canada Conference, Toronto, ON, 16-18 June, 2014.